Universidad Rey Juan Carlos

Departamento

Teoría de la Señal y Comunicaciones

y

Sistemas Telemáticos y Computación

PhD Dissertation

Robust Signal Processing in Cardiac Signals:

Applications in Heart Rate Variability, Heart Rate Turbulence and Fibrillatory Arrhythmias

Author

Óscar Barquero Pérez

Supervisors

Dr. José Luis Rojo Álvarez

Dra. Inmaculada Mora Jimémez

Fuenlabrada, June 2014

José Luis Rojo Álvarez, con D.N.I. 09788715-F, e Inmaculada Mora Jiménez, con D.N.I. 04591755-N, como Director y Co-directora de la Tesis Doctoral realizada por Óscar Barquero Pérez y titulada *Robust Signal Processing in Cardiac Signals: Applications in Heart Rate Variability, Heart Rate Turbulence and Fibrillatory Arrhytmias*, hacemos constar que ésta cumple con todos los requisitos necesarios y, por ello, autorizamos la defensa de la misma.

Fdo.

Fuenlabrada,   de   de 2014.

TESIS DOCTORAL

Robust Signal Processing in Cardiac Signals: Applications in Heart Rate Variability, Heart Rate Turbulence and Fibrillatory Arrhythmias

Autor: Óscar Barquero Pérez

Directores: Dr. José Luis Rojo Álvarez

Dra. Inmaculada Mora Jiménez

Firma del Tribunal Calificador:

Firma

Presidente:

Vocal:

Vocal:

Vocal:

Secretario:

Calificación:

Fuenlabrada,   de   de 2014.

Resumen

El principal objetivo de esta Tesis Doctoral, en el campo del procesamiento digital de señales biomédicas, es el desarrollo de métodos robustos de análisis cardiaco. La Tesis tiene dos objetivos específicos, a saber, (1) caracterizar la fibrilación auricular y ventricular (FA, FV), y (2) evaluar, de forma no invasiva, el control del ritmo cardiaco por parte del Sistema Nervioso Autónomo (SNA) y el barorreflejo.

El análisis espectral de electrogramas (EGM) se ha utilizado para caracterizar el ciclo medio (periodicidad) y la regularidad de la FV. Sin embargo, mediante este enfoque se descarta información relevante del espectro, como puede ser, la estructura armónica o la envolvente espectral. En el Capítulo 1 2 se presenta un método paramétrico basado en una extensión del desarrollo en serie de Fourier, que incorpora componentes para caracterizar fluctuaciones de banda estrecha. Este enfoque, llamado *Fourier Organización Análisis* (FOA), se utiliza para caracterizar la periodicidad e irregularidad, así como para proporcionar información detallada sobre el contenido espectral tanto de EGMs simulados como reales. Se estudiaron EGMs, registrados egistrados en desfibriladores automáticos implantables, en distintas condiciones, a saber, ritmo sinusal, taquicardia supraventricular, taquicardia ventricular y FV. Los parámetros obtenidos utilizando FOA mejoraron las mediciones de organización y regularidad obtenidas mediante los métodos clásicos. De esta forma, se puede concluir que FOA proporciona una descripción espectral detallada y más robusta.

El análisis avanzado de la FA en EGM intracardiacos tiene como objetivo determinar las zonas más apropiadas para la ablación. Los métodos basados en el dominio de la frecuencia estiman la frecuencia dominante con el objetivo de identificar regiones cardiacas de rápida activación como objetivos de ablación. Sin embargo, a menudo, descartan información relevante del espectro y proporcionan una caracterización incompleta de las señales de FA complejas. En el Capítulo 3 se propone un método para estimar la frecuencia fundamental de la FA basado en una generalización , utilizando kernels, de la función de correlación para procesos estocásticos, llamado *Correntropy*. Este enfoque proporciona una estimación robusta de la periodicidad de señales complejas de FA y, combinado con FOA, proporciona una caracterización completa de la regularidad y del contenido espectral de la FA. Se utilizaron EGM intracardiacos en FA durante estudios electrofisilógicos con diferentes grado de complejidad, seleccionados visualmente por un experto. La estimación de la frecuencia fundamental utilizando Correntropy, combinado con un

enfoque de componentes múltiples mediante FOA, permitió establecer una caracterización completa de señales de FA complejas.

El análisis espectral de las series temporales latido-a-latido para evaluar la Variabilidad de la Frecuencia Cardiaca (VFC) ha sido ampliamente utilizada en la literatura. Sin embargo, esta aproximación es muy sensible a la presencia de ruido, artefactos y falsas detecciones de latidos, que son un problema común en los registros Holter. En el Capítulo 4, se propone un método robusto para interpolar series temporales muestreadas de forma no uniforme, como es el caso de la señal de VFC, basado en *Support Vector Machine* (SVM). Se propone utilizar un núcleo de Mercer espectralmente adaptado, basado en la autocorrelación de la serie temporal latido-a-latido. Este enfoque permite realizar un análisis espectral robusto de la señal de VFC, y podría evitar la costosa tarea de corrección manual, habitual en los registros Holter, necesaria para obtener índices espectrales fiables.

La Turbulencia de la Frecuencia Cardiaca (TFC), que es la respuesta provocada por un Complejo Ventricular Prematuro (CVP), ha demostrado ser un fuerte criterio útil de estratificación de riesgo en pacientes con enfermedad cardiaca. A fin de reducir el nivel de ruido de TFC, las mediciones convencionales de TFC utilizan el promedio todos los CVP en un paciente. Sin embargo, este enfoque proporciona índices de largo plazo, con información promediada de todo el registro, y no tiene en cuenta las condiciones fisiológicas locales. En el Capítulo 4 5 se propone un método para eliminar el ruido de los CVPs individuales usando una técnica de procesamiento de señales basado en SVM. Se utilizaron CVPs estimulados durante estudio electrofisiológico como estándar de bajo ruido. El enfoque propuesto proporciona mediciones de TFC, en base de datos de Holter, con una reducción significativa en sesgo y varianza. Por lo tanto, la eliminación de ruido en TFC mediante SVM permite obtener mediciones a corto plazo, a la par que mejora el nivel de ruido de las medidas a largo plazo.

La TFC está afectada por varios factores fisiológicos, principalmente por la frecuencia cardiaca (FC) y el intervalo de acoplamiento (IA) del CVP. La hipótesis fisiológica para explicar la TFC es la respuesta barorrefleja después de un CVP. Sin embargo, varios estudios han proporcionado resultados contradictorios sobre la relación entre el IA y los índices de TFC. En algunos casos, los resultados fueron incluso contrarios a la hipótesis del origen barorreflejo de la TFC. En el Capítulo 6 se propone un modelo de regresión no lineal para evaluar la influencia del IA y de la FC sobre la TFC tanto en datos de estudio electrofisiológico y de registros Holter. Los resultados mostraron que el modelo de regresión no lineal es capaz de explicar la influencia del IA sobre la TFC ,en pacientes sanos, de una forma acorde con la hipótesis barorrefleja.

Abstract

The main objective of this doctoral Thesis, in the field of biomedical signal processing, is to develop robust methods for cardiac signal analysis. It has two specific objectives, namely, (1) to characterize atrial and ventricular fibrillation (AF, VF), and (2) to assess, noninvasively, the baroreflex and the Autonomic Nervous Systems (ANS) control of the heart rate.

Spectral analysis of electrograms (EGM) has been used to characterize the average cycle (periodicity) and regularity of VF. However, relevant information of the spectrum has been often discarded in this approach, such as the harmonic structure or the spectral envelope. In Chapter 2, a parametric method based on an extension of Fourier Series that accounts for narrow band fluctuations is presented. This approach, called Fourier Organization Analysis (FOA), is used to characterize the periodicity and irregularity, as well as to provide detailed information about the spectral content of EGM simulated in a computer model, and actual EGM recorded in Implantable Cardioverter Defibrillator (ICD). Different conditions are studied, namely, sinus rhythm, supraventricular tachycardia, ventricular tachycardia and ventricular fibrillation. Parameters obtained using FOA improved the organization measurements with respect to the classic approaches. Therefore, FOA yields a more detailed and robust spectral description of EGM.

Advanced analysis of AF intracardiac EGMs aims to establish clinical targets for ablation. Frequency domain methods estimate the dominant frequency to identify cardiac sites with high activation rates as ablation targets. However, they often discard relevant information in the spectrum, and they might provide an incomplete characterization of complex AF signals. In Chapter 3, a method to estimate the AF fundamental frequency based on a kernel generalization of the correlation function for stochastic processes, called Correntropy, is proposed. This approach provides a robust estimation of AF periodicity, which could be a difficult problem in complex AF signals. Complete characterization of the regularity and spectral content is provided using FOA. AF intracardiac EGMs recorded during Electrophysiological Studies (EPS) with different degree of complexity, visually selected by an expert, are studied. Correntropy estimation of fundamental frequency, combined with FOA, allowed to estimate the periodicity as well as to characterize complex AF signals by using a multicomponent approach to FOA.

Spectral analysis of beat-to-beat time series to assess Heart Rate Variability (HRV) has been widely used in the literature. However, this approach is very sensitive to the presence of noise, artifacts and false beat detections,

which are a common problem in Holter recordings. In Chapter 4, a robust method is proposed to interpolate time series nonuniformly sampled, as in HRV, based on Support Vector Machine (SVM) regression. A spectrally adapted Mercer kernel, based in the autocorrelation of the beat-to-beat time series, is proposed. This approach allows to perform a robust spectral analysis of HRV signals, and it might avoid the time-consuming task of manually correction of beat-to-beat time series from Holter recordings, which is needed to obtain reliable spectral measurements.

Heart rate turbulence (HRT) response after a Ventricular Premature Complex (VPC) has been shown to be a strong risk stratification criterion in patients with cardiac disease. In order to reduce the noise level of the HRT signal, conventional measurements use a patient-averaged of VPCs. However, this approach provides only long-term HRT indexes and it does not take into account local physiological conditions. In Chapter 5, a method to denoise individual VPCs is proposed using a signal processing technique based on SVM regression. HRT stimulated during EPS is used as a low-noise gold standard. This approach provided HRT measurements, in a 24-h Holter patient database, with significant reduction in the bias and the variance. SVM denoising yields short-term HRT measurements and improves the signal-to-noise level of long-term HRT measurements.

HRT is known to be affected by several physiological factors, mainly heart rate (HR) and coupling interval (CI) of VPC. The physiological hypothesis to explain the HRT is a baroreflex response after the VPC. However, several studies showed different results about the relationship between CI and HRT parameters. In some cases results were contrary to the hypothesis of baroreflex source of HRT. In Chapter 6, a nonlinear regression model is proposed to assess the influence of CI and HR on HRT using data from EPS and from Holter recordings. Results showed that the nonlinear regression model is able to explain the influence of CI on HRT for healthy patients in accordance with the baroreflex hypothesis.

Acknowledgements

La primera acepción de la palabra *tesis* habla de *conclusión*, apropiada definición para este documento. Antónimo de *conclusión* es el inevitable *inicio*.

Ambas situaciones, *conclusión* e *inicio*, las he de agradecer, sin menor duda, a mis directores de tesis. Gracias.

Gracias a Arcadi: eres un amigo.

Gracias a Leif: eres un amigo.

La última acepción de *tesis* habla del impulso necesario para marcar el ritmo. Sin duda, todos mis compañeros del departamento han funcionado como mi *tesis*, los que fueron y los que son. Noy soy rácano, no es momento, son mis AMIGOS.

Desafortunadamente la RAE no ofrece acepción de *tesis* que me sirva para la familia (cuñadas, primos, titos, titas, sobrinos, ...) y amigos. Está claro, no hay palabras para ellos. Son muchos, pero que no les quepa duda, sabrán, en su momento, que son ellos.

Mi pueblo, Siruela: es mi familia, soy yo.

Mis padres y mis hermanos, mis hermanos y mis padres.

Mi familia de Zarautz.

A José Saramago, que não deixou que eu ficasse sossegado: sou muito menos ignorante hoje do que nunca fui. "Encontramo-nos noutro sítio".

Familia = RebecAdriánInge +?

The Author

ix

List of Acronyms and Abbreviations

AF Atrial Fibrillation

AMI Acute Myocardial Infarction

ANS Autonomic Nervous System

AV Atrioventricular

CESNI Continuous-time Equivalent System for Nonuniform Interpolation

CI Coupling Interval

CL Cycle Length

CSD Correntropy Spectral Density

ECG Electrocardiogram

EGM Electrogram

EPS Electrophysiological Study

FFT Fast Fourier Transform

HF High Frequency

HRT Heart Rate Turbulence

HRV Heart Rate Variability

ICD Implantable Cardioverter Defibrillator

LF Low Frequency

LMMSE Linear Minimum Mean Square Error

LS Least Squares

LVEF Left Ventricular Ejection Fraction

MFR Mean Firing Rates

ML Maximum Likelihood

MSSF Modulated Squared *Sinc* Function

PSD Power Spectral Density

RSS Residual Sum of Squares

SA Sinoatrial

SCL Sinus Cycle Length

SNR Signal to Noise Ratio

SO Specific Objective

SR Sinus Rhythm

SVM Support Vector Machine

SVT SupraVentricular Tachycardia

TO Turbulence Onset

TS Turbulence Slope

ULF Ultra Low Frequency

VF Ventricular Fibrillation

VT Ventricular Tachycardia

VLF Very Low Frequency

VPC Ventricular Premature Complex

WSS Wide Sense Stationary

Contents

Introduction

This doctoral Thesis is in the field of biomedical signal processing. Physiological signals, specifically cardiac electrical ones, are in general the result of a complex process and they are contaminated with different sources of noise and other physiological processes. This poses a real challenge for the biomedical engineer who is faced with the trade-off of developing methods to characterize biomedical signals and, at the same time, methods easy to interpret. Generally, signal processing methods are either very simple, leading to incomplete characterization but easy interpretation, or are very complex and lead to correct solutions but difficult interpretation, so their actual clinical applicability is doubtful. The aim of this doctoral Thesis is to develop robust signal processing methods in cardiac analysis with the constrain to be methods that provides interpretable and meaningful results. The Thesis has two specific objectives (SO), namely: (1) to characterize atrial and ventricular fibrillation (AF, VF); and (2) to assess, noninvasively, the Baroreflex and the Autonomic Nervous System (ANS) control of the Heart Rate (HR).

Part I of this Thesis deals with the SO-1. In Chapter 2, a novel parametric method to characterize the spectral components of VF Electrograms (EGM) is proposed. Two complementary approaches have been mainly followed in spectral analysis to characterize VF signals, namely Dominant Frequency Analysis (DFA) and Organization Analysis (OA). The former aims to characterize the EGM periodicity, whereas the latter quantifies the signal irregularity that remains unexplained by that periodicity [1]. However, these descriptions have often discarded relevant information of the spectrum, such as the harmonic structure or the spectral envelope. Moreover, it is not always guaranteed that a dominant frequency will give a good estimation for the average cycle (periodicity). In this chapter, a unified, simple, and automatic processing algorithm to provide a more detailed information about the spectral EGM structure is proposed. The method, called Fourier Organization Analysis (FOA), uses a Least Squares (LS) approximation of the EGM, based on a modified harmonic Fourier Series model, closely related to the OA description, accounting for narrow band fluctuations of each component in the EGM Fourier Series. The work developed in this chapter has been published in:

- Óscar Barquero-Pérez, José Luis Rojo-Álvarez, Antonio J. Caamaño, Rebeca Goya-Esteban, Estrella Everss, Felipe Alonso-Atienza, Juan José Sánchez-Muñoz and Arcadi García-Alberola *Fundamental Fre-*

quency and Regularity of Cardiac Electrograms with Fourier Organization Analysis. Vol 57, Num 9, Pag 2168-2177. IEEE Transactions on Biomedical Engineering. Sep 2010.

In Chapter 3, an extension of the method proposed in Chapter 2, to deal with AF signals is proposed. It aims to take into account multiple components and a robust estimation of the fundamental frequency. AF signals have been often characterized with the same methods (DFA and OA) proposed for the analysis of VF [2, 3]. However, some AF signals show a complex structure which could not be completely characterized using the classical approach. Hence, a new method is proposed to estimate the periodicity of the AF signal using a kernel generalization of the correlation function for stochastic processes, called Correntropy. Also, an extension of the FOA method to account for multiple components contributing to the signal at independent fundamental frequencies is proposed. The work of this chapter has been published in the international conference:

- Óscar Barquero-Pérez, Leif Sörnmo, Rebeca Goya-Esteban, Inmaculada Mora-Jiménez, Arcadi García-Alberola, José Luis Rojo-Álvarez. *Fundamental Frequency Estimation in Atrial Fibrillation Signals using Correntropy and Fourier Organization Analysis.* 3rd International Workshop on Cognitive Information Processing (CIP), Pag 1-6, Baiona (Spain) 28-30 May 2012.

Part II of this Thesis deals with the SO-2. In Chapter 4, a novel method is developed to interpolate the nonuniformly sampled beat-to-beat (RR-interval) time series, based on support vector machine (SVM) regression. RR-interval time series are used to study the Heart Rate Variability (HRV), which, in turn, allow to noninvasively assess the control of the HR and its relationship with cardiovascular mortality. HRV analysis is usually performed on 24-h ambulatory ECG recordings (Holter). Spectral analysis of HRV allows to identify the different oscillatory components involved in the HR control, and it is usually identified with the activity of the ANS branches (sympathetic and vagal) [4]. However, Holter recordings suffer from high noise, which induces the presence of artifacts and beat misclassifications. Conventional spectral analysis is very sensitive to these problems in Holter recordings. In this chapter, a novel robust method is proposed for nonuniform interpolation based on SVM regression with the autocorrelation of the observed sequence as a high performance kernel. The work developed in this chapter has been published as a part of:

- Carlos Figuera, Óscar Barquero-Pérez, José Luis Rojo-Álvarez, Manel Martínez-Ramón, Alicia Guerrero-Curieses, Antonio J. Caamaño. *Spectrally Adapted Mercer Kernels for Support Vector Nonuniform Interpolation*, Signal Processing, Vol 94, Pag 412-433, Jan 2014.

In Chapter 5, a method is proposed for denoising RR-interval segments of 15-20 samples after ventricular premature contractions (VPC), so called

VPC-tachograms, to study the Heart Rate Turbulence (HRT). In healthy subjects, HRT shows an early acceleration and a late deceleration of the HR. In patients with cardiac conditions, HRT is attenuated or even completely suppressed. Therefore, HRT has been used to assess the baroreflex and ANS control of the HR after a VPC (non-sinusal beat). The usual procedure to assess HRT involves to average all the available VPC-tachograms in a Holter recording, aiming to filter the noise present on individual VPC-tachograms [5, 6]. However, this procedure needs a large number of VPC-tachograms, and has the implicit assumptions of statistical independence on the noise, which could be questioned from an electrophysiological point of view. In this chapter, a robust denoising method based on SVM regression is proposed. This approach allows to provide reliable assessment of HRT even with few VPC-tachograms. Also, a new index to assess the HRT on single denoised VPC-tachograms, called Turbulence Length, is proposed. The work developed in this chapter has contributed to following publications:

- José Luis Rojo-Álvarez, Óscar Barquero-Pérez, Inmaculada Mora-Jiménez, Estrella Everss, Ana Belén Rodríguez-González and Arcadi García-Alberola. *Heart Rate Turbulence Denoising Using Support Vector Machines.* Vol 56, Num 2, Pag 310-319, IEEE Transactions on Biomedical Engineering, Feb 2009.

- Sergio Manzano-Fernández, Francisco J. Pastor-Pérez, Óscar Barquero-Pérez, Domingo A. Pascual-Figal, Rebeca Goya-Esteban, José Luis Rojo-Álvarez, Antonio Caamaño-Fernández, María Dolores Martínez Martínez-Espejo, James Louis Januzzi, Mariano Valdés, Arcadio García-Alberola. *Short-Term Variability of Heart Rate Turbulence in Chronic Heart Failure.* Vol 17, Num 9, Pag 735-741, Journal of cardiac failure, Sep 2011.

In Chapter 6, the influence of several physiological variables on the HRT is explained by means of a nonlinear regression model. The physiological fundamentals of the HRT are based on a baroreflex source and, accordingly, several physiological factors affect the HRT response. Namely, the HR and the VPC prematurity are important factors affecting the HRT. The HR influence on HRT has been explained and demonstrated in the literature, so that, high HR yields an attenuation on the HRT response. However, the study of the VPC prematurity influence on HRT has led to conflicting results in the literature [6, 7]. In this chapter, a nonlinear ridge regression model is proposed that is able to account for nonlinear relationships and interaction terms. Results provided by the model in data from healthy subjects, as well as in cardiac condition patients with good prognostic, agreed with the baroreflex source of HRT hypothesis. The contributions of this chapter are published in:

- Óscar Barquero-Pérez, Carlos Figuera, Rebeca Goya-Esteban, Inmaculada Mora-Jiménez, José Luis Rojo-Álvarez, Javier Gimeno-Blanes,

Arcadi García-Alberola, *Heart Rate Turbulence Modulation with Coupling Interval and Heart Rate*, 39th Computing in Cardiology, Krakow, Poland, Sep 9-12, 2012.

- Óscar Barquero-Pérez, Rebeca Goya-Esteban, Carlos Figuera, Inmaculada Mora-Jiménez, Arcadi García-Alberola, José Luis Rojo-Álvarez. *Physiological Feature Analysis in Heart Rate Turbulence using LASSO Model*, 40th Computing in Cardiology, Zaragoza, Spain, Sep 22-25, 2013.

Part I

Overview of the Research Field

Chapter 1

Background

In this chapter an overview of the research field is presented. First, a brief introduction to the cardiovascular system, and in particular to the heart, is outlined. Second, the electrical activity of the heart to generate a coordinated contraction (a beat) is outlined, as well as a brief introduction to the ECG. Following, a description of the physiological background is presented to understand the different problems tackled in this Thesis is presented, namely VF, AF, HRV, and HRT.

1.1   Anatomy of the Heart

The cardiovascular system has as main function to facilitate the exchange of oxygen, carbon, dioxide and nutrients between the cells and the outside environment. The cardiovascular system ensures that adequate blood flow is delivered to organs, so that this exchange can take place. The cardiovascular system consists on two separate circulatory subsystems: the systemic and the pulmonary. The heart connects both subsystems acting as a double pump, one for each circulatory subsystem. The systemic circulation transports the blood with oxygen and nutrients to the various muscles and organs, where oxygen is partially exchanged with carbon dioxide, resulting in a blood partially deoxygenated. The blood returns to the heart by the veins, and is redirected to the pulmonary circulation, in which the partially deoxygenated blood is carried to the lung tissues, where the carbon dioxide is exchanged for oxygen in the alveoli. Finally, this oxygened blood returns back to the heart and into the systemic circulation again, performing a complete cycle on the cardiovascular system [8, 9].

The heart can be defined as a muscle organ whose main function is to propel the blood into the cardiovascular system. The anatomy of the heart is divided into two sides, *right heart* and *left heart*. Each side consists of two chambers, the *atrium* where the blood enters from the veins, and the *ventricle* where the blood is propelled into the arteries. The *right heart* receives the blood from the systemic circulatory system and pumps it into the pulmonary circulatory systems, whereas the *left heart* receives the blood from the pulmonary system and pumps it into the systemic system [10, 11].
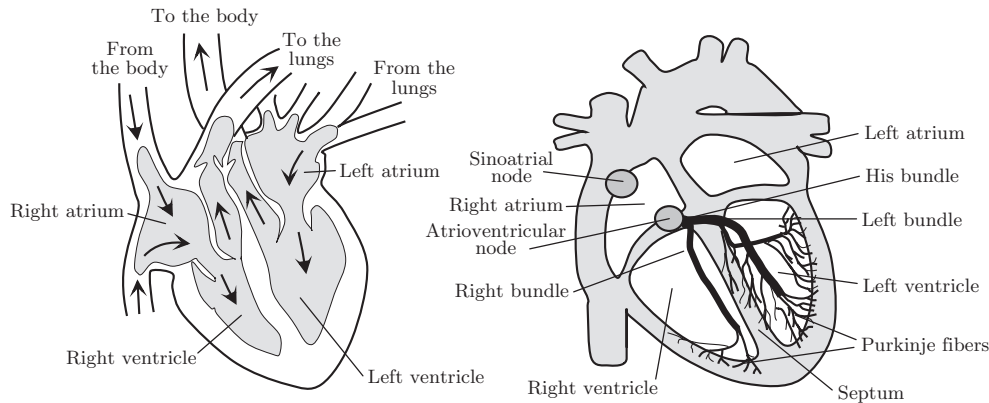
Figure 1.1: *Anatomy of the heart and electrical conduction system. Taken from [11].*

Figure 1.1 (left) represents a picture of the anatomy of the heart.

1.2   Electrical Activity of the Heart Electrocardiogram

The function of the heart as a blood pump is achieved by cardiac contraction, which is triggered by the propagation of an electric impulse through the heart muscle (*myocardium*). Cardiac contraction is effective only if it is synchronized, which is achieved by the electrical conduction system that allows electrical impulses to spread rapidly, and in an organized way, throughout the heart [11, 12], see Figure 1.1 (right).

Each cardiac cycle is triggered by an electrical impulse originated in the sinoatrial (SA) node, which is a collection of cells with the ability to automatically generate an electrical impulse, which spreads across the atria, causing them to depolarize, and eventually, to contract impelling the blood to the ventricles. The electrical impulse has only available one pathway to enter the ventricles, which is the atrioventricular (AV) node. Here, a delay is introduced a delay in the conduction for two reasons. First, it allows a complete atrial depolarization-contraction, and therefore a complete passage of blood from the atria to the ventricles. Second, it limits the frequency of impulses travelling through AV node to the ventricle to prevent high ventricular rates in some atrial arrhythmias. The electrical impulse leaving the AV node enters the ventricle at the bundle of His, and then follows the left and right bundle branches. Then, the impulse is conducted by the Purkinje fibers at high velocity throughout the ventricles. These fibers conduct the electrical impulse to the muscular walls of the ventricles, which contract and force the blood out of the heart. This represents a complete electrical cycle of a heartbeat.

The whole conduction system of the heart is very important because it permits rapid, organized, and synchronized depolarization and contraction
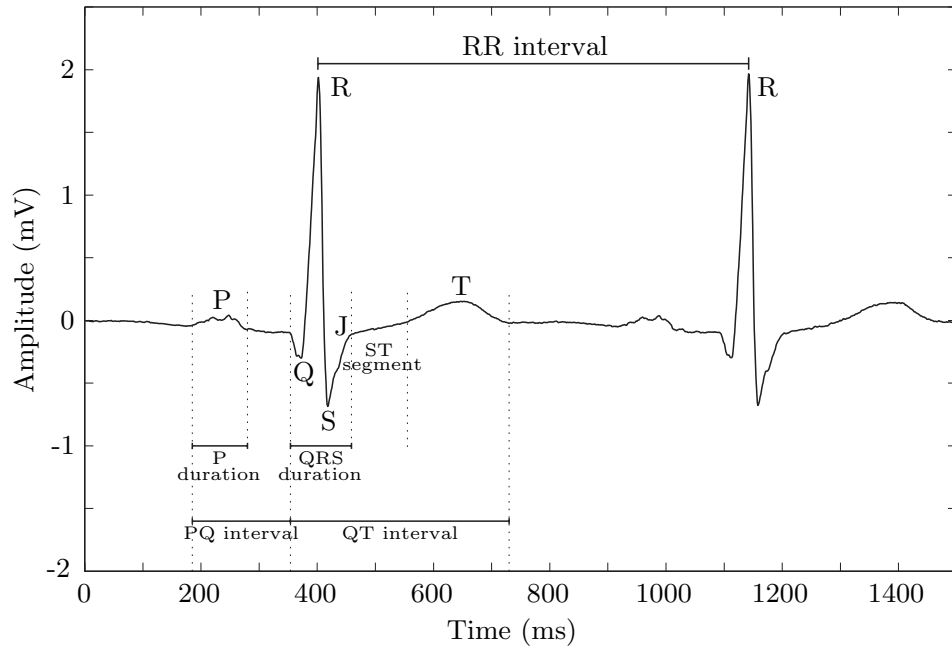
Figure 1.2: *Waves and intervals in a heart beat recorded in an ECG. Taken from [11].*

of the ventricles, which eventually allows for an efficient ventricular contraction [8].

The ECG is recorded by a number of electrodes attached to the body surface. The standard 12-lead ECG is acquired using ten electrodes, three are located on the wrists and ankle joints, and the remaining six are located on the chest. When recording the ECG continuously over long periods of time, only three electrodes are often used. During normal Sinus Rhythm (SR), each heartbeat in the ECG signal consists of a P wave, a QRS complex and a T wave. The P wave corresponds to atrial activation, the QRS complex to activation of the ventricles, and the T wave to ventricular recovery [11, 12]. Figure 1.2 shows the different waves and intervals in a heart beat.

1.3 Fibrillatory Arrhytmias

Cardiac fibrillation is the rapid acceleration and spatial desynchronization of mechanical contractions of the heart, and it is the leading cause of death in the industrialized world [13, 14]. Cardiac fibrillation can occur both in the atria and in the ventricles, called AF and VF, respectively. ECG recordings of fibrillation are characterized by rapid, irregular electrical activity. Figure 1.3 shows examples of AF and VF. VF is a lethal arrhythmia and leads to death if not stopped within minutes. Although AF is not immediately lethal, it is the most common sustained cardiac arrhythmia in clinical practice [13, 15].

Spectral analysis of cardiac fibrillation signals has increased in the recent

(a) AF ECG recording
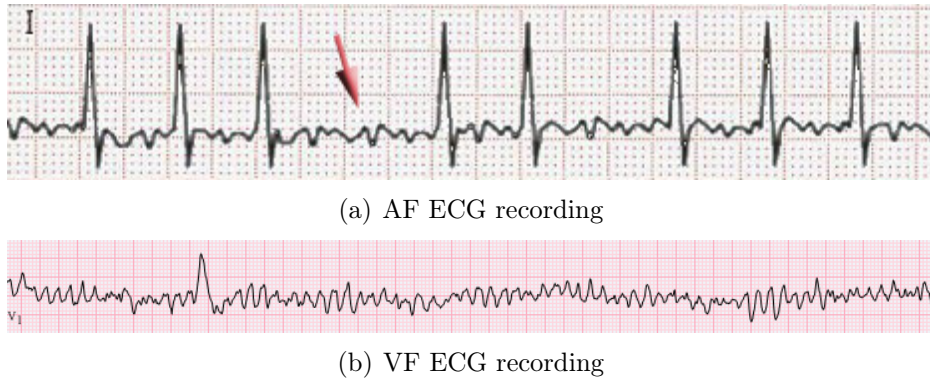
(b) VF ECG recording

Figure 1.3: *AF and VF ECG recordings. ECG recording in AF presents the complex QRS since the electrical impulse reaches the AV node, and then propagates normally in the ventricles. Arrow highlights the absence of P wave.*

years [16, 17]. Basically, spectral analysis aims to characterize the regularity, the averaged cycle of the signal, and the organization, in the sense of how different is the signal from pure sinusoidal behaviour.

In the remaining of the section, AF and VF are explained in more detail, as well as the usual signal processing techniques.

1.3.1   Atrial Fibrillation

AF is the most common sustained cardiac arrhythmia, occurring in 1 – 2% of the general population. Over 6 million Europeans suffer from this arrhythmia, and its prevalence is estimated to at least double in the next 50 years as the population ages [15].

In AF, the origin of the electrical impulses can be at different areas in the atria, instead of the sinusal node. Several impulses originated at different locations in the atria spread throughout the atria causing uncoordinated rapid atrial contractions. As a consequence of the rapid atrial rate during AF, the ventricular response is rapid and irregular. According to [15], one in five of all strokes is attributed to this arrhythmia. Ischaemic strokes in association with AF are often fatal, and those patients who survive are left more disabled and more likely to suffer a recurrence than patients with other causes of stroke.

The electrophysiological mechanisms of AF are not yet completely understood. Three main mechanisms have been proposed to explain the initiation and perpetuation of AF:

Focal mechanisms. Haïsaguerre *et al.* [18] reported that AF is often triggered by a focal activity. Pulmonary veins, because of shorter refractory periods and abrupt changes in myocite fiber orientation, have a strong potential to perpetuate AF.

Multiple wavelet hypothesis. Moe *et al.* [19] proposed that AF is per-

Figure 1.4: *Bipolar EGMs from a patient in AF during an EPS.*

petuated by continuous conduction of several independent wavelets propagating through the atria in a chaotic way. Fibrillation wavefronts continuously undergo wavefront–waveback interactions, resulting in wavebreak and the generation of new wavefronts, which in some conditions allow to sustain the AF.

Wandering rotors. Jalife *et al.* [20] proposed that AF can be the result of the interaction between self-sustaining rotors, this is vortices of electrical spiral waves. Such rotors are self-sustained and may be stationary, or they may drift but subsequently anchor to anatomical heterogeneities in cardiac muscle.

In AF, the atria depolarize in an uncoordinated fashion, which is reflected in the ECG by the replacement of the P wave by an undulating baseline, where the waves are called *f-waves*, see Fig. 1.3(a). Several techniques have been proposed to remove ventricle activity to analyze the AF in ECG recordings [21].

Intracardiac recordings, EGMs , of AF are usually obtained during Electrophysiological Studies (EPS). The usual procedure is to insert several catheters, with several recording electrodes, into the heart through the veins. Atrial activity is recording by electrodes from the catheter, usually the electrical potential measured between two adjacent electrodes, 2-5 mm distance, is recorded in *bipolar* EGMs. Figure 1.4 shows three bipolar EGM intracardiac signals in AF from a patient in an EPS.

There has been a recent increase interest on the analysis of AF in the frequency domain and in its application to the clinical environment. Indeed, several clinical targets for AF ablation use the EGM spectral representation. These targets aim to give a regular description in the frequency domain in terms of low Cycle Length (CL) and/or high regularity regions. Therefore, the identification of sites with high dominant frequency, f_d, have been proposed as ablation targets [2, 22]. Bipolar and monopolar EGMs can have very sharp waveforms corresponding with rapid depolarization, and this morphology can cause problems identifying f_d in spectral analysis. A set of preprocessing steps has been proposed to condition the signal [3, 23]:

- Bandpass filtering at 40-250 Hz.

(a) Original AF EGM   (b) Preprocessed AF EGM
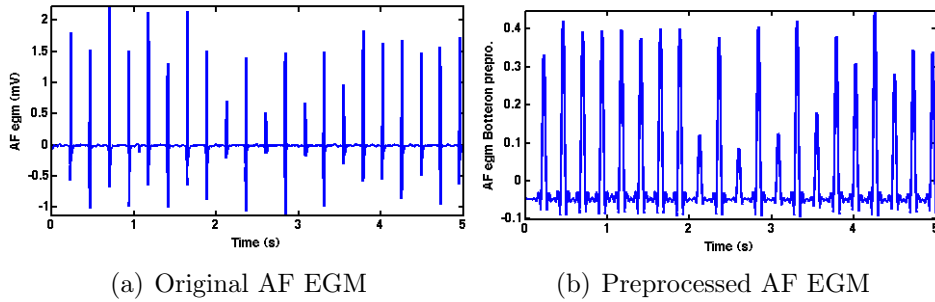
Figure 1.5: *Comparison between the original (a) and the preprocessed (b) bipolar EGM during AF.*

- Rectification.

- Lowpass filtering at 20 Hz.

Figure 1.5 shows a bipolar EGM during AF (a) and the corresponding preprocessed signal (b).

Additionally, regularity analysis is used aiming to measure the relative contribution of the almost-periodic component of an EGM in terms of its signal power. Conventional organization parameters are defined in the frequency domain. The power of the components in a predetermined narrow band (around either the f_d peak or the harmonic peaks) is often used to account for the relevance of the almost-periodic component. Two parameters are typically used. First, The Regularity Index, ri, which was originally defined as the ratio of power in the f_d bandwidth, and the total power in the band [2–30] Hz [2, 24]. And second, the Organization Index, oi, which is another measure defined as the ratio of the power in the f_d bandwidth, combining up to four harmonic peaks, and the total power in the band [2–30] Hz [25, 26].

1.3.2   Ventricular Fibrillation

VF is one of the major arrhythmias associated with Sudden Cardiac Death (SCD). In the United States alone, approximately $300,000$ patients die suddenly each year because of VF. In Europe, the overall rates are similar to those in United States, with significant geographic variations reported [27].

Ventricular fibrillation (VF) is one of the major arrhythmias associated with cardiac arrest. During VF the ventricles do not beat in a coordinated way, leading to inefficient beats and no cardiac output [12]. Consequently, the arterial pressure suddenly drops to exceedingly low levels, and death usually ensues within less than ten minutes as a result of lack of oxygen delivery to vital organs [28].

The mechanisms underlying VF are not yet completely understood. There exists two different theories to explain the initiation and maintenance of VF: the multiple wavelet theory proposed by Moe for the AF, which
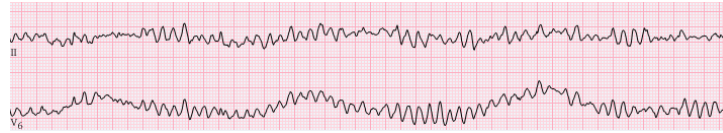
(a) ECG VF recording
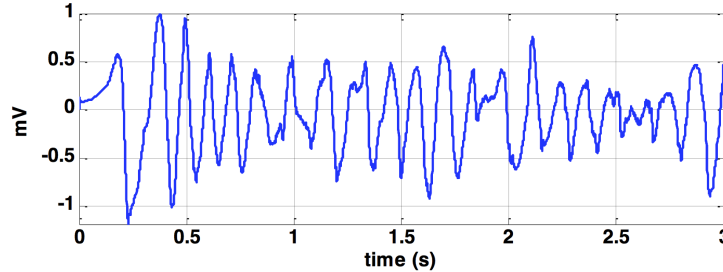
(b) EGM-ICD VF recording

Figure 1.6: *VF recording from an ECG (a) and a monopolar EGM from an ICD (b).*

states that the VF dynamics are the cause of multiple interaction between multiple wavefronts [19]; and the rotor theory, which explains the activation of the ventricles at exceedingly high frequency by the existence of rotors that may drift at high speeds producing changes in the beat activations sequences, or may be quasi–stationary and their wavefronts breakup at varying distances [28].

Recordings of VF, both in ECG and EGM signals, are characterized by irregular changes in the morphology complexes, namely in amplitude and frequency [28]. Figure 1.6 shows examples of VF on ECG (a), and on EGM from an Implantable Cardioverter Defibrillator (ICD) (b).

Even though VF is usually described as a fractionated and chaotic heart activity, some studies state that there is some spatial-temporal organization [29]. Frequency domain analysis of VF characterize the periodicity and irregularity of the VF in a similar way as in the AF. VF is characterized by a spectral distribution concentrated in the band between 3 and 7 Hz. VF signals have to be preprocessed to remove base wander line and high frequencies, above 15-20 Hz [30]. The main measures used in the VF frequency domain analysis are: fd, which is the frequency for which the absolute value of the Power Spectral Density (PSD) occurs [23, 30, 31]; and ri is defined as the ratio power in a 75% bandwidth around the fd, to the power of the [1–15] Hz band [2].

1.4   Heart Rate Variability

HRV is the term used to describe the variations in the time intervals between consecutive heart beats. HRV is usually studied by analyzing the RR-interval time series (beat-to-beat time interval) derived from the ECG. The extraction of the RR-intervals from the ECG can be achieved by mea-
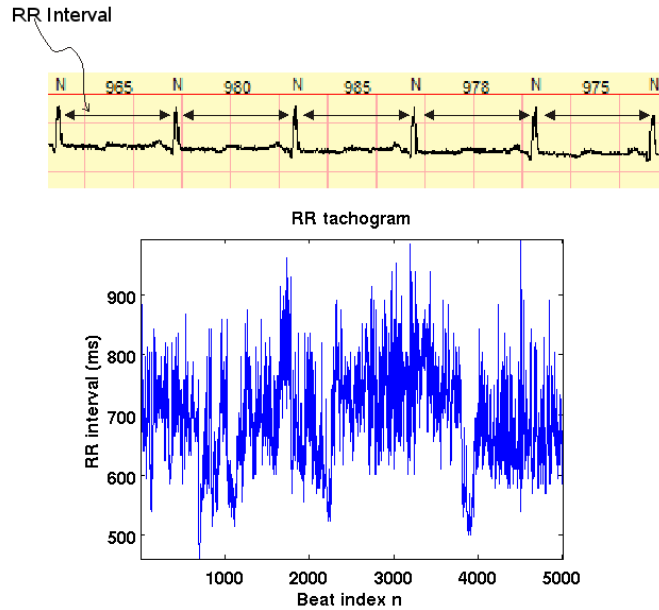
Figure 1.7: *RR intervals time series extracted from an ECG. The N label means normal beat. The time intervals between successive beats are in milliseconds.*

suring the time intervals between QRS complexes, which are the electrical marks registered in an ECG when a cardiac beat occurred. RR-interval time series (sometimes called RR tachogram) is usually constructed as a function of the interval number [32] see Figure 1.7.

HRV is due to the activity of the SA node, as the source of the repetitive impulses that generate the normal beats [33]. The SA node is in turn influenced by the ANS, namely by the parasympathetic and sympathetic branches, which interact in a complex way with a variety of reflexes and systems [34]. The general behavior is outlined in Fig 1.8. HRV has been suggested as a noninvasive tool to assess the state of the system that controls the heart rhythm and its relationship with cardiovascular mortality [4].

The clinical relevance of the HRV has been established in several studies. Hon and Lee reported in 1965 that fetal distress was preceded by alterations in the interbeat intervals. Wolf *et al.* established in 1977 an association of higher risk of post-infarction mortality in patients with reduced HRV [4, 35]. Indeed, it has been shown that low HRV is associated with some cardiac illness: myocardial infarction, atherosclerosis, heart failure, and even with ageing [36].

The underlying assumption, when studying HRV, is that short-term and long-term variations in HR have different physiological origins and the magnitude of these variations has been shown to be indicative of the autonomic state of the subject [37]. For instance, after a myocardial infarction, the innervation level of the heart decreases, and part of the nervous control of this organ can be lost. The HRV reflects this control loss and it makes possible the classification of SCD risk groups [35]. The degeneration of the ANS due
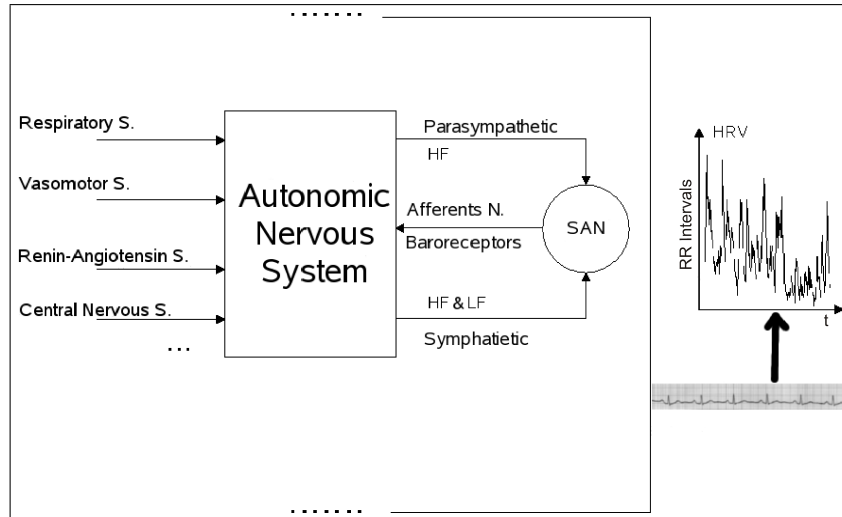
Figure 1.8: *HRV is due to the SA node activity which is modulated by the complex interactions between various systems.*

to the ageing can also be inferred by the analysis of the HRV. Therefore, it would be possible to characterize different cardiovascular states by just measuring the HRV.

The methods used in HRV analysis can be very roughly divided into three main groups, namely, time-domain methods, frequency-domain methods, and nonlinear methods.

Time-domain methods are the simplest ones in computational terms. They treat the RR-interval sequence as an unordered set of intervals and employ different techniques to express the variance of such data. They can be split into two categories [4]: *statistical descriptors*, and *geometrical descriptors*. Table 1.1 summarizes the most common time-domain descriptors for characterization of HRV, whereas Table 1.2 summarizes the most common geometrical descriptors.

Frequency-domain methods are based on PSD estimation, which provides the basic information on how the power (i.e. the variance) is distributed as a function of frequency [38]. The different systems modulating the HR (i.e. modulating the behavior of the ANS) oscillate spontaneously with specific frequencies. Thus, when the PSD is taken from a HRV signal, it is expected to extract information on those systems related to cardiac autonomic function, that is, to identify the harmonic frequency components that correspond to each system. It is possible, for example, to quantify the power of the different spectral components in PSD as a measurement of the contribution of each system to the global variability [11, 39, 40].

PSD is generally estimated from the RR-Interval time series. Since it is a representation of the beat-to-beat variability, it is inherently a discrete and uneven time series (this is the reason for the *variability*). However, almost all of the PSD estimation methods require evenly sampled data. The two usual approaches are:

Descriptor	Units	Description
AVNN	ms	Mean of RR intervals.
SDNN	ms	Standard deviation of all RR intervals.
SDANN	ms	Standard deviation of the averages of RR intervals in all 5 minute segments of the entire recording.
SDNNindex	ms	Mean of the standard deviations of RR intervals for all 5 minute segments.
RMSSD	ms	The Square root of the mean of the sum of the squares of differences between adjacent RR intervals.
NN50		Number of pairs of adjacent RR intervals differing by more than 50 ms in the entire recording.
pNN50	%	NN50 divided by the total number of NN intervals.

Table 1.1: *Statistical descriptors of the HRV.*

Descriptor	Units	Description
Triangular index	ms	Total number of all NN intervals divided by the maximum of the histogram of all RR intervals.
TINN	ms	Base width of the minimum square difference triangular interpolation of the highest peak of the histogram of all RR intervals.
Lorenz plot scattering	ms	Representation of each RR interval duration versus the duration of the previous interval.
Differential index	ms	Difference between the widths of the histogram of differences between adjacent RR intervals measured at selected heights.
Logarithmic index		Coefficient φ of the negative exponential curve $K \exp^{-\varphi t}$ best approximation of the histogram of absolute differences between adjacent intervals.

Table 1.2: *Geometric descriptors of HRV.*

- To assume that the data are, in fact, evenly sampled, and then apply the PSD techniques directly to the RR-Interval time series. However, the units in frequency domain are not anymore Hz. It has been called, instead, *beatquency domain* [41]

- To interpolate and re-sample the RR-Interval time series in order to obtain an evenly sampled time series and then apply PSD techniques
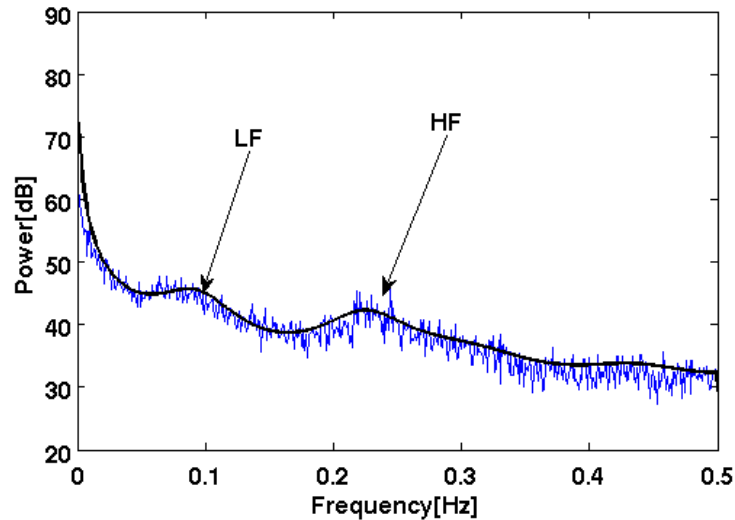
Figure 1.9: *PSD estimation of the same RR-tachogram. Comparison between nonparametric methods (fine line) and parametric methods (bold line), Welch periodogram and AR model respectively.*

on evenly data [11]. In this approach, the units are Hz.

The spectral analysis of HRV may be applied to short-term recordings, often 5 minutes segments, or to long-term recordings, usually 24 hours recordings, which is the standard for Holter recordings in clinical environment. In short-term recordings, the PSD estimation shows three main spectral components [4, 42, 43]:

1. Very Low Frequency (VLF): dc–0.04 Hz.

2. Low Frequency (LF): 0.04–0.15 Hz.

3. High Frequency (HF): 0.15–0.4 Hz.

Table 1.3 shows indices in the frequency domain.

The PSD measures in the LF and HF bands are closely associated with autonomic balance. An increase in parasympathetic activity is primarily related to an increase of the HF power, whereas an increase in sympathetic activity is related to an increase of the LF power. However, it is also accepted that the LF band has influences from the parasympathetic activity [11, 39], see Figure 1.9. The ratio between the power corresponding to the two components serves as an index of autonomic balance [4].

Power spectral analysis of the HRV in long-term recordings (24 hours) includes an ultra-low frequency component (ULF), in addition to VLF, LF, and HF components. The oscillations in the ULF and VLF bands are thought to be due to long-term regulatory mechanisms such as the thermoregulatory system, the renin-angiontensin system and other factors, but the exact relation is not clear [39].

Descriptor	Units	Description	Frequency range
5-min total power	ms^2	The variance of RR-intervals	$\leq 0.4\ Hz$
VLF	ms^2	Power in VLF band	$\leq 0.04\ Hz$
LF	ms^2	Power in LF band	$0.04 - 0.15\ Hz$
LFnorm	n.u	Normalize LF power	
HF	ms^2	Power in HF band	$0.15 - 0.4\ Hz$
HFnorm	n.u	Normalize HF power	
LF/HF		Ratio LF[ms^2]/HF[ms^2]	

Table 1.3: *HRV frequency domain indices.*

Descriptor	Description
	Chaos Theory
Correlation Dimension	Fractal dimension of the attractor in the sate space.
Lyapunov exponents	Sensitive dependence on initial conditions.
	Fractal time series
$1/f$ spectrum	Long-term correlation analysis frequency domain.
Dentrended fluctuation analysis	Long-term correlation analysis.
	Entropy
Approximate Entropy	Irregularity assessment.
Sample Entropy	Irregularity assessment.
Multiscale entropy	Irregularity assessment at different time scales.

Table 1.4: *HRV Nonlinear indices.*

Nonlinear methods to assess the HRV have been proposed recently. The rational can be explained because the irregular and complex HR fluctuations observed during normal SR in healthy subjects, even at rest, are due in part to deterministic chaos, and that a variety of diseases may involve a (paradoxical) decrease in this type of nonlinear variability [44, 45]. Linear methods do not provide information on nonlinear structures, since they assume that the time series under study is the output of a linear system. Therefore, the methods based on chaos theory and nonlinear theory have gained recent interest, in order to extract all the information that the HRV signal conveys.

Nonlinear measures used in HRV analysis can be divided into three categories, namely, chaos theory indices, fractal indices and indices from information theory. Table 1.4 shows a short list of indices commonly found in HRV literature.
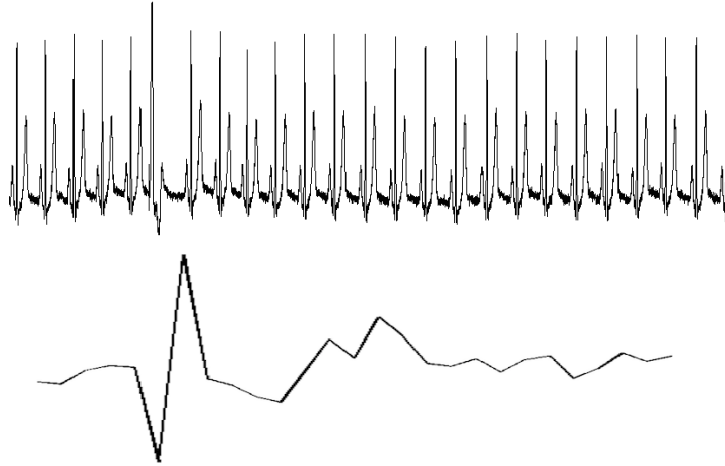
Figure 1.10: *Example of an ECG with the presence of a VPC (top) and the RR-Interval time series representation (bottom).*

1.5   Heart Rate Turbulence

The term HRT was firstly used by Schmidt *et al.* [5] to describe the short-term fluctuations in sinus HR that occur following VPCs [6]. Figure 1.10 shows an example of an ECG with a VPC (top) and the RR-interval time series (bottom). Even with the presence of noise, it is clearly visible the biphasic response of the HR on the RR-interval time series after the VPC and the compensatory pause.

In normal subjects, sinus rate initially accelerates and then decelerates compared with the HR previous to the VPC. Finally, the HR returns to the baseline. Figure 1.11 shows a, somewhat, clean example of RR-interval time series and the different parts of the HRT. This RR-intervals sequences comprising 5 sinus RR-intervals before VPC, the compensatory pause, and subsequent 15 (or 20) sinus RR-intervals, is usually called VPC-tachogram.

The physiological mechanism of HRT is supposed to be based on a baroreflex source, which has been confirmed in the literature [5, 6]. According to this, systolic blood pressure produced by the VPC is lower than previous beats, which leads to an inefficient baroreflex input. In turn, it causes vagal inhibition, increasing the HR [6]. Subsequent deceleration is due to the ensuing compensatory pause and the increase in blood pressure, which induce a vagal stimulation and sympathetic withdrawal [46].

HRT is usually assessed in Holter recordings. A previous step to remove inadequate VPC-tachograms is required for obtaining accurate HRT measurements. The guidelines indicate to remove a VPC-tachogram when one of the following conditions are fulfilled [47]:

- The five sinus beats preceding the VPC and the 15 sinus beats following the compensatory pause include some arrhythmia, artifacts or false classifications.
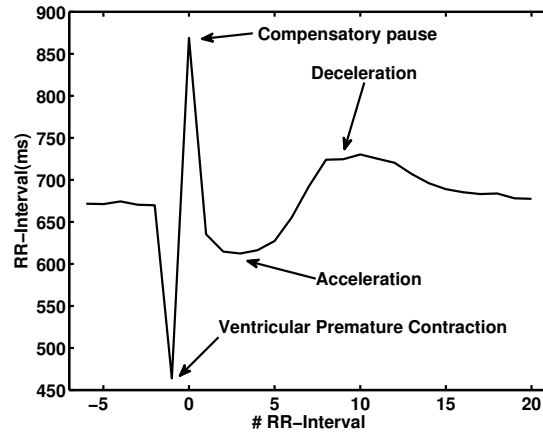
Figure 1.11: *Biphasic response after a VPC in an RR-interval time series. After the VPC there exists a compensatory pause following by the HRT response: early acceleration and late deceleration.*
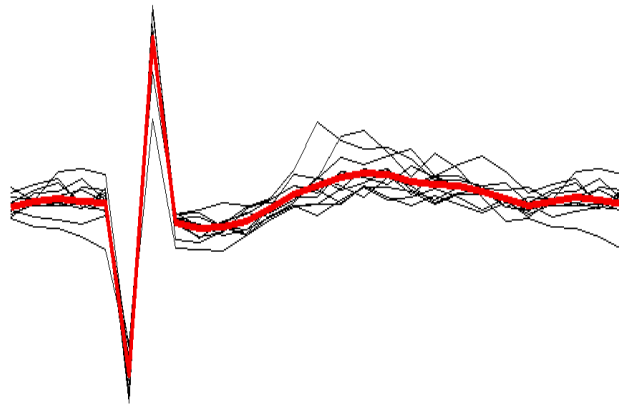
Figure 1.12: *Example of the averaging procedure to improve the signal-to-noise ratio. The thick line represents the average of all available individual VPC-tachograms.*

- RR-intervals < 300 ms.

- RR-intervals > 2000 ms.

- Difference between consecutive RR-intervals higher than 200 ms.

- Difference between any RR-interval and the reference interval (mean of the five sinus intervals preceding the VPC) higher than 20%.

- Prematurity smaller than 20% of the reference interval.

- Compensatory pause smaller than 20% of the reference interval.

The next processing step is to remove background effects and noise present on individual VPC-tachograms. The usual procedure is to average all the available VPC-tachograms to improve the signal-to-noise ratio.

(a) TO (b) TS

Figure 1.13: TO (a) and TS (b) HRT parameters. TO quantifies the early acceleration, while TS quantifies the late deceleration.

(a) $Healthy$ (b) $High-risk$
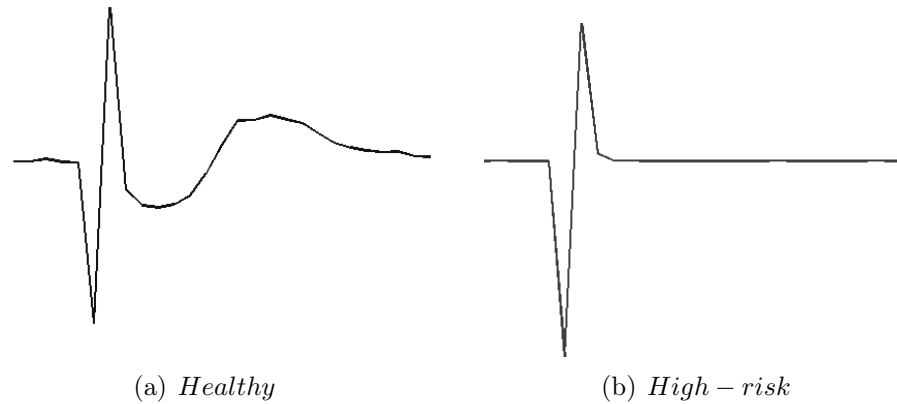
Figure 1.14: *Averaged VPC-tachogram for a healthy subject (a), and for a patient at high-risk after a myocardial infarction (b), in which HRT is blunted.*

A minimum of five VPC-tachograms is required to perform the average [47], see Fig. 1.12.

The first phase of the HRT (early acceleration) is quantified by Turbulence Onset (TO), which is calculated using the following equation:

$$TO = \frac{(RR_1 + RR_2) - (RR_{-2} + RR_{-1})}{RR_{-2} + RR_{-1}} \times 100[\%] \qquad (1.1)$$

where RR_{-2} and RR_{-1} are the two RR-intervals immediately preceding the VPC coupling interval, and RR_1 and RR_2 are the RR-intervals immediately following the compensatory pause, see Figure 1.13(a). The second phase of the HRT (late deceleration) is quantified by Turbulence Slope (TS), which is the slope of the steepest regression line observed over any sequence of five consecutive RR-intervals within the first 15 sinus rhythm RR-intervals after the compensatory pause, see Figure 1.13(b).

Patients at high risk showed an attenuated HRT or even entirely missing. This difference on the HRT response has been proven to be a powerful predictor of mortality and SCD [5, 48]. Figure 1.14 shows two averaged

VPC-tachograms, the left (right) panel corresponding to a healthy subject (to a patient at high-risk after miocardial infarctin). High-risk patients are characterized by depressed HRT, expressed as the lack of an immediate acceleration, or even deceleration of a sinus rhythm (positive values of TO), and an attenuated subsequent deceleration with lower TS values (flattened slope) [49]. It has been suggested that HRT, being a vagally-dependent effective measure of baroreflex sensitivity related to the advancement of heart failure, might be used as a marker of congestive heart failure progression. Indeed, in patients with heart failure regardless of etiology, HRT consistently predicted heart failure progression and all cause mortality [49]. HRT seems to be particularly useful in identifying high-risk patients with preserved left ventricular function, the group not covered by current indications for ICD. ISAR-HRT [48] was the first study that showed independent role of the HRT in predicting mortality not only in patients with significantly decreased Left Ventricular Ejection Fraction (LVEF), but especially in those with LVEF above 30%.

Part II

Signal Processing Methods for Fibrillatory Arrhythmias

Chapter 2

Ventricular Fibrillation Characterization with Fourier Organization Analysis

2.1 Introduction

Analysis of intracardiac EGMs in cardiac electrophysiology has often been addressed by using time domain parameters, such as activation times and voltage amplitudes [50, 51]. Early descriptions of EGM in the frequency domain had few implications for clinical practice [29, 52], however, there has been a recent increase in interest in its application to the clinical environment, and several clinical targets for AF ablation use the EGM spectral representation. These targets aim to give a regular description in the frequency domain in terms of low CL and/or high regularity regions [2, 22]. Such spectral features have been used both in electrical and in optical mapping recordings, during AF and VF [16, 53, 54, 55, 56]. In [57], EGM from ICDs were also analyzed during SR and ventricular tachycardia (VT).

Two complementary approaches have been mainly followed in spectral analysis applied to cardiac mapping systems: DFA and OA [16, 25]. The former aims to characterize the EGM periodicity using the averaged CL of a non-purely periodic rhythm (usually AF or VF), whereas the latter quantifies the signal energy that remains unexplained by that periodicity. However, these descriptions have often discarded relevant information of the spectrum, such as the harmonic structure or the spectral envelope. Moreover, it is not always guaranteed that a dominant frequency will give a good estimation of the averaged CL. In [58], the authors show that there is a poor correlation between the EGM average CL and the dominant frequency in patients with persistent AF. These drawbacks can lead to incomplete understanding of the information in DFA and OA spectral parameters, which are further explored in this chapter.

A unified, simple, and automatic processing algorithm is proposed for: (1) improving the parameters estimated from DFA and OA; and (2) giving more detailed information about the spectral EGM structure. The proposed

method, called FOA, uses a LS approximation of the EGM using a modified harmonic Fourier Series signal model, closely related to the OA description, accounting for narrow band fluctuations of each component in the Fourier Series. The fundamental frequency, used in our method as an estimation of the inverse of the CL, is first estimated according to the best LS fit to the EGM as a function of the signal model in terms of this parameter. Then, a set of parameters from the best model is used to describe the spectral structure and organization of the signal.

2.2   Background

Spectral parameters for DFA and for OA have been defined under the implicit assumption that the underlying signal consists of an almost-periodic component plus an irregular component [16, 25]. On the one hand, DFA aims to determine the averaged CL of the almost-periodic component in an EGM, and for this purpose, f_d has been defined as the frequency of the maximal absolute value of its spectrum $P(f)$. The parameter f_d is obtained either directly from the EGM spectrum, or by using an auxiliary signal, obtained by filtering and rectifying the EGM [23]. This last method is commonly used as an automatic procedure for obtaining the averaged CL estimation of an EGM. An additional parameter, called dominant frequency bandwidth $bw(f_d)$, is sometimes obtained. This parameter is defined as the difference between the upper and lower frequencies for which the spectral maximum peak falls to 75% of its value.

OA takes a different approach and aims to measure the relative contribution of the almost-periodic component of an EGM in terms of its signal power. Conventional organization parameters are defined in the frequency domain. The first step of the calculation is to estimate the underlying CL (usually from DFA). Next, the power of the components in a predetermined narrow band around either the fundamental peak or the harmonic peaks, is used to account for the relevance of the almost-periodic component. Typically two parameters are used. The parameter ri, which was originally defined as the ratio of power in the dominant frequency bandwidth, and the total power in the band of interest. In this work we use the the B band (2–30 Hz for AF, and 2–15 Hz in VF) [2, 24]. Later, oi was defined. This is the ratio of the power in the fundamental frequency bandwidth, combining up to four harmonic peaks, and the total power in the B band [25, 26].

Though highly informative, the parameters yielded by DFA and OA (f_d, $bw(f_d)$, oi, and ri) give an incomplete spectral description of the signals. Another important descriptor is the spectral envelope, which for a purely periodic signal is given by the Fourier Transform of a single cycle. For an almost-periodic signal, the spectral envelope is still (roughly) related to the averaged Fourier Transforms of consecutive cycles. For EGM analysis purposes, the spectral envelope can be seen as the spectrum of an isolated arrhythmia complex, which is dependent on the morphology of the EGM,

but independent from its CL.

In a purely periodic signal, harmonic frequencies are the integer multiples of fundamental frequency f_0, that is, $f_k = k f_0$. DFA and OA parameters have been used to analyze the differences between spontaneous and induced VF episodes [59], and to study the self-termination of VF episodes [60] in ICD stored EGM. The spectral envelope yields a spectral representation that has no harmonic structure, and hence it contains explicit information about the underlying physiological phenomena, as well as about the acquisition characteristics. In some works, the spectral profile of the harmonics showed significant differences between patients with inferior and anterior myocardial infarction, whereas the differences in f_d, f_d from DFA, hereafter called f_{d_DFA}, and *oi* were non-significant [61]. There are other works where the spectral envelope is used as a feature in a discrimination scheme of ventricular arrhythmias [62, 63].

Parameters from DFA and OA can even become inaccurate in some conditions, given that f_d will not always be the same as f_0. This risk holds, even when using the automatic algorithm in [23]. An operating definition for f_0 in the presence of harmonic structure was presented in [59, 60, 61]. It is defined as the averaged inter-harmonic separation. According to the theoretical properties of the Fourier Transform of periodic signals this yields an estimation of the inverse of the CL, when harmonic structure is present in the EGM [64]. This definition of fundamental frequency, however, has not yet been implemented in an automatic signal processing algorithm.

2.3   Fourier Organization Analysis

In this section, FOA algorithm is proposed, as a generalized version of both DFA and OA, by using the well-known principles of spectral analysis and signal approximation. First, the signal model and the approximation using LS principles are presented. Then, strategy for automatic estimation of f_0 is detailed. Finally, periodicity and organization EGM parameters used within the FOA algorithm are described.

2.3.1   Fourier Organization Analysis Signal Model

Let $EGM(t)$ be a continuous time EGM signal. If it was a purely periodic signal with fundamental period T_0, its Fourier Series representation would be given by $EGM(t) = \sum_{k=1}^{K} A_k \cos\left(2\pi \left(k f_0\right) t + \phi_k\right)$, where $f_0 = 1/T_0$ is the fundamental frequency. A_k and ϕ_k representing the amplitude and phase for each harmonic component respectively. K represents the number of harmonics.

Three additional elements can be introduced into this signal model. First, additive noise can be present, denoted by $e(t)$. Second, a digitized version of $EGM(t)$ during a given acquisition time interval is used, which yields N samples acquired at a rate of f_s samples per second. Under these conditions,

the spectral resolution of a nonparametric Fourier-based spectral analysis procedure is about $\Delta = f_s/N$ Hz. Third, $EGM(t)$ will not be purely periodic in real recordings, but it will be almost or near-periodic. This can be observed by the presence of narrow-band structure (harmonic peaks) in the signal spectrum.

In the case of OA parameters, spectral components in a narrow bandwidth of the spectral peaks contribute to the quantification of the signal regularity, e.g., ri, as defined in [2]. It is computed by taking into account the power at the dominant frequency and at its adjacent frequencies. In a Fourier-based spectral analysis this correspond to the spectral resolution Δ. A similar idea can be included in our model, by considering two additional sinusoidal components for each harmonic peak, whose frequencies are the harmonic component plus and minus Δ Hz. The signal model for $EGM(t)$ is given by:

$$
\begin{aligned}
EGM(t) = {} & \sum_{k=1}^{K} A_k \cos\left(2\pi(kf_0)t + \phi_k\right) \\
& + \sum_{k=1}^{K} A_k^- \cos\left(2\pi(kf_0 - \Delta)t + \phi_k^-\right) \qquad (2.1) \\
& + \sum_{k=1}^{K} A_k^+ \cos\left(2\pi(kf_0 + \Delta)t + \phi_k^+\right) + e(t)
\end{aligned}
$$

where $A_k^+, A_k^-, \phi_k^+, \phi_k^-$, are the amplitudes and phases related to the near-periodicity associated with the harmonics. This signal model can be expressed in an abbreviated form, $EGM(t) = s_{f_0}(t) + e(t)$, where $s_{f_0}(t)$ denotes the organized or near-periodic component of $EGM(t)$ that is associated with f_0. Recall that f_0 corresponds to the inverse of the averaged CL, or fundamental period T_0, in the time domain. The model parameters $\{A_k, A_k^+, A_k^-, \phi_k, \phi_k^+, \phi_k^-\}$ can be estimated by using the discrete-time version of the EGM, (2.1), i.e, $EGM[n] = EGM(n/f_s)$, where $n \in \mathbb{Z}$ is a discrete-time integer index, by using a LS projection onto a Hilbert signal space of sampled sinusoids containing the fluctuations. Therefore, a Fourier Series expansion is proposed that considers two additional sinusoidal neighbour components for each harmonic component, the coefficients for this expansion being estimated using LS.

In order to use the FOA signal model in (2.1), the following steps are necessary:

1. *Estimation of f_0 and periodicity description.* This step provides the estimation of the main rhythm. An automatic method is proposed that searches for the argument that minimizes the Mean Square Error (MSE) for FOA signal model in (2.1) as a function of f_0.

2. *Signal model fitting and organization description.* In this step, FOA signal model is fitted to the EGM, using f_0^* as estimated in the previous step. The coefficients of the signal model are again computed

by LS procedure. Therefore, coefficients are estimated by minimizing, $\|S\mathbf{a} - EGM\|_2$, where $\mathbf{a}$ are the coefficients of the model, $\mathbf{a} = \{A_k, A_k^+, A_k^-; k = 1, \ldots, K\}$; S is the matrix of sine and cosine base signals, and EGM is the column vector EGM. Coefficients are estimated by using the Moore-Penrose pseudoinverse, $\mathbf{a} = (S^T S)^{-1} S^T EGM$.

These steps are further explained in the next subsections.

2.3.2   Automatic Estimation of f_0

FOA signal model has assumed that f_0 is known, but in practice f_0 is also an unknown parameter and it has to be estimated. A simple automatic estimation method is proposed using the FOA signal model, consisting of fitting the signal model in (2.1). Fitting means, it is needed to calculate coefficients using LS, for a set of values of f_0 in an adequate frequency range for search, $f_0 \in [f_l, f_h] \, Hz$. Let us denote the signal model fitted for each f_0 in that range, by $\hat{s}_{f_0}(t)$. The MSE between the signal and the fitted model is computed as a function of f_0, this is, $MSE(f_0) = \|EGM[n] - \hat{s}_{f_0}[n]\|^2$. The best value of f_0 is then the argument that minimizes $MSE(f_0)$:

$$f_0^* = \arg\min_{f_0} MSE(f0), \quad f_0 \in [f_l, f_h] \text{ Hz.} \tag{2.2}$$

where f_0^* is the optimum value to be used as the fundamental frequency for the FOA signal model (see Fig 2.2).

   In some cases, subharmonics of f_0 have been observed to give low MSE values, yielding inadequate f_0^* estimations. These cases can be readily identified and corrected by noting that the spectral profile becomes a strongly oscillating series.

2.3.3   Fourier Organization Parameters

The implicit relationship between the signal model in (2.1) and parameters oi and ri, allows us to define an index for quantifying the regularity of the signal. This is given by the power ratio between the near-periodic component and the EGM. For the estimated fundamental frequency f_0^*, the model is fitted to the signal using LS procedure, and then, the EGM can be modeled as:

$$EGM[n] = \hat{s}_{f_0^*}[n] + e[n] \tag{2.3}$$

   Take energy ratios, and then regularity coefficients are calculated as:

$$p_1 = \frac{\|\hat{s}_{f_0^*}[n]\|^2}{\|EGM[n]\|^2}, \quad p_e = \frac{\|e[n]\|^2}{\|EGM[n]\|^2} \tag{2.4}$$

Note that p_1 is just a generalization of oi and ri parameters. Note also that p_e accounts not only for the noise, but also for any additional component not included in p_1 and not related to f_0^*. Previous parameters quantifying

organization (oi and ri) implicitly assume a defined periodicity in the signal, hence organization being referred to the quantification of the agreement with that periodicity. A similar framework is followed for parameter p_1 measuring the agreement of the signal with periodicity in f_0. This represents an operative definition for the organization concept, in which periodicity and organization are jointly searched, and the chosen periodicity is given by the higher organization that can be obtained from the adjustment of the near-harmonic signal model.

Other spectral parameters can be readily obtained from signal model (2.1). Trivially, dominant frequency is simply the frequency for which the maximum spectral amplitude occurs, this is, $f_d = \arg\max_f\{A_k^-, A_k, A_k^+; k = 1, \ldots, K\}$. The set of modulus parameters as $M_k = A_k^- + A_k + A_k^+$ can also be defined, which represents the modulus for the kth component, taking into account the kth harmonic and its corresponding sinusoidal fluctuation components.

A good estimation of f_0^* is a fundamental step in the spectral analysis of EGM signal recordings, since not only does this parameter accounts for the CL, but also all the other organization parameters are directly related to it. This holds also for DFA and OA parameters. As previously stated, the use of f_d instead of f_0^* can be misleading in EGM with non-low-pass spectral envelopes, and even the use of the automated algorithm in [31] can give incorrect estimates if it is not subsequently supervised. In particular, when applying FOA, slight deviations from an adequate value of f_0^* will reduce the value of the p_1 coefficient, leading to inaccurate interpretations of the EGM organization and irregularity. The number of harmonics (K) to be used in the model is also a practical issue, and it has to be previously fixed. Is is estimated by dividing the signal bandwidth to the value of f_0^*.

In summary, FOA is closely related to conventional nonparametric spectral analysis and to DFA and OA. Its main advantage is that FOA gives a unified and detailed description of the spectrum and organization by the application of an automatic algorithm.

2.4   Simulations

2.4.1   Computer Model

A computer model [65] was used to simulate examples of monopolar and bipolar EGM recorded in different and simple electrophysiological conditions (see Fig. 2.1). In brief, a rectangular grid of 1×2 cm (80 cell groups per cm) was constructed for discretizing a 2-dimensional tissue model. Excitation dynamics were given by a cellular automaton with three states (rest, activated, refractory), where transitions were controlled by static restitution curves of the action potential duration and of conduction velocity in terms of the diastolic interval. Voltage levels were calculated by using a prototype action potential, whose time duration was modified according to restitution
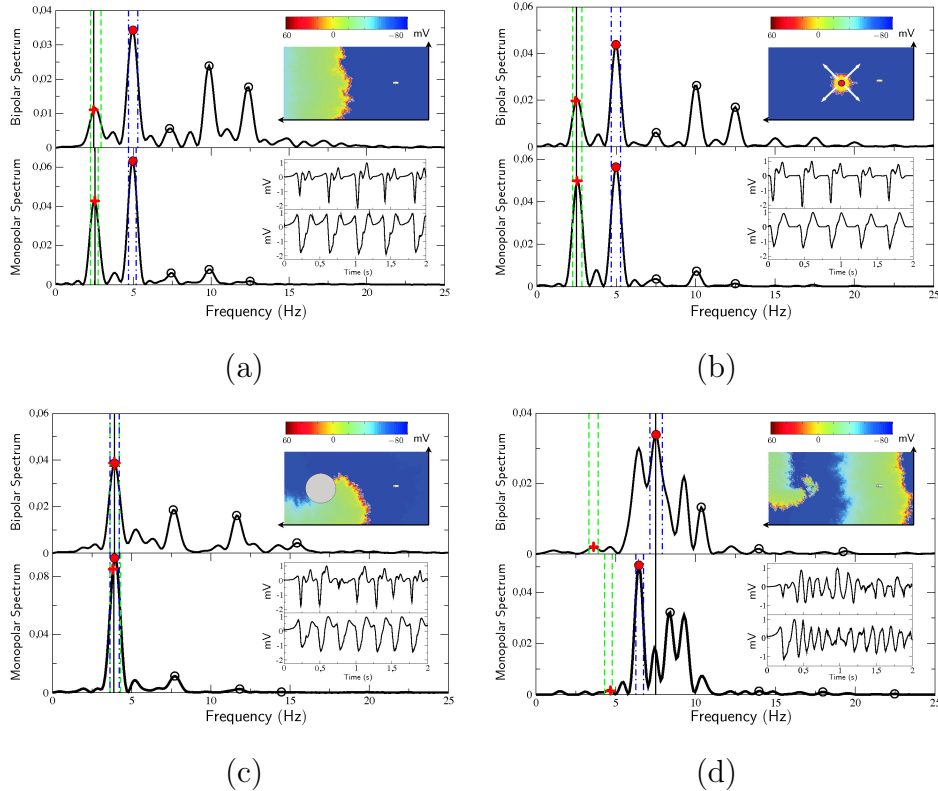
Figure 2.1: *Simulation results: EGM and spectra, for bipolar and monopolar recordings in each simulated electrophysiological condition: (a) Plane wavefront; (b) Focal activation; (c) Anchored rotor; (d) Fibrillatory conduction. Spectral peaks are denoted by crosses (f_{d_DFA}), solid circle (f_d), and 3rd to 5th harmonics (empty circles) estimated by DFA-OA method. Dotted vertical lines in the spectra indicate $bw(f_{d\_DFA})$ and $bw(f_d)$. Solid vertical lines in the spectra indicate f_0 estimated by FOA method. Inbox subpanels show a snapshot of the action potential simulation (upper) and the simulated EGM (lower).*

properties. Diffusion rules yielded action potential propagation along the tissue. An EGM recording model, according to the volume conductor equation in a homogeneous medium [66], was tuned for modeling simultaneous monopolar and bipolar recordings. A monopolar electrode was placed at $x = 1.5$ cm, $y = 0.5$ cm, 0.2 cm height. The bipolar electrode configuration consisted of that electrode at the positive pole, and a negative electrode at $x = 1.52$ cm, $y = 0.52$ cm, 0.2 cm height. Simulated EGM were recorded at 1600 samples per second (see [65] for details).

Several electrophysiological conditions were simulated: (1) Sustained line stimulation from the left border (pacing rate of 400 ms), yielding a plane wavefront; (2) Point stimulation (pacing rate of 400 ms) from a focal point at $x = 1$ cm, $y = 0.5$ cm; (3) Anchored rotor around a circular obstacle (0.4 cm diameter infarcted region); (4) Fibrillatory activity. The two last conditions were generated by using a standard $S1 - S2$ stimulation protocol, and the
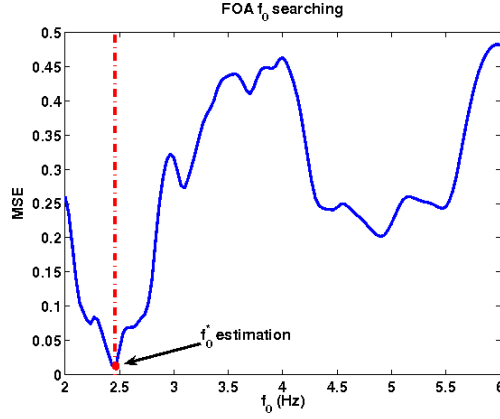
Figure 2.2: *Example of MSE for estimating f_0^* in plane wavefront EGM simulation with FOA procedure. Note that the better the f_0 estimation, the lower MSE.*
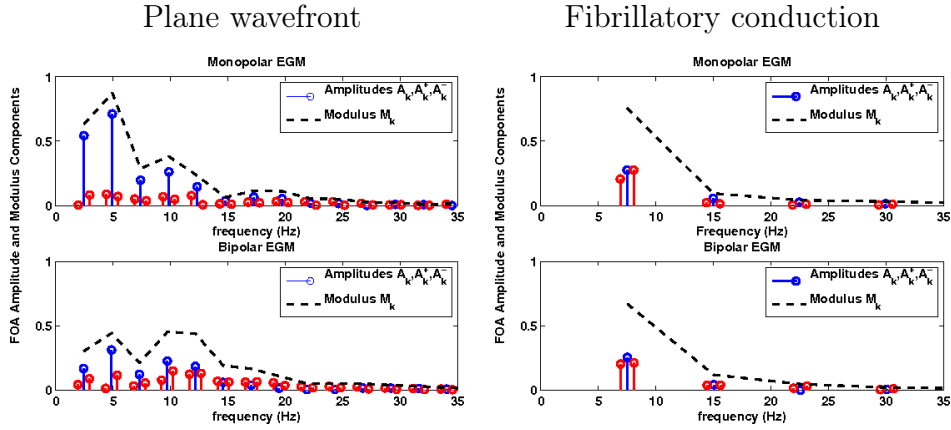
Figure 2.3: *Simulation results: Spectral envelope using amplitude and modulus components from FOA, for bipolar (up) and monopolar (down) recordings in Plane Wavefront and Fibrillatory Conduction. Parameters M_k have been interpolated with splines for visualization and comparison purposes.*

simple tissue and acquisition model contained all the necessary information for an easy comparison between the tissue activity and the recorded EGM in these example conditions [65]. Each simulation was run for 2 seconds, as this was long enough duration to include several cycles of tachycardia and fibrillation in all cases.

2.4.2   Analysis Methods

The FOA algorithm applied to the simulated EGM signals consisted of the steps described previously in Sec. 2.3. Specifically, f_0^* was first estimated, the signal model in (2.1) was then fitted using LS, and organization (p_1 and p_e) and spectral envelope ($M_k, f_d, A_k, A_k^+, A_k^-$) parameters were obtained. Figure 2.2 shows an example of MSE as a function of f_0 in FOA procedure,

		Plane		Focal		Anchored		Fibrillatory	
		M	B	M	B	M	B	M	B
MFR (Hz)		2.48		2.50		3.88		7.12 / 7.08*	
Time	$CL\ (ms)$	400	400	400	400	250	250	143	125
	$CL^{-1}\ (Hz)$	2.5	2.5	2.5	2.5	4.0	4.0	6.9	8
DFA and OA	$f_{d\_DFA}\ (Hz)$	2.54	2.44	2.54	2.44	3.81	3.91	4.69	3.61
	$f_d\ (Hz)$	4.98	4.98	4.98	4.88	3.91	3.91	6.45	7.52
	$P_n(f_d)$	63	34	56	43	93	39	50	34
	$P_n(f_{d\_DFA})$	43	11	50	20	85	39	2	2
	$P_n(f_2)$	63	34	56	44	11	19	32	34
	$P_n(f_3)$	6	6	4	6	2	3	14	13
	$P_n(f_4)$	8	24	7	26	0.5	11	1	1
	$P_n(f_5)$	2	18	1	17	0.3	.3	0.3	0.7
	$bw(f_{d\_DFA})\ (Hz)$	0.49	0.68	0.59	0.59	0.68	0.59	0.49	0.59
	$bw(f_d)\ (Hz)$	0.49	0.58	0.59	0.59	0.59	0.59	0.49	0.78
	oi	0.99	0.80	0.99	0.92	0.83	0.66	0.53	0.47
	ri	0.45	0.26	0.41	0.30	0.69	0.31	0.32	0.30
FOA	$f_0\ (Hz)$	2.47	2.43	2.50	2.50	3.87	3.90	7.49	7.53
	M_0	0.63	0.30	0.55	0.39	0.99	0.50	0.76	0.67
	M_2	0.87	0.44	0.53	0.49	0.50	0.47	0.10	0.12
	M_3	0.29	0.21	0.17	0.18	0.31	0.50	0.04	0.05
	M_4	0.38	0.45	0.20	0.38	0.15	0.28	0.03	0.02
	M_5	0.23	0.44	0.10	0.30	0.11	0.17	0.01	0.01
	p_1	0.98	0.90	0.96	0.96	0.89	0.77	0.59	0.52
	p_e	0.02	0.10	0.04	0.04	0.11	0.23	0.41	0.48

Table 2.1: *Results of DFA, OA, and FOA, in simulated EGM. Parameters from $P_n(f)$ are reported as its value $\times 10^3$. * The second value was computed averaging action potentials from a square of 9 cells right below the recording electrode.*

for the case of the plane wavefront.

For conventional parameters, the automatic procedure in DFA was used to calculate f_{d_DFA} in a filtered and rectified auxiliary signal obtained from the EGM [23, 25, 26, 31], which estimates f_d in the auxiliary signal. This estimated f_{d_DFA} was used for estimating the CL and to compute OA parameters. A spectral representation $P(f)$ was obtained for each EGM by using Welch periodogram with rectangular windowing, 2048 samples, 50% overlapping. These settings were used because previous experiments (not included here) showed that oi is reduced when time averaging is made us-

ing any windowing different from a rectangular structure. Hence, f_d was obtained as the maximum in the spectral representation of the EGM, and $P_n(f)$ as the unit-area normalized power spectrum at frequency f. Other conventional parameters were $bw(f_{d\_DFA})$, $bw(f_d)$, $P_n(f_0)$, $P_n(f_d)$, $P_n(f_k)$, oi and ri.

The mean firing rates (MFR) of the cell directly below the recording electrode were computed using the action potentials, for each simulated condition. For fibrillatory conduction, the MFR was also calculated using a square of 9 cells directly below the recording electrode. MFR values can also be used as a gold standard for the main rhythm of the simulated EGM.

The averaged CL was also obtained in the time domain by an expert counting the EGM relevant peaks, aiming to establish their relationship with the spectral parameters, and also a means of evaluate the quality of the f_d and f_{d_DFA} from the classical approach and f_0 from FOA.

2.4.3 Simulations Results

Results on Periodicity Parameters. Simulated EGM and their spectra are shown in Fig. 2.1, and Table 2.1 contains their measured spectral parameters for both DFA-OA and FOA procedures. A narrow-line spectral structure was observed in all cases, and a harmonic structure was present in all the recordings, except for fibrillatory conduction.

There was high agreement among f_0 and f_{d_DFA} as estimated by FOA and by DFA, the inverse of CL, and the MFR, for the cases of plane wavefront, focal activation, and anchored rotor. The interharmonic separation between successive peaks in the spectra was also about f_0 Hz in these cases. Parameter f_d, when estimated directly from EGM spectrum, was the same as f_0 and f_{d_DFA} only in the anchored rotor, but in plane wavefront and focal activation f_d corresponded to the second harmonic of f_0.

For fibrillatory conduction, a clear harmonic structure was not observed, and a less narrow-band spectra was present. The inverse of the manually determined CL (6.9 Hz for monopolar, 8 Hz for bipolar) were more related to f_d (6.45 Hz, 7.52 Hz) and f_0 estimated by FOA (7.49 Hz, 7.53 Hz) than to f_{d_DFA} estimated by DFA (4.6 Hz, 3.1 Hz). The agreement between f_0 from FOA, in both monopolar and bipolar, and MFR (7.08 Hz) is an additional indication of the robustness of the proposed method when estimating the main rhythm of EGM in complex conditions. The automatic algorithm for estimating f_{d_DFA} using DFA was seen to fail here. Taking into account that it was still a narrowband spectrum, it could be seen as a single-harmonic spectrum, and hence, the averaged CL would be consistently explained by f_d in this example. The values obtained for f_0 estimated by FOA were very similar for both monopolar and bipolar recordings.

Results on Spectral Envelope. The previously observed differences between f_0 and f_d were explained by the spectral envelopes of the EGM. As seen in Table 2.1 and Figs. 2.1 and 2.3, the harmonic peaks followed a smooth variation in the frequency domain, approximately corresponding to

the spectral envelopes. In fibrillatory conduction, the spectral envelope was significantly different from the profile of the spectral peaks, given that the beat-to-beat variations were considerably higher. Nevertheless, the relative amplitude of the spectral lines was determined by the spectral envelope, and hence, this feature caused f_d to be different from f_0. As shown in Table 2.1, the harmonic peaks followed a profile similar to the FOA modulus.

Spectral envelope mainly depended on two causes, namely, the setting configuration of the acquisition lead system, and the underlying electrophysiological process during each cycle. In our simulations, the same underlying electrophysiological process had a very different spectral shape, depending on the electrode configuration. As an example, the spectral envelope of bipolar EGM in the plane wavefront had a higher spectral content around 12 Hz when compared to the monopolar EGM. These differences between envelopes of different configurations were less evident in fibrillatory conduction, where the underlying electrophysiological activity was a faster, more high-frequency process, enough to partially compensate the effect of the lead configuration on the spectral envelope. Obviously, similar underlying electrophysiological activations will exhibit similar spectral envelopes under the same lead configuration (e.g., plane wavefront vs focal activation examples), but different envelopes with different electrophysiological activations (e.g., plane wavefront vs fibrillatory activity examples).

Results on Organization Parameters. Table 2.1 also shows the parameters related to OA (oi and ri), and parameters p_1 and p_e from FOA. Bandwidth tended to be higher in bipolar than in monopolar EGM. For regular rhythms, organization, as quantified with oi and p_1, was high both for monopolar and for bipolar recordings, with a trend in monopolar EGM to be higher than in bipolar EGM. However, organization was much lower in these recordings as quantified by ri, since this parameter does not consider the organized activity contained in the harmonics. Irregular rhythms exhibited dramatically lower oi and p_1, as expected in fibrillatory conduction. However, since oi is computed from the estimation of f_0, it is necessary to be sure that f_0 is correctly estimated, otherwise the interpretation of oi values could be misleading. The high irregularity of the fibrillatory conduction can be observed from the FOA amplitude components $\{A_1^-, A_1^+\}$ in Fig. 2.3, being very similar to the FOA amplitude component A_1. However, these components were considerably lower than component A_1 for more regular rhythms.

2.5 Results on Clinical Databases

2.5.1 Databases

Two different databases with EGM recordings stored in ICD were used in this study. All the EGM recordings were obtained from patients undergoing the implant of a Medtronic® device in Hospital Universitario Virgen de la Arrixaca of Murcia and in Hospital General Universitario Gregorio Marañón of Madrid, Spain. For each analyzed episode, two simultaneously recorded
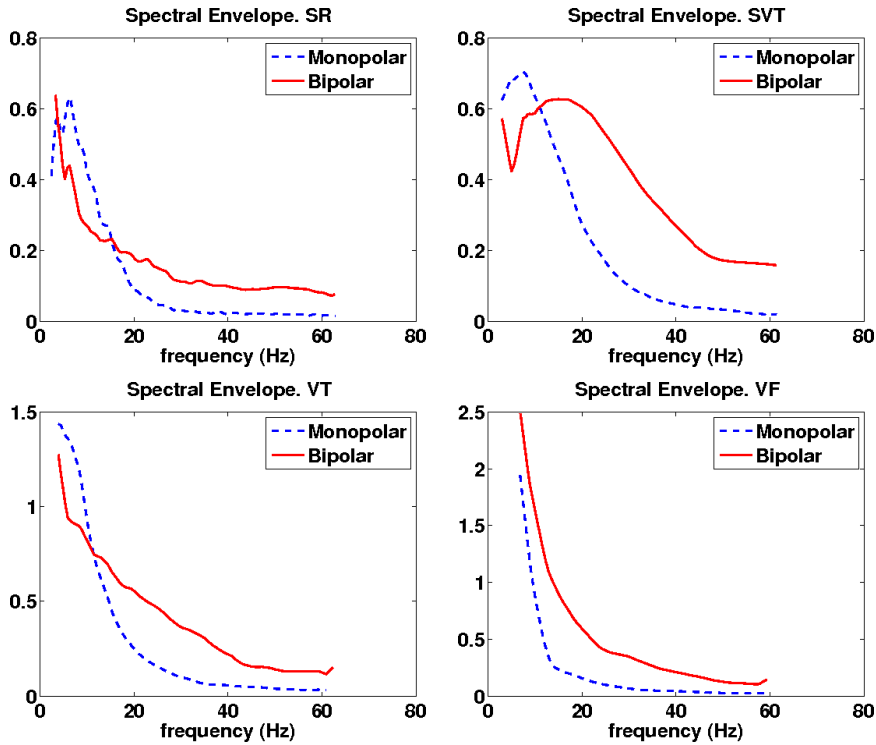
Figure 2.4: *Spectral envelopes (using spline interpolated amplitudes) of the FOA signal model for the database with different rhythms.*

EGM were available in the device, with pseudo-monopolar (from can to coil) and bipolar (from tip to ring) configurations, at 128 samples per second. Recordings included in the study were revised and classified by an specialist.

There is little information in the literature about regularity measurements for other rhythms than VF, as given by the ECG or the EGM waveforms. However, it is widely known that the SR has a fluctuating magnitude due to HRV, and also, VT are known to be less stable in instantaneous rhythm than SVT.

The first clinical database consisted of EGM during four different rhythms, namely, 5 SR, 8 SupraVentricular Tachycardia (SVT), 8 VT, and 7 VF. AF recordings were discarded for this study, whereas SVT and VT were collected by requiring relatively stable episodes along the whole recording. Additionally, SVT were considered in which a similar morphology to sinus rhythm could be observed, and VT were recognized by an expert in those episodes with very different morphology from SR. Only one episode per patient was considered, and small yet balanced groups were assembled. The analysis in this database aimed to assess the performance of FOA procedure in sustained and non-sustained rhythms, with some similarity to the simulation conditions in the preceding sections. All EGM recordings in this database had the same length (6 seconds), except for one of the 5 SR signals, which had 4.8 seconds length. The second clinical database consisted of EGM only from VF, specifically, up to 240 VF episodes in 99 patients, for which all the available time recorded for each EGM signal was used. This

set of recordings aimed to check whether failures of the automated algorithm used for estimating f_{d_DFA} in DFA and OA to estimate the CL could have an impact on a larger set of measurements, and to check whether FOA, using f_0, could give high quality measurements in those same conditions.

Each EGM in both clinical databases was analyzed following the same methodology used in the preceding section, both for conventional analysis given by DFA and OA, and for the proposed FOA method. The averaged $1/CL$ in the time domain was also obtained for each EGM given by manual annotation by an expert, which allowed us to establish a gold standard for comparison with periodicity estimations from the classical and the proposed method.

2.5.2   Results on Database with Different Rhythms

Table 2.2 contains the averaged $1/CL$ from manual annotation for each EGM in the database with different rhythms, and the measured spectral parameters when computed with both DFA and FOA approaches (mean $\pm$ standard deviation for all of them). There was a high agreement between $1/CL$ and f_0 computed using FOA method for all rhythms, both in monopolar an bipolar recordings, indicating that FOA method is more suitable in the estimation of the main rhythm, whereas f_{d_DFA} computed using DFA and f_d showed only good agreement in VF recordings. Moreover, as shown in Figure 2.5, the proposed FOA was more accurate than DFA when estimating the averaged $1/CL$ for every single VF episode.

There was also visible discrepancy between f_{d_DFA} (DFA) and f_0 (FOA) in SR recordings. Given that DFA gave higher values of both in monopolar and bipolar than FOA. Another suggestion that FOA gave better estimates was the agreement between f_0 when computed in monopolar and in bipolar recordings. Also, f_0 computed by FOA allowed coherent comparisons between different rhythms. The slowest CL was for SR and the fastest was for VF, as trivially expected, whereas SVT and VT were very similar in terms of CL. Figure 2.4 shows the spline interpolated, normalized, and averaged spectral envelopes for the four rhythms. Bipolar recordings generally contained more power in high frequency components than monopolar recordings, and there was a crossing point in the spectral envelopes in SR, SVT, and VT, but not in VF. Table 2.2 also shows parameters oi and ri from OA, and parameters p_1 and p_e from FOA. Interpretation of the EGM organization has to be done with caution when using OA parameters, since they are based on f_{d_DFA} estimation and, as previously stated, the automatic estimation procedure in conventional DFA failed in several cases. According to oi, SR was more irregular than SVT, than VT, and also than VF when obtained from OA. FOA approach made it possible to establish a more coherent organization comparisons. According to p_1 in FOA, VF was the most irregular rhythm, as expected, whereas SVT was the most organized, even more than SR, which can be explained by the well known heart rate variability due to the autonomous system control of cardiac cycle in healthy conditions.
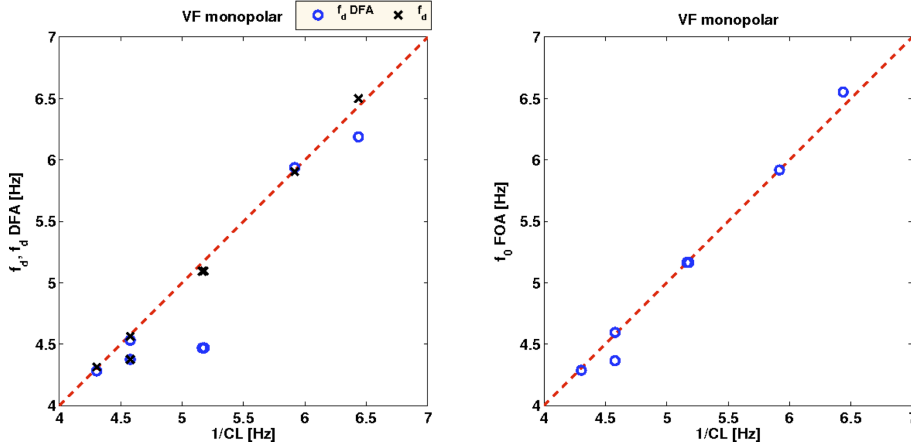
Figure 2.5: *Relationship between f_d, f_{d_DFA} from DFA and f_0 FOA, and $1/CL$ for every single one VF EGM in first database with different rhythms.*

2.5.3   Results on Database with Ventricular Fibrillation

Table 2.3 shows the spectral parameters measured by DFA and by FOA in the database with VF episodes. Periodicity, as characterized by f_0, was slightly different when estimated by DFA and by FOA. Further details can be seen in Figure 2.6, which shows f_{d_DFA} as estimated by DFA vs f_0 as estimated by FOA, allowing us to compare both estimations without the averaging effect in Table 2.3. Note that, though in general terms there was a high agreement between both estimations, however, in some cases the estimation of f_{d_DFA} and f_0 were dramatically different. Moreover, there was higher agreement between f_d and f_0 estimated by FOA than between f_d and f_{d_DFA}. This result is consistent with previous results in simulated signals and first database of real signals, showing that for non-harmonic structure, e.g. VF recordings, f_0 estimated by FOA is related to f_d. The differences between f_{d_DFA} f_0, and between f_d and f_{d_DFA} were significant (paired t-test, $p < 0.0\bar{5}$); whereas the differences in f_0 by FOA and f_d were non-significant, both in monopolar and bipolar recordings. Therefore, FOA yields better estimations of f_0 than the automatic procedure in DFA for VF recordings stored in ICD.

Organization parameters, namely oi and ri in OA, and p_1 and p_e in FOA, showed again and consistently that bipolar recordings are in general less organized than monopolar recordings.

2.6   Discussion and Conclusions

A new algorithm has been presented as a generalization of conventional DFA and OA, so-called FOA, which allows us to obtain automatically the spectral structure and features in EGM recordings. Controlled electrophysiological substrates have been simulated, and synthetic EGM have been obtained. A
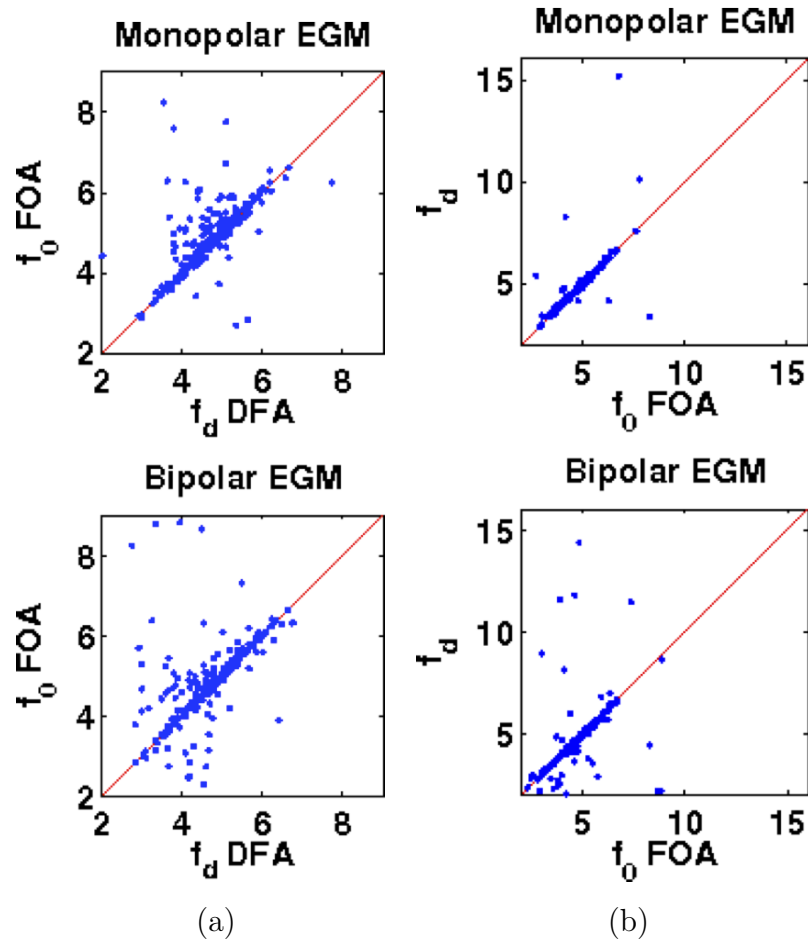
Figure 2.6: *Estimation of f_{d_DFA} by DFA (a) and f_d (b) vs f_0 estimated by FOA for each EGM recording in VF Database. The red line represents the $y = x$ line, points in this line representing both methods yielding the same estimated frequency.*

small database with four different rhythms, and a extensive VF database, have also been analyzed. The database with different rhythms aimed to evaluate the performance of the two different approaches, the classical DFA and the proposed FOA, in real EGM recordings with different electrophysiological and well-known situations. On the other hand, VF database aimed to evaluated the performance of both approaches in a real database with a large number of EGM recording. This was necessary to determine that the failures associated with the algorithm used in conventional DFA for estimating f_0, had some visible impact on the estimated regularity in a populational analysis. It also showed that the use of FOA alleviated the impact of these failures. This methodology allowed us to give a principled understanding of the meaning and limitations of the different indices currently used in the DFA and OA literature, and also to check the improvement given by the FOA spectral description.

Fundamental and Dominant Frequency. Due to a number of factors, f_0 and f_d can be different, and in that case, the use of f_d as a surrogate for

the CL is not guaranteed. This is because it might be just a harmonic of f_0. It is clearly shown in our results, suggesting that a distinction between f_d and f_0 should be maintained, in order to avoid errors in the determination of the EGM approximate CL. The virtually universal use of f_d in the electrophysiology literature should not lead to the erroneous concept that f_d always corresponds to the CL of the EGM. When harmonic structure is present, the inter-harmonic separation can confirm the estimated CL.

A usual procedure in DFA consists of estimating f_d from an auxiliary signal, obtained by filtering and rectification of the original EGM [23, 25, 26, 31]. In these references, this auxiliary signal was used to calculate f_{d_DFA} in the bipolar EGM, either for calculating the CL or as complementary information for the calculation of the oi. If the calculations have been successful, f_d in the auxiliary signal will correspond to f_0 in the original EGM. However, this will not be always the case, and sometimes an error in this automatic algorithm will yield incorrect CL estimations. In [31], an example is presented (Fig. 5-B in the reference) of an irregular EGM in which DFA gives a 10 Hz peak. In this case, the comparison to the activation interval pointed out by the authors, together with the evident presence of harmonic structure, indicates that the periodicity was given by f_0 at the 5 Hz peak, and that f_d was just its second harmonic. In a study examining the effect of changes in atrial EGM during AF on the f_d [1], good agreement was in general obtained between the (inverse of the) averaged CL and the f_d, except for varying amplitude and activation interval conditions (Fig. 3-D in the reference). Problems in the estimation of the CL therein can be explained by the automatic algorithm failing to extract the peak from the auxiliary signal, and they are similar to the ones observed in our experiments with VF recordings (Section 2.5).

The procedure presented here to estimate f_0 using FOA gave better results than the classical DFA procedure due to the fact that FOA is implicitly based on the harmonic structure presented in the signal to model it. FOA also accounts for fluctuations in the harmonic components, and the inter-harmonic spacing of the spectral peaks can give relevant information about the averaged CL of an EGM. The estimated CL in the spectral domain could also be cross-checked with the time-domain estimated in case of doubts. However, cross-checking with time-peaks counting can introduce some subjectivity or doubts, whereas MSE minimization is an objective and quantitative criterion. In fibrillatory recordings, FOA also performs well, because the LS projection gives a relevant weight only to the f_0 component, which in this case corresponds to f_d.

It should be noted that when a nonharmonic spectral structure is present, the f_0 parameter estimated with FOA can be similar to the f_d parameter, which will be a common situation in VF. Still, aiming to give an automated procedure, it was decided to always look for f_0 parameter in the EGM to capture the periodicity of the main rhythm. Taking into account the results of Table 2.2 (VF column), even in those cases of VF with one main narrow component and widespread activity, f_0 is often coincident with f_d, and both

parameters keep a marked coherence with $1/CL$ as marked by an expert. Hence, for the algorithm giving a unified solution, it can be consider that in those cases with one single narrow main component, that is harmonic structure with one single harmonic. This unification in the result of the algorithm for periodicity estimation, clearly has to be complemented with a parameter for regularity characterization.

Acquisition in Bipolar and Monopolar Recordings. Because the spectral envelope is simultaneously determined by the underlying physiological process and by the characteristics of the acquisition system, its quantification, either in terms of the power of the harmonics or by a more detailed and sophisticated technique, can yield a more detailed spectral description of the EGM under study. In general, f_d and f_0 are more likely to be coincident in monopolar than in bipolar recordings. The monopolar EGM can be said to have a mostly low-pass (band-pass) spectral envelope. Optical mapping recordings during AF and VF have usually a low-pass spectral envelope [24, 67], and hence, f_0 and f_d were usually the same in these recordings, which avoided the need of using the auxiliary signal processing. However, monopolar and bipolar atrial EGM during AF will have low-pass and band-pass envelopes, respectively, and comparisons between spectral parameters obtained from different systems can be problematic, given that small differences in the acquisition system (such as inter-electrode spacing or electrode size) could produce significant differences in the spectral envelope.

Organization and Harmonics. In the presence of harmonic structure, an appropriate signal model of organization should take the harmonics into consideration. Given that ri parameter was initially defined for optical mapping recordings, it could have some interpretation problems when straightforwardly applied to EGM during AF. This is due to the presence of harmonics. In this case, a redefinition of organization according to the spectral characteristics of the analyzed EGM is convenient. This is done in [25] where the authors defined oi. A theoretical study on OA for bipolar EGM [68] showed that the calculation of ri could be affected by harmonics, and concluded that the ri is not a valid measure for organization. The conclusion might have changed if the harmonic structure of the bipolar EGM had been considered. FOA in our simulation and real data studies shows that regularity measurements have to account for the harmonics in its definition. Otherwise, misleading low values of organization can be obtained from organized EGM recordings. The use of oi is more robust in this sense than ri, but still it can be affected by poor previous estimation of the periodicity parameter.

Additional Considerations. One possible improvement for the method proposed is to look for Δ in a narrow frequency interval around the harmonic peaks, in order to capture more wide-band behaviors. However, the usefulness of this modification was not significant in our database (not shown). Arrhythmia discrimination capabilities of the parameters was also analyzed, keeping in mind the limited size of the first data set. In this setting, parameters from the FOA approach, f_0 and p_1, were the only ones that seemed to offer a coherent trend for rhythm classification. Further the effect of

the recording length in the second database was analyze, and it was found that the averaged differences between a fixed length for all the recordings (6 seconds) and the actual length of the episode being considered were not relevant. However, in some few cases some problems could arise when using a different frequency grid for the same EGM, which is an effect to be taken into account in the algorithm.

Limitations of the Study. The mathematical model that has been used in the present study is approximated and highly simplified. The simulation of complex electrophysiological conditions could lead to inaccurate morphology for the extracellular signals, since in complex conditions, the amplitude and morphology of the action potentials may be highly variable. The use of computer models based on differential equations would be more appropriate when simulating and analyzing a wider variety of VF mechanisms. Accordingly, extrapolation of the results to the clinical environment should be made cautiously. Results on ICD recordings were significant, but their extrapolation to electrical and optical mapping recordings should be specifically addressed. FOA algorithm can be used for analyzing atrial fibrillation EGM, which is an interesting research direction. Also of interest is the consideration of several periodic components in the signal under analysis. These two relevant issues are beyond the scope of this paper.

Conclusions. DFA and OA of EGM have been used in cardiac electrophysiology for characterizing almost-periodic activation and high regularity regions, respectively. The rationale under the mathematical definition of these indices has not always been fully considered, thus leading to interpretation problems. Our results show that the proposed FOA yields a more compact and reliable organization description of cardiac EGM than DFA and OA alone in ICD stored EGM signals.

		Sinus Rhythm		Supraventricular Tachycardia		Ventricular Tachycardia		Ventricular Fibrillation	
		Monopolar	Bipolar	Monopolar	Bipolar	Monopolar	Bipolar	Monopolar	Bipolar
Time	CL^{-1} (Hz)	1.21 ± 0.11	1.21 ± 0.11	2.58 ± 0.15	2.58 ± 0.16	2.72 ± 0.47	2.71 ± 0.47	5.16 ± 0.78	5.20 ± 0.84
DFA and OA	f_0 (Hz)	2.94 ± 0.76	3.66 ± 0.33	2.58 ± 0.16	3.51 ± 1.2	3.25 ± 0.67	3.25 ± 0.66	5.10 ± 0.87	5.25 ± 0.82
	f_d (Hz)	3.94 ± 0.90	4.03 ± 2.67	6.62 ± 3.78	9.36 ± 11.68	5.36 ± 2.58	5.34 ± 4.62	5.24 ± 0.87	5.26 ± 0.85
	ri	0.15 ± 0.01	0.21 ± 0.25	0.26 ± 0.11	0.15 ± 0.04	0.35 ± 0.19	0.51 ± 0.70	0.71 ± 0.09	0.49 ± 0.11
	oi	0.47 ± 0.04	0.48 ± 0.19	0.92 ± 0.02	0.64 ± 0.02	0.84 ± 0.21	0.81 ± 0.28	0.81 ± 0.06	0.74 ± 0.08
FOA	f_0 (Hz)	1.22 ± 0.11	1.22 ± 0.11	2.58 ± 0.16	2.58 ± 0.16	2.74 ± 0.46	2.70 ± 0.52	5.26 ± 0.89	5.27 ± 0.87
	p_1	0.82 ± 0.12	0.68 ± 0.13	0.91 ± 0.08	0.70 ± 0.23	0.74 ± 0.21	0.64 ± 0.27	0.66 ± 0.15	0.51 ± 0.09
	p_e	0.18 ± 0.12	0.32 ± 0.13	0.09 ± 0.08	0.30 ± 0.23	0.26 ± 0.21	0.36 ± 0.27	0.34 ± 0.15	0.49 ± 0.09

Table 2.2: *Results of DFA, OA, and FOA, in clinical EGM signals from the different rhythms database.*

	DFA		FOA	
	Monopolar	Bipolar	Monopolar	Bipolar
f_{d_DFA} (Hz)	4.68 ± 0.73	4.67 ± 0.84	—	—
f_0 (HZ)	—	—	4.85 ± 0.82	4.85 ± 1.00
p_1	—	—	0.50 ± 0.20	0.37 ± 0.20
p_e	—	—	0.50 ± 0.21	0.63 ± 0.20
f_d (Hz)	4.90 ± 1.07	4.90 ± 1.71	—	—
ri (OA)	0.56 ± 0.18	0.37 ± 0.18	—	—
oi (OA)	0.73 ± 0.16	0.62 ± 0.15	—	—

Table 2.3: *Results of DFA, OA, and FOA, in clinical EGM signals from VF Database.*

Chapter 3

Atrial Fibrillation Characterization using Correntropy and Fourier Organization Analysis

3.1 Introduction

AF is nowadays the most usual sustained arrhythmia. Catheter ablation is a useful method to prevent recurrences in patients with paroxysmal or persistent AF, and recently, analysis of intra–cardiac EGMs has been used as a criterion for selecting efficient ablation targets [51, 69]. Two main approaches have been used to guide the ablation procedure to date, namely, time domain [70] and frequency domain methods [2], the former based on activation rate, and the latter based on f_d representing the inverse average CL. Both methods aim to estimate the EGM periodicity properties with the objective of finding those regions with the shortest average CL. A usual technique used to perform the frequency domain analysis of AF EGMs is the so-called DFA [3, 31], which aims to estimate the average excitation rate (inverse of mean CL) based on the f_d of a preprocessed AF signal. However, such descriptions have often discarded relevant information of the spectrum, e.g., the harmonic structure or the spectral envelope. Additionally, it is not guaranteed that f_d will always provide a good estimation of the averaged CL, given that there are several controversial studies about these issues [58, 71]. More, it has been pointed out that DFA may not give a correct description when dealing with complex fractionated AF EGMs [72, 73].

A new method to estimate the f_0 of AF signals is proposed, instead of f_d, in order to characterize the activation rates, hence giving a quality estimation of the average CLs. The reason for this is that in purely sinusoidal signals, the f_0 is the frequency at which the maximum of the power spectral density (PSD) occurs. Nevertheless, if the signal has harmonic structure, which is very common in regular AF signals, it could happen that an harmonic, and not the fundamental, would correspond to the value which gives

the maximum of the PSD. Since the harmonic magnitude distribution depends, among other parameters, on the morphology of the waveform that is repeated, it is more likely that signals with a bandpass character show the maximum of the PSD (f_d) in an harmonic component.

The method proposed here is based on a generalization of the correlation function for stochastic processes, called *Correntropy* [74]. This method proposes a similarity measurement defined in terms of inner products in a kernel parameter space. The Correntropy function has been applied successfully in previous medical research [75]. To deal with complex fractionated AF EGMs, a combination of Correntropy function with FOA is proposed.

3.2   Methods

In this Section, the Correntropy is defined. DFA and FOA methods, to characterize the periodicity of AF signals, were defined in Chapter 2.

3.2.1   Correntropy Definition

It is assumed that $\{x(n), n = 0, \cdots, N-1\}$ is a discrete stochastic process of length N. The *Correntropy* function, denoted $V(\tau)$, is defined as [74, 76, 77]:

$$V(\tau) = \mathbf{E}\left[\kappa_\sigma\left(x(n) - x(n - \tau)\right)\right] \tag{3.1}$$

where $\mathbf{E}$ is the statistical expectation operator and κ_σ is a symmetric positive definite kernel. The kernel used in this study is the Gaussian kernel, which is one of the most commonly used in different areas, such as machine learning, support vector machines, or density estimation [78]:

$$\kappa_\sigma(x(n), x(n - \tau)) = \frac{1}{\sigma\sqrt{2\pi}} \exp\left[-\frac{(x(n) - x(n - \tau))^2}{2\sigma^2}\right] \tag{3.2}$$

where σ is the kernel width parameter, or kernel size.

The Correntropy function partially characterizes higher order moments of a stochastic process. This property is clearly shown expanding the Correntropy function using Taylor series:

$$V(\tau) = \frac{1}{\sigma\sqrt{2\pi}} \sum_{k=0}^{\infty} \frac{(-1)^k}{2\sigma^{2k}k!} \mathbf{E}\left[(x(n) - x(n - \tau))^{2k}\right] \tag{3.3}$$

therefore, $V(\tau)$ contains all even-order moments of $x(n)$. The emphasis given to the higher order moments is controlled by kernel width σ. In this study, unless otherwise stated, the value assigned to σ is determined by Silverman's rule of density estimation [74], as follows:

$$\sigma = 0.9AN^{-0.2} \tag{3.4}$$

where A is the smallest value between standard deviation of data samples and data interquartile range scaled by 1.34, and N is the number of data samples. Although this rule is for probability density estimation, it is simple and provides reasonable results.
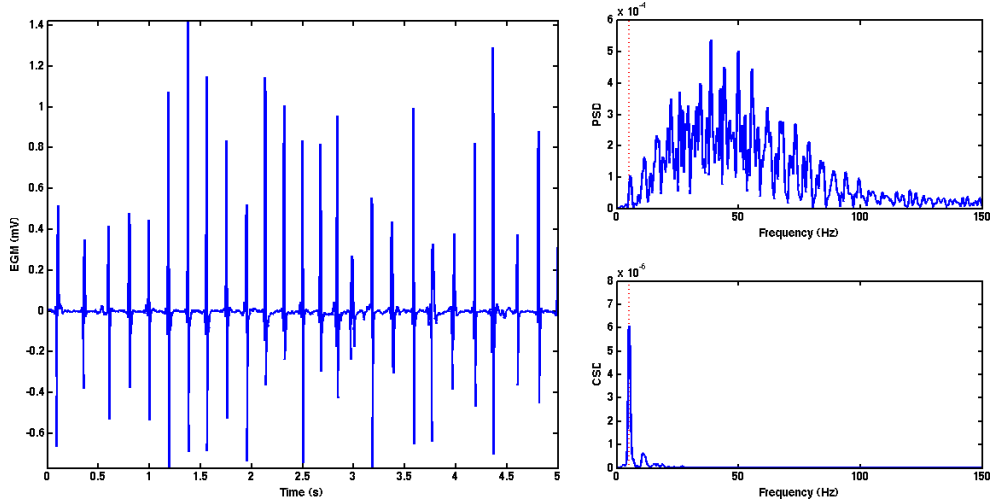
Figure 3.1: *Real AF signal (left, note that time is in vertical axis), and its PSD signal (right-top) and CSD signal without preprocessing (right-bottom). The f_0 is marked in dotted line.*

3.2.2 Fundamental Frequency Estimation

PSD based on the Correntropy function, denoted as Correntropy Spectral Density (CSD), is used to estimate the fundamental frequency in AF signals:

$$P_x(f) = \sum_{m=-(N-1)}^{N-1} V(m)e^{-j2\pi fm} \tag{3.5}$$

The procedure to estimate f_0 with Correntropy is the following:

- Preprocess the AF signal, $x(n)$: bandpass filtering at 40-250 Hz, rectification, and lowpass filtering at 20 Hz.

- Estimate the CSD using Welch's method.

- Identify peaks in CSD higher than a threshold.

- Estimate f_0 as the argument of the first identified peak in CSD.

The usual preprocessing method, according to the algorithm proposed in [3], can be summarized as follows [23]:

- Bandpass filtering at 40-250 Hz.

- Rectification.

- Lowpass filtering at 20 Hz.

- Windowing (Hanning).

This preprocessing method is the same used in DFA method. f_{d_DFA} is estimated by using the preprocessed AF signal.

The preprocessing stage aims to modify the band-pass nature of the AF signal, mainly in bipolar EGMs, in order to emphasize the spectral components near the fundamental frequency and to attenuate the spectral components due to the harmonics. This step facilitates the f_0 estimation. A second goal is to obtain reliable FOA models, which are more feasible when the signal has a limited bandwidth and a low-pass nature.

Some AF signals show a complex time structure. One of the possible causes of this complexity may be the interaction of two fibrillatory wavefronts, known as type II AF signals [79]. The strategy proposed in this paper to characterize this type of signals is to estimate two different fundamental frequencies, $f_{0,1}$ and $f_{0,2}$, assuming that there is only two wavefronts, showing there is an improvement in the FOA model constructed using both fundamental frequencies. The steps are listed below:

- Estimate $f_{0,1}$ with the previous procedure.

- Fine search for $f_{0,1}$ using a FOA model approach, minimizing p_e^1, and fit a FOA model $foa_1(n)$.

- Remove $foa_1(n)$ from the original signal $x(n)$ (or preprocessing versions); $y(n) = x(n) - foa_1(n)$.

- Estimate $f_{0,2}$, with the previous procedure, using $y(n)$ as input signal.

- Fit a FOA model, $foa_{12}(n)$ with the two estimated fundamental frequencies, $f_{0,1}$ and $f_{0,2}$, and compare the parameter p_e^{12} from this model with p_e^1, from the model using only $f_{0,1}$, to evaluate the improvement.

Figure 3.1 shows a real AF EGM and both the PSD of the original signal and the CSD of the Correntropy function. It can be seen that AF signal has a band-pass nature. Figure 3.2 shows the CSD computed in an AF signal without and with preprocessing. In AF signals with a clear harmonic structure and a very regular period, the Correntropy function would lead to similar results with and without preprocessing. Anyhow, the preprocessing would allow to obtain more reliable FOA models, and hence it would improve the estimation of f_0 in less regular and noisy signals.

3.3   Pseudo–Real Experiments

In order to test the performance of the Correntropy–FOA approach when estimating the f_0 in AF signals, a set of experiments using a pseudo-real AF signal with known f_0 was designed. The model used to generate the pseudo-real signal was based on the formerly proposed in [68]. Basically, the AF synthetic signal is built by replicating a template waveform in a periodic way, allowing to introduce some irregularity both in amplitude and in periodicity cycle from one beat to another. This model was modified by changing the
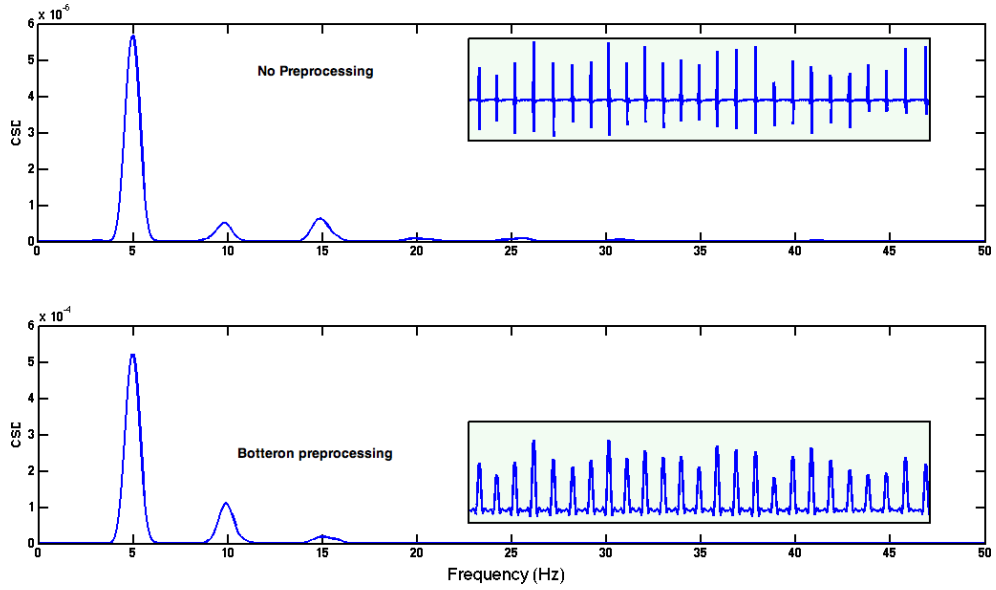
Figure 3.2: *Real AF signal (inside plots) and its corresponding CSD signal for different preprocessing methods.*

synthetic template waveform for a real beat extracted from an AF bipolar signal. Three different experiments were designed:

- Pseudo-real AF for estimation of the f_0 under noise conditions. AF signals with different f_0, ranging from 3 to 10 Hz in 0.5 Hz steps, and contaminated with white Gaussian noise for 2 signal to noise ratios (SNR) 0 dB, and 5 dB, were simulated. For each f_0, and for each SNR, 100 realizations were generated.

- Pseudo-real AF signals plus random cycle uncertainty for evaluation of robustness. AF signals, with a f_0 of 12 Hz, plus a uniformly distributed random cycle uncertainty varying from 5 to 20 ms, were simulated in steps of 5 ms. For each value of the uncertainty, 100 realizations were performed.

- Pseudo-real AF signals with two wavefronts. AF signals resulting from the composition (sum) of two signals with different fundamental frequency, $f_{0,1}$ and $f_{0,2}$, were simulated. The first component $f_{0,1}$ was previously fixed by hand, whereas the second component was randomly selected in the usual range between 3 and 15 Hz. Table 3.1 shows the pairs of values used in this experiment.

3.4   Experiments with Real Signals

A set of 17 5-seconds AF bipolar EGMs during EPS were collected. All EPS were conducted in the arrhythmia unit at Hospital Universitario Virgen de Arrixaca, Murcia, Spain. EGM signals were recorded in a polygraph

$f_{0,1}$ Hz	$f_{0,2}$ Hz
5.0	12.9; 8.5; 6.3
10.0	13.4; 6.3; 8.2
12.0	4.7 ; 5.1; 14.5

Table 3.1: *Experiment with pseudo-real AF signals with two components and two fundamental frequencies. $f_{0,1}$ was prefixed by hand, and $f_{0,2}$ was randomly selected between 3 and 15 Hz.*

Cardiolab by GE Medical Systems Information Technology, using the bipolar signals obtained from a decapolar catheter placed in the coronary sinus and a duodecapolar catheter placed in the right atrium around the tricuspid annulus. The signals were recorded at 977 Hz sampling frequency.

The AF EGMs were visually selected by a cardiologist and separated into two different groups: one group with very regular (periodic) and uniform morphology signal, and another group with complex and fragmented signals. The first group, called Type-I, contained 8 recordings, and the second group, called Type-II, contained 9 recordings.

The Type-I group was studied to evaluate the behaviour of the proposed Correntropy method to characterize organized signals, where the mean CL can be readily calculated manually in the time domain, and therefore a comparison with a gold standard can be achieved. For this group, an automatic method to compute the CL was implemented and manually supervised when necessary. The mean CL computed by the previous procedure was compared with the f_0 estimated with Correntropy on a preprocessed signal, and with f_{d_DFA} estimated using DFA. The Type-II group was selected to study the performance of the proposed Correntropy method to characterize complex AF signals, with two or more wavefronts interacting. Therefore, it could be necessary more than only one f_0 for complete characterization. For this group, a comparison with a semi-automatic CL calculation would introduce a bias, due to the difficulty to identify the fiducial points, mainly because of the high irregularity in period and also the complexity in morphology. For this experiment, $f_{0,1}$ and $f_{0,2}$ were estimated by using the proposed Correntropy-FOA method. Also, the parameter p_e^1 from the FOA model when using only the first component, and $p_e^{1,2}$ from FOA model by using both components simultaneously were used to evaluate the improvement when using more than one f_0. Also, f_{d_DFA} obtained using DFA was also reported.

f_0	SNR = 0 dB		SNR = 5 dB	
	$\hat{f}_{d\_DFA}$ **DFA**	$\hat{f}_0$ **Corrent**	$\hat{f}_{d\_DFA}$ **DFA**	$\hat{f}_0$ **Corrent**
3	3.78($\pm$1.46)	3.65($\pm$1.25)	3.20($\pm$0.72)	3.42($\pm$1.10)
4	4.40($\pm$1.21)	4.00($\pm$0.02)	4.00($\pm$0.00)	4.00($\pm$0.00)
5	5.20($\pm$1.00)	5.00($\pm$0.02)	5.00($\pm$0.00)	5.00($\pm$0.00)
6	6.00($\pm$0.00)	6.00($\pm$0.00)	6.00($\pm$0.00)	6.00($\pm$0.00)
7	7.00($\pm$0.00)	7.00($\pm$0.00)	7.00($\pm$0.00)	7.00($\pm$0.00)
8	8.00($\pm$0.00)	8.00($\pm$0.00)	8.00($\pm$0.00)	8.00($\pm$0.00)
9	9.00($\pm$0.00)	9.00($\pm$0.00)	9.00($\pm$0.00)	9.00($\pm$0.00)
10	10.00($\pm$0.00)	10.00($\pm$0.00)	10.00($\pm$0.00)	10.00($\pm$0.00)

Table 3.2: *Experiment with pseudo-real AF signals with additive Gaussian white noise. Comparison between real f_0 and estimated $\hat{f}_0$ using Correntropy and f_{d_DFA} using DFA (mean $\pm$ standard deviation). Units are Hz.*

3.5 Results on Pseudo-real Signals

3.5.1 Pseudo-real Atrial Fibrillation Signals with Additive Noise

In this experiment, $\hat{f}_0$ estimated using the Correntropy method and f_{d_DFA} by DFA were compared to the real f_0 in pseudo-real AF signals with Gaussian noise. Table 3.2 shows the results as mean$\pm$standard deviation for two different SNR. Both methods provided good-quality results, with the Correntropy approach yielding lower standard deviation.

3.5.2 Pseudo-real Atrial Fibrillation Plus Cycle Random Uncertainty

Table 3.3 shows the results when analysing the pseudo-real AF with cycle random uncertainty. Original signal (without uncertainty) had $f_0 = 12$ Hz. The results showed that both methods (Correntropy and DFA) were robust when estimating the periodicity in conditions where signals are not purely periodic, with slightly lower standard deviation for the DFA method.

3.5.3 Pseudo-real Atrial Fibrillation Signals with Two Wavefronts

This experiment aimed to emulate complex signals where the AF signals correspond to an interaction between two wavefronts with different fundamental frequencies. This is a deterministic experiment, without stochastic part, in order to evaluate the feasibility of the proposed Correntropy-FOA method to deal with two components in controlled conditions.

Uncertainty	$\hat{f}_{d\_DFA}$ **DFA**	$\hat{f}_0$ **Correntropy**
ms	Hz	Hz
5	12.00($\pm$0.00)	12.00($\pm$0.00)
10	12.00($\pm$0.00)	12.00($\pm$0.00)
15	12.00($\pm$0.00)	12.00($\pm$0.01)
20	12.00($\pm$0.02)	12.00($\pm$0.04)

Table 3.3: *Experiment with pseudo-real AF signals with random uncertainty in cycle with a real fundamental frequency of 12 Hz (mean $\pm$ standard deviation). Correntropy method using preprocessing.*

$[f_0^1, f_0^2]$	Correntropy-FOA $[\hat{f}_{0,1}, \hat{f}_{0,2}]$
[5.0, 12.9]	[5.0, 12.9]
[5.0, 8.5]	[5.0, 8.5]
[5.0, 6.3]	[4.9, 6.3]
[10.0, 13.4]	[10.0, 13.4]
[10.0, 6.3]	[10.0, 6.3]
[10.0, 8.2]	[10.0, 8.2]
[12.0, 4.7]	[12.0, 5.0]
[12.0, 5.1]	[12.0, 5.1]
[12.0, 14.5]	[12.0, 14.5]

Table 3.4: *Experiment with pseudo-real AF signals using two fundamental frequencies. Correntropy-FOA method using preprocessing. Units are in Hz*
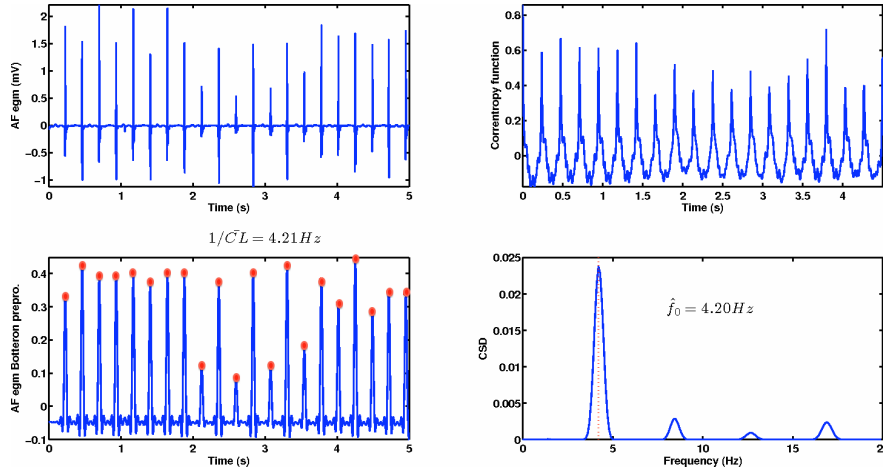
Figure 3.3: *Analysis of a real AF signal (top-left). The periodicity of the signal was estimated in the time domain by computing the average CL (bottom-left), and the $\hat{f}_0$ using Correntropy (top-bottom-right).*
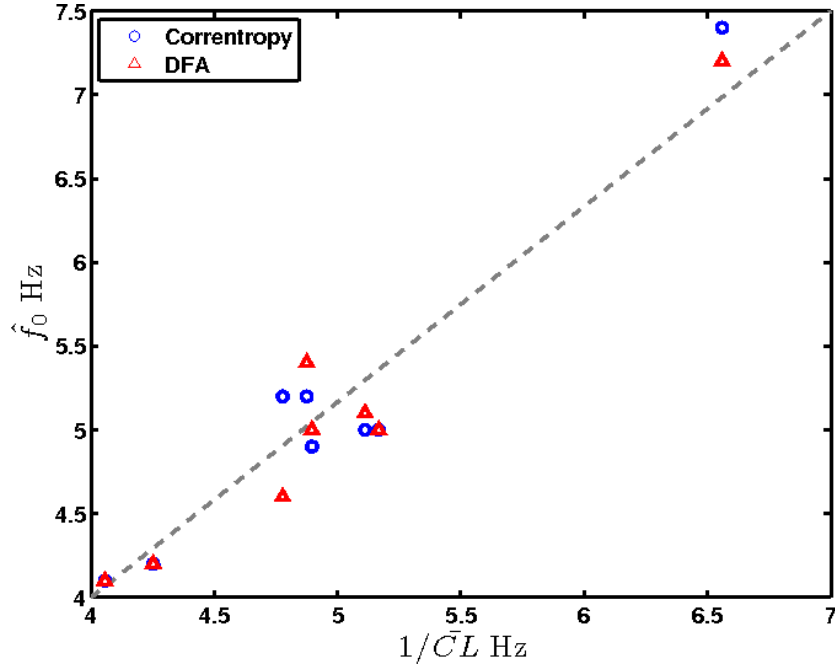
Figure 3.4: *Comparison between periodicity estimated in time domain (CL), and estimated using Correntropy and DFA.*

Table 3.4 shows the original values of the two pseudo-real components forming the complex AF electrogram, and the estimated fundamental frequencies when using the proposed method. It can be checked that in these simple conditions, without noise, the method was able to extract both components precisely.

3.6   Results on Real Signals

3.6.1   Type-I Atrial Fibrillation Signals

In order to evaluate the performance of Correntropy method in periodic and simple morphology AF signals, the inverse of the average CL was compared with $\hat{f}_0$ when estimated with Correntropy method, and $\hat{f}_d$ using DFA. The CL was computed using a semi-automatic algorithm, which basically detects the activation peaks in the preprocessed signal. This result was visually inspected to avoid false detections. Figure 3.3 shows an example of both estimation of CL and $\hat{f}_0$ using the Correntropy method.

The results for the 8 recordings are summarized in Figure 3.4, representing a comparison between the inverse average CL and $\hat{f}_0$ using Correntropy method and $\hat{f}_d$ using DFA. This analysis shows that both methods performed in a similar way, with high matching with the time domain estimation.

Recording	$\hat{f}_{0,1}$	$\hat{f}_{0,2}$	p_e^1	$p_e^{1,2}$	f_{d_DFA}
Recording 1	**7.53**	**7.30**	**0.46**	**0.36**	7.60
Recording 2	7.06	14.60	0.48	0.45	7.30
Recording 3	**7.41**	**7.50**	**0.55**	**0.45**	7.5
Recording 4	**6.57**	**6.80**	**0.62**	**0.52**	12.80†
Recording 5	4.80	3.30	0.40	0.32	4.80
Recording 6	**5.43**	**5.10**	**0.57**	**0.34**	5.20
Recording 7	4.00	4.00	0.22	0.17	4.00
Recording 8	10.38	11.20	0.63	0.59	10.30
Recording 9	9.69	10.20	0.86	0.80	9.50

Table 3.5: *Analysis of real AF signal from Type-II dataset. $\hat{f}_{0,1}$, $\hat{f}_{0,2}$ and p_e^1, $p_e^{1,2}$ from Correntropy-FOA was computed for each recording. Reduction from p_e^1 to $p_e^{1,2}$ in more than 0.1 units.*

3.6.2   Type-II Atrial Fibrillation Signals

This set of signals was selected to study how well, the proposed Correntropy-FOA method, characterizes complex signals, under the assumption that their complex nature may be due to the interaction of different wavefronts at different activation rates (CL). The proposed method estimated two fundamental frequencies and assessed their adequacy modelling the signal. If the residual energy was reduced by more than 0.1 units using a second component in the model, that is using $f_{0,2}$, then it was assumed that there was more than one wavefront interacting.

Table 3.5 shows the results of the Correntropy-FOA method applied on the Type-II dataset. The analysis using DFA was also reported. Note that there was one value (marked by †) where $\hat{f}_{d\_DFA}$ was estimating nearly the second harmonic ($2 \times f_0$). This error can arise when DFA is applied to some complex signals [31]. The analysis suggested that at least 4 out of the 9 recordings were better characterized using two different components. High values of p_e suggested that more than two components would be needed for a more complete characterization.

Figure 3.5 shows how a complex AF signal is well modelled using two different components.

3.7   Conclusions

A new method based on the Correntropy function was proposed to estimate the f_0 of AF signals to assess its periodicity. A combination of this method with the FOA approach to model fibrillatory signals was proposed to analyze complex AF signals, under the assumption that the complexity may
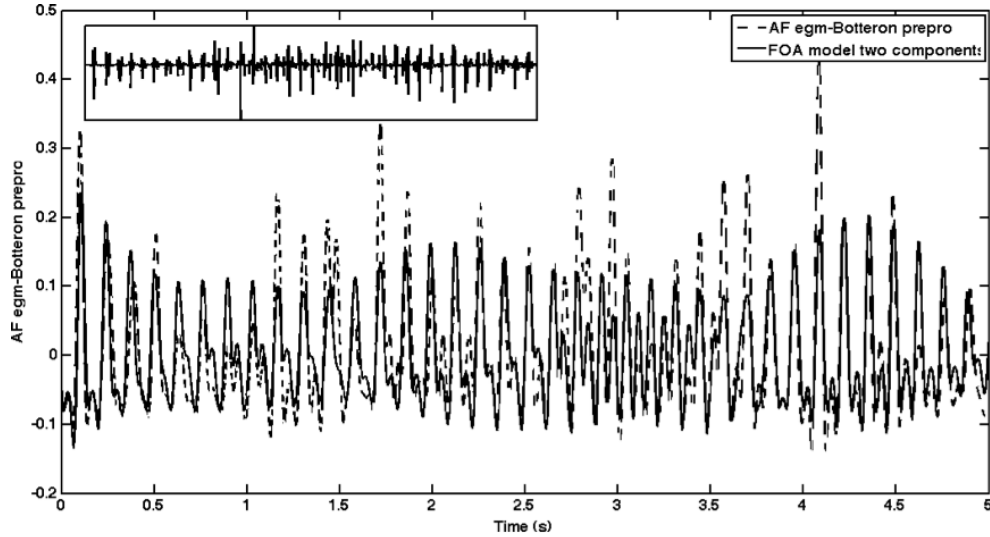
Figure 3.5: *An example of a complex AF, which is best modelled using two different fundamental frequencies. The original AF signal is plotted in the interior panel.*

be originated by the interaction of two (or more) wavefronts with different f_0. Both methods were compared with the classic approach based on DFA, which characterized the periodicity of the AF signal by means of the f_d calculated on a preprocessed signal. A set of experiments with pseudo-real AF signals were designed. In addition, two different dataset were assembled, one with regular and homogeneous AF signals, and another one with complex AF signals. The proposed method allowed, on one hand, to characterize the periodicity of regular AF signals, and on the other hand, to improve the characterization of more complex ones. In the future, a more comprehensive analysis with larger real datasets must be done to assess the adequacy of these promising methods characterizing AF signals. From the technical point of view, a more robust technique to identify the statistical relevance of using more than one component in FOA model has to be devised, what could allow also to identify more than two components to give a complete characterization. Different spectral resolutions Δ must be tested to ensure that the model is capable of correctly handling irregularity in the periodicity.

Part III

Signal Processing Methods to Study Baroreflex and Autonomic Nervous System

Chapter 4

Spectrally Adapted Mercer Kernels for Support Vector Nonuniform Interpolation of Heart Rate Variability

4.1 Introduction

Shannon's work on uniform sampling [80, 81] states that a noise-free, band-limited, uniformly sampled continuous-time signal can be perfectly recovered whenever the sampling rate is larger or equal than twice the signal bandwidth. These initial results have been extended both in theoretical studies [82, 83, 84, 85] and in practical applications [86, 87, 88]. However, the interpolation problem when these assumptions are not met becomes a very hard one, and many approaches have been proposed by extending Shannon's original idea.

A seminal work in this setting was Yen's algorithm [89]. In that work an expression for the uniquely defined interpolator of a nonuniformly sampled bandlimited signal is computed by minimizing the energy of the reconstructed signal. The solution is given as the weighted sum of *sinc* kernels with the same bandwidth as the signal. This algorithm suffers from ill posing due to the degrees of freedom of the solution [87]. This limitation is alleviated with the inclusion of a regularization term[90]. Other interpolation algorithms using the *sinc* kernel have been proposed [87, 91, 92], in which the *sinc* weights are obtained according to the minimization of the maximum error on the observed data. These algorithms, which use the *sinc* kernel as their basic interpolation function, implicitly assume a band-limited signal to be interpolated. For non band-limited signals, other algorithms have considered a non band-limited kernel, such as the Gaussian kernel [84]. Finally, very efficient methods have been recently developed to reduce the computational complexity of the interpolator, for example by using filter banks [93, 94], or a modified weighted version of the Lagrange interpolator [95] (see also references therein). It is interesting to note that the well-known Wiener filter has

received less attention than the use of Gaussian or *sinc* kernel expansions for nonuniform-sampled signal interpolation problems [96].

On a different theoretical framework, SVMs have been proposed in recent years as learning-from-samples tools for a number of problems, including classification and regression [97], and in many practical applications [98]. SVM algorithms have been recently proposed for nonuniform-sampled signal interpolation [99], using *sinc* and Gaussian kernels, and showing good performance for low-pass signals in terms of robustness, sparseness, and regularization capabilities. SVM algorithms have to be formulated in terms of Mercer kernels, and a well-known theoretical result is that any autocorrelation function is a valid Mercer kernel [100]. However, the suitability of using the autocorrelation of the observed process as the SVM kernel for interpolation problems has not been analyzed so far. Moreover, no previous analysis can be found on the SVM kernel choice which takes into account the spectral adaptation between the observed signal, the kernel itself, and the Lagrange multipliers yielded by the model.

HRV has been suggested as a noninvasive tool to assess the state of the ASN and its relationship with cardiovascular mortality [4]. RR-interval time series are used to study the HRV, and it is usually analyzed on 24-h ambulatory ECG recordings (Holter). Spectral analysis of HRV allows to identify the different oscillatory components involved in the HR control, and it is usually identified with the activity of the ANS branches (sympathetic and vagal) [4, 101]. However, Holter recordings suffer from high noise, which induces the presence of artifacts and beat misclassifications. Conventional spectral analysis is very sensitive to these problems in Holter recordings. Additionally, PSD is generally estimated from the RR-Interval time series, which is a representation of the beat-to-beat variability. Therefore, it is inherently a discrete and nonuniform time series (this is the reason for the *variability*). The usual procedure implies to interpolate and re-sample the RR-Interval time series in order to obtain a uniformly sampled time series and then apply PSD techniques. In this chapter, the use of SVM algorithms is proposed to solve the nonuniform sampling interpolation problem by exploring several Mercer kernels that are spectrally adapted to the signal to be interpolated. To accomplish this task, first the relationship between the Wiener filter and the SVM algorithm is analyzed for this problem, using the spectral interpretation of both algorithms. Then, according to this analysis, different SVM interpolation kernels are explored accounting for different degrees of spectral adaptation and performance, namely, band-pass kernels, estimated signal autocorrelation kernels, and actual signal autocorrelation kernels. This approach is tested on two different 24-hour Holter recording from a healthy and a Congestive Heart Failure subjects.

4.2   Algorithms for Nonuniform Interpolation

In this section, first notation and definition of the problem to solved are introduced. Second, three nonuniform interpolation algorithms, namely, Wiener filter [96], Yen regularized interpolator [89, 90], and SVM interpolator [99] are described. Although much more interpolation methods have already been proposed in the literature, the limitation to these three cases has two reasons: (i) they are representative cases of optimal algorithms (with a different optimality concept for each case), and (ii) they have a straightforward spectral interpretation, which allows an interesting comparison with the algorithms proposed.

Let $x(t)$ be a continuous-time signal with finite-energy, consisting of a possibly band-limited signal $z(t)$, which can be seen as a realization of a random process, corrupted with additive noise $w(t)$, i.e., $x(t) = z(t) + w(t)$, where the noise is modeled as a zero-mean Wide Sense Stationary (WSS) process. This signal has been observed on a set of N unevenly spaced time instants, $\{t_n, n = 1, \ldots, N\}$, obtaining the set of observations $\boldsymbol{x} = [x(t_1), \cdots, x(t_n), \cdots, x(t_N)]^T$.

Then, the nonuniform interpolation problem consists in finding a continuous-time signal $\hat{z}(t)$ that approximates the noise-free interpolated signal in a set of K time instants, $\{t'_k, k = 1, \ldots, K\}$.

4.2.1   Wiener Filter for Nonuniform Interpolation

Time Domain Analysis. As described in [96], a Bayesian approach to solve this problem amounts to the Wiener filter [102]. Assuming that $z(t)$ is zero mean, the linear estimator is given by:

$$\hat{z}(t'_k) = \boldsymbol{a}_k^T \boldsymbol{x} \qquad \text{for } k = 1, \ldots, K \tag{4.1}$$

The scalar Linear Minimum Mean Square Error (LMMSE) estimator is obtained when $\boldsymbol{a}_k$ is chosen to minimize the MSE and takes the following form [96]:

$$\hat{z}(t'_k) = \boldsymbol{r}_{z_k}^T \boldsymbol{C}_{xx}^{-1} \boldsymbol{x} \qquad \text{for } k = 1, \ldots, K \tag{4.2}$$

Vector $\boldsymbol{r}_{z_k}$ contains the cross covariance values between the observed signal and the signal interpolated at time t'_k, that is $\boldsymbol{r}_{z_k} = [r_{zz}(t'_k - t_1), \cdots, r_{zz}(t'_k - t_N)]^T$, where $r_{zz}(\tau)$ is the autocorrelation of the *noise-free* signal for a time shift τ. $\boldsymbol{C}_{xx}$ is the covariance matrix of the observations and, assuming WSS data with zero mean, it is computed as $\boldsymbol{C}_{xx} = \boldsymbol{R}_{zz} + \boldsymbol{R}_{ww}$, where $\boldsymbol{R}_{zz}$ is the autocovariance matrix of the signal with component i, j given by $\boldsymbol{R}_{zz}(i, j) = r_{zz}(t_i - t_j)$, and $\boldsymbol{R}_{ww}$ is the noise covariance matrix. For the *i.i.d.* case, $\boldsymbol{R}_{ww} = \sigma_w^2 \boldsymbol{I}_N$, with σ_w^2 the noise power and $\boldsymbol{I}_N$ the identity matrix of size $N \times N$. Thus, $\hat{z}(t'_k)$ is given by:

$$\hat{z}(t'_k) = \left[\left(\boldsymbol{R}_{zz} + \sigma_w^2 \boldsymbol{I}_N \right)^{-1} \boldsymbol{r}_{z_k} \right]^T \boldsymbol{x} \tag{4.3}$$

Although the solution in (4.3) is optimal in the MSE sense, two main drawbacks can arise when using it for practical applications: (1) it implies the inversion of a matrix that, specially for high SNR, can be almost singular, so the problem can become numerically ill-posed; and (2) the knowledge of the autocorrelation of the signal $r_{zz}(\tau)$ at every $\tau = t_i - t_j$ is needed, so it must estimated from the observed samples if it is not known.

Frequency Domain Analysis. The solution of the LMMSE estimator given by (4.2) can be seen as the convolution of the observations with a filter with impulse response $h_W^{(k)}[n] = a[k - n]$. For a finite number of nonuniform samples, the solution cannot be converted into a time-invariant filter since it depends on k index, which is a significant different with the uniform-sampling case. However, in order to provide a simple spectral interpretation of the interpolator it is assumed that $N \to \infty$ and then (4.3) can be approximated as the convolution of the observations with a time-invariant filter with response $h_W[n]$, which does not depend on the time index k [96]:

$$\hat{z}(t'_k) = \sum_{n=-\infty}^{\infty} h_W[n]x(t_k - t_n) \tag{4.4}$$

In this case, the coefficients of the filter $h_W[n]$ can be computed using the Wiener-Hopf equations [102]. By applying the Fourier transform to these equations, the transfer function of the filter is finally obtained:

$$H_W(f) = \frac{P_{zz}(f)}{P_{zz}(f) + P_{ww}(f)} = \frac{\eta(f)}{\eta(f) + 1} \tag{4.5}$$

where $P_{zz}(f)$ and $P_{ww}(f)$ are the PSD of the original signal and the noise respectively, and $\eta = \frac{P_{zz}(f)}{P_{ww}(f)}$ represents the local SNR in a frequency f. Obviously, $0 < H_W(f) < 1$, tending to 1 (to 0) in spectral bands with high (low) SNR. Hence, the Wiener filter enhances (attenuates) the signal in those bands with high (low) SNR, and the autocorrelation of the process to be interpolated is a natural indicator of the relevance of each spectral band in terms of SNR.

4.2.2   Yen Regularized Interpolator

Time Domain Analysis. Inspired by Shannon's sampling theorem, *a priori* information can be used for band-limited signal interpolation by means of a *sinc* kernel. In this case, the signal is modeled with a *sinc* kernel expansion as:

$$x(t'_k) = z(t'_k) + w(t'_k) = \boldsymbol{a}^T \boldsymbol{s}_k + w(t'_k) \qquad \text{for } k = 1, \dots, K \tag{4.6}$$

with $\boldsymbol{s}_k$ a $N \times 1$ column vector with components $\boldsymbol{s}_k[n] = \text{sinc}(\sigma_0(t'_k - t_n))$, where $\text{sinc}(t) = \frac{\sin(t)}{t}$ and parameter $\sigma_0 = \frac{\pi}{T_0}$ is the *sinc* function bandwidth. Then, the interpolator can be stated as follows:

$$\hat{z}(t'_k) = \boldsymbol{a}^T \boldsymbol{s}_k \qquad \text{for } k = 1, \dots, K \tag{4.7}$$

When LS strategy is used to estimate $\boldsymbol{a}$, Yen's solution ([89], Theorem IV) is obtained. If a regularization term is used to prevent numerical ill-posing, $\boldsymbol{a}$ is obtained by minimizing:

$$\mathcal{L}_{reg} = \frac{1}{2}\|\boldsymbol{x} - \boldsymbol{S}\boldsymbol{a}\|^2 + \frac{\delta}{2}\|\boldsymbol{a}\|^2 \tag{4.8}$$

where $\boldsymbol{S}$ is a square matrix with elements $\boldsymbol{S}(n, k) = \mathrm{sinc}(\sigma_0(t_n - t'_k))$, and δ tunes the trade-off between solution smoothness and the errors in the observed data. In this case, $\boldsymbol{a}$ is given by:

$$\boldsymbol{a} = \left(\boldsymbol{S}^2 + \delta\boldsymbol{I}_N\right)^{-1}\boldsymbol{S}\boldsymbol{x} \tag{4.9}$$

The use of the regularization term leads to solutions that are suboptimal in the MSE sense.

Frequency Domain Analysis. An asymptotic analysis similar to the one presented for the Wiener filter can be done based on (4.9) and (4.7). Using a continuous time equivalent model for the interpolation algorithm (see Section 4.3 for further details) the interpolation algorithm can be interpreted as a filtering process over the input signal, this is:

$$\hat{z}(t) = h_Y(t) * x(t) \tag{4.10}$$

where $*$ denotes the convolution operator. Now, the transfer function of the filter is given by:

$$H_Y(f) = \frac{P_{ss}(f)}{P_{ss}(f) + \delta} \tag{4.11}$$

where $P_{ss}(f)$ is the PSD of $sinc(\sigma_0 t)$ (since this one is deterministic, $P_{ss}(f) \equiv |S(f)|^2$ with $S(f)$ the Fourier transform of the *sinc* function), which is a rectangular pulse of width σ_0. $H_Y(f)$ takes the value $\frac{1}{1+\delta}$ inside the passband of $P_{ss}(f)$ and 0 outside. Therefore, if σ_0 is equal to the signal bandwidth, the filter attenuates the noise outside the signal band and does not affect the components inside the band. A comparison between (4.11) and (4.5) reveals that both interpolators can be interpreted as filters in the frequency domain, but in the case of Yen's algorithm the local SNR $\eta(f)$ is approximated by the *sinc* kernel PSD, $P_{ss}(f)$.

4.2.3   Support Vector Machine Interpolation

An alternative to the use of LS criterion in nonuniform interpolation is the SVM approach [103]. Next the procedure presented in [99] is summarized, in order to use the most relevant results in the next section.

Let us assume a nonuniform interpolator of the form:

$$\hat{z}(t'_k) = \boldsymbol{a}^T\boldsymbol{\varphi}(t'_k) \tag{4.12}$$

where $\boldsymbol{a}$ is a $N \times 1$ weight vector which defines the solution and $\boldsymbol{\varphi}(t'_k)$ is a nonlinear transformation of the time instants to a Hilbert space $\mathcal{H}$, provided with a dot product:

$$\boldsymbol{\varphi}(t_1)^T\boldsymbol{\varphi}(t_2) = K(t_1, t_2) \tag{4.13}$$

with $K(\cdot, \cdot)$ being a kernel that satisfies the Mercer's Theorem [97]. The solution of the SVM is stated in terms of dots products of the transformed input samples. Hence, (4.13) indicates that the nonlinear transformation in (4.12) will be done implicitly by means of a kernel function.

In order to construct the interpolator, vector $\boldsymbol{a}$ must be found. For this purpose, following the structural risk minimization principle, a cost function on the errors in the sampling instants plus a regularization term should be minimized [97]. In this work, a ε-Huber cost [104] function is used:

$$\mathcal{L}_{\varepsilon H}(e_n) = \begin{cases} 0, & |e_n| < \varepsilon \\ \frac{1}{2\gamma}(|e_n| - \varepsilon)^2, & \varepsilon \leq |e_n| < \varepsilon + \gamma C \\ C(|e_n| - \varepsilon) - \frac{1}{2}\gamma C^2, & |e_n| \geq \varepsilon + \gamma C \end{cases} \tag{4.14}$$

where $e_n = x(t_n) - \hat{z}(t_n)$, and ε, γ and C are free parameters to be adjusted using *a priori* knowledge (see [105] for further details). Using this cost function, the primal functional to be optimized in order to obtain $\boldsymbol{a}$ is:

$$\mathcal{L}_p = \frac{1}{2}\|\boldsymbol{a}\|^2 + \frac{1}{2\gamma}\sum_{n \in I_1}(\xi_n^2 + \xi_n^{*2}) + C\sum_{n \in \mathcal{I}_2}(\xi_n + \xi_n^*) - \sum_{n \in \mathcal{I}_2}\frac{\gamma C^2}{2} \tag{4.15}$$

subject to the constraints:

$$\begin{aligned} x_n - \boldsymbol{a}^T\boldsymbol{\varphi}(t_n) &\leq \varepsilon + \xi_n \\ -x_n + \boldsymbol{a}^T\boldsymbol{\varphi}(t_n) &\leq \varepsilon + \xi_n^* \end{aligned} \tag{4.16}$$

where $\xi_n^{(*)} = \max\{0, |e_n| - \varepsilon\}$ are the error magnitude outside the insensitivity region for positive and negative errors, respectively, and sets $\mathcal{I}_1$ and $\mathcal{I}_2$ contains the indices of errors that lie in the quadratic and linear sections of the cost function, respectively [104].

The SVM approach allows to control the estimator smoothness through the first term of (4.15) . Also, due to the insensitivity region of the cost function the solution is sparse, meaning that only a subset of the original signal samples are used for building the solution, and hence the computational burden of the interpolator is reduced. Finally, the cost function approaches maximum likelihood (ML) for Gaussian noise and is robust against non-Gaussian interferences as impulsive noise [104].

Using the Lagrange method for solving the problem in (4.15)-(4.16), the solution is:

$$\boldsymbol{a} = \sum_{n=1}^{N}(\alpha_n - \alpha_n^*)\boldsymbol{\varphi}(t_n) = \sum_{n=1}^{N}\beta_n\boldsymbol{\varphi}(t_n) \tag{4.17}$$

where $\beta_n = \alpha_n - \alpha_n^*$ are the Lagrange multipliers for constraints in (4.16) [99]. Finally, by combining (4.12) and (4.17), and expanding the scalar product into a summation, the interpolated signal is given by:

$$\hat{z}(t_k') = \sum_{n=1}^{N}\beta_n\boldsymbol{\varphi}(t_n)^T\boldsymbol{\varphi}(t_k') = \sum_{n=1}^{N}\beta_n K(t_n, t_k') = \sum_{n=1}^{N}\beta_n K(t_n - t_k'). \tag{4.18}$$

where for the last equality it has been assumed that the kernel fulfills the condition $K(x, y) = K(x - y)$. In that case, the kernel can be thought as a time-invariant system that provides a convolutional model for the solution [106]. Conversely, it is known that for a function $K(\cdot, \cdot)$ to be a valid shift invariant kernel, it is a necessary and sufficient condition that it has a non negative Fourier transform [107].

4.2.4   Some Comparative Remarks

It can be seen that both Yen and Wiener filter algorithms use the LS (regularized for Yen method) criterion. However, Wiener algorithm is linear with the observations, and it does not assume any *a priori* decomposition of the signal in terms of building functions. Instead, it relies on the knowledge of the autocorrelation function, which can be hard to be estimated in a number of applications. Alternatively, Yen algorithm is nonlinear with respect to the observations and assumes an *a priori* model based on *sinc* kernels. Hence, the knowledge of the signal autocorrelation is not needed. The SVM interpolation uses a different optimization criterion, which is the structural risk minimization, and its solution is nonlinear with respect to the observations since it assumes a signal decomposition in terms of a given Mercer kernel.

4.3   Spectrally Adapted Mercer Kernels

In this section, a Continuous-time Equivalent System for Nonuniform Interpolation (CESNI) is presented, which represents the solution of the interpolation problem based on the SVM approach. The objective of presenting a continuous-time equivalent system is to establish a frequency domain description of the interpolation SVM algorithm. Based on the analysis of the CESNI model, several effective Mercer kernels are proposed for SVM-based nonuniform sampling interpolation. These kernels account for different degrees of spectral adaptation to the observed data.

Definition 1 (CESNI) Given the SVM procedure described in Section 4.2.3, its continuous-time equivalent system is defined as:

$$\hat{z}(t) = \mathcal{T}\{x(t)\} \tag{4.19}$$

with $x(t) = z(t) + w(t)$, $\hat{z}(t)$ the estimation of $z(t)$, and $\mathcal{T}\{\cdot\}$ a continuous time non-linear feedback system. If $\mathcal{T}\{\cdot\}$ is evaluated in a set of N time instants $\{t_n, n = 1, \ldots, N\}$ taken from a uniform random distribution, the system defined by the solution in Section 4.2.3 is obtained.

In order to define $\mathcal{T}\{\cdot\}$, recall that Lagrange coefficients are related with the observed data by the derivative of the cost function, i.e. $\beta_n = \mathcal{L}'_{\varepsilon H}(e_n) \equiv \frac{d\mathcal{L}_{\varepsilon H}(e_n)}{de}$ (proof can be found in [105]) and that $e_n = x(t_n) - \hat{z}(t_n)$. Using these results, it can be seen that the solution defined in (4.18) can be modeled
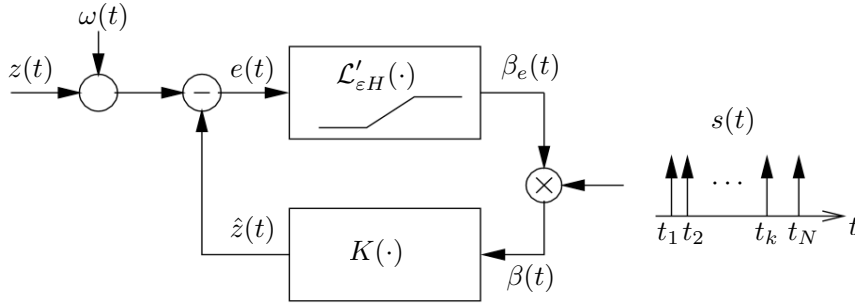
Figure 4.1: *CESNI for the SVM interpolation algorithm. The interpolated signal $\hat{z}(t)$ is built by filtering the continuous-time sampled version of the Lagrange coefficients $\beta(t)$ with the SVM kernel $K(t)$.*

as a feedback system, and it will be defined $\mathcal{T}\{\cdot\}$ as its continuous time version, which is represented in Figure 4.1. CESNI elements are subsequently scrutinized.

Property 1 (Residual Continuous Time Signal) Given the CESNI of SVM algorithm for unidimensional signal interpolation, the residual continuous time signal is given by:

$$e(t) = x(t) - \hat{z}(t) \tag{4.20}$$

and it corresponds to the continuous time signal from which the residuals are sampled.

Property 2 (Model Coefficient Continuous-time Signal) In the CESNI of SVM algorithm for unidimensional signal interpolation, the Model Coefficient Continuous-time Signal is given by the following set of equations

$$\beta_e(t) = \mathcal{L}'_{\varepsilon H}\left(e(t)\right) \tag{4.21}$$

$$s(t) = \sum_{n=1}^{N} \delta(t_n) \tag{4.22}$$

$$\beta(t) = \beta_e(t) \times s(t) = \sum_{n=1}^{N} \beta_n \delta(t_n) \tag{4.23}$$

where $\beta_e(t)$ is the equivalent continuous signal for the Lagrange coefficient sequence, $\beta(t)$ is its sampled version, and $\delta(t)$ represents the Dirac's delta function. Hence (4.23) represents the discrete set of the model coefficients given by the SVM algorithm as obtained by random sampling of a continuous time signal $\beta_e(t)$.

Property 3 (Recovered Continuous-time Signal) In the CESNI of SVM algorithm for unidimensional signal interpolation, the recovered continuous-time signal is given by:

$$\hat{z}(t) = K(t) * \beta(t) \tag{4.24}$$

which shows that the kernel works as a linear, time-invariant filter and that the Lagrange coefficients are the inputs to that filter.

Consequently, denoting the PSD of $\hat{z}(t)$, $K(t)$, and $\beta(t)$ as $P_{\hat{Z}}(f)$, $P_{\mathcal{K}}(f)$, and $P_{\mathcal{B}}(f)$, respectively, the recovered signal PSD is given by $P_{\hat{Z}}(f) = P_{\mathcal{K}}(f)P_{\mathcal{B}}(f)$, and hence it can be concluded that the kernel is shaping the output in the frequency domain. On the one hand, an appropriate adaptation of the kernel spectrum to the one of the original signal shall improve the interpolation performance. On the other hand, if the signal and kernel spectra are not in the same band, the performance shall be really poor. This would be the case of the *sinc* or the Gaussian kernels when used for band-pass signal interpolation. This suggests that Mercer kernels represent the transfer function which should emphasize the recovered signal in those bands with higher SNR. Looking at the Wiener filter transfer function in (4.5) it can be seen that the signal autocorrelation could be used for this purpose, since its Fourier transform is the PSD of the signal.

Nevertheless, despite these are well known principles of signal processing, little attention has been paid to the possibility of using spectrally adapted Mercer kernels in SVM-based interpolation algorithms. According to these considerations, several Mercer kernels are proposed with different degrees of spectral adaptation, namely, modulated and autocorrelation kernels.

Property 4 (Modulated Kernels) If $z(t)$ is a bandpass signal centered at f_0, modulated versions of RBF and sinc *kernels given by*

$$K(t_n, t'_k) = sinc(\sigma_0(t_n - t'_k)) \sin(2\pi f_0(t_n - t'_k)) \qquad (4.25)$$

$$K(t_n, t'_k) = \exp\left(-\frac{(t_n - t'_k)^2}{2\sigma_0^2}\right) \sin(2\pi f_0(t_n - t'_k)) \qquad (4.26)$$

are suitable Mercer kernels. Moreover, their spectra are adapted to the signal spectrum. Note that in this case, an additional free parameter ω_0 has to be settled for the kernel.

Property 5 (Autocorrelation Kernels) Similarly to the Wiener filter, the autocorrelation of the signal to be interpolated ($z(t)$) or its noisy observations ($x(t_n)$) can be used to define the following kernels:

$$K_{ideal}(t_n, t'_k) = r_{zz}(t_n - t'_k) \qquad (4.27)$$

$$K_{est}(t_n, t'_k) = r_{xx}(t_n - t'_k) \qquad (4.28)$$

which are the ideal (actual) autocorrelation function computed from the underlying process and autocorrelation function estimated from the observations, respectively.

If the second order statistics of the process are known, the kernel defined in (4.27) can be used. When the autocorrelation of the process is not known, an estimation procedure must be used. Note that this problem is not exclusive of the SVM interpolator, but is also present in the Wiener case. However, as shown in the experiments, due to the robustness of the SVM algorithm, simple procedures for estimating the autocorrelation functions can be used.
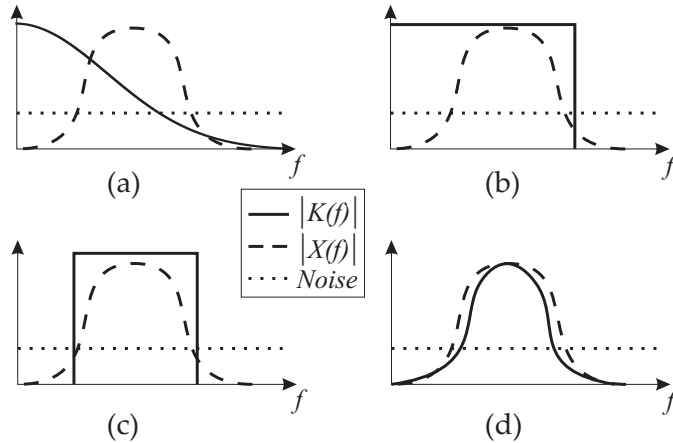
Figure 4.2: *Illustration of the spectral adaptation of the kernels to the observations for a band pass signal: (a) with RBF kernel, (b) with* sinc *kernel, (c) with modulated* sinc *kernel, and (d) with autocorrelation kernel.*

Figure 4.2 illustrates the effect of using different kernels. The signal to be interpolated is band-pass, so its interpolation with low-pass kernels, either RBF (a) or *sinc* (b), can be a loose spectral adaptation which indeed emphasizes the noise in the low-pass band. In (c), the use of a modulated band-pass *sinc* kernel allows us to enhance the transfer function spectral adaptation to the signal spectral profile, which is further refined in (d) when using the estimated autocorrelation as interpolation kernel.

4.4   Experiments

In this section, the described algorithms are experimentally assessed. Their performance are analyzed when interpolating a band-pass signal. Then, the interpolation of two signals is evaluated with very different spectra, to assess the impact of the kernel spectral adaptation. Different levels of nonuniformity are also tested in the sampling process, different number of training samples, and non-Gaussian noise. In a second set of experiments, the algorithms with several one-dimensional functions are tested with different and representative spectral profiles. Finally, the applicability of SVM algorithms is illustrated by interpolating a set of Heart Variability Rate (HRV) signals, which are nonuniformly sampled time series by construction.

4.4.1   Experimental Setup

The interpolation algorithms is benchmarked that are summarized in Table 4.1, including all the methods described above and the functionally weighted version of the Lagrange interpolator described in [95].

For *Wien* and *SVM-Corr* algorithms the autocorrelation function had to be estimated from the observed samples. Note that the autocorrelation had

Algorithm description	Label
Yen algorithm with regularization	*Yen*
Weighted Lagrange interpolator	*WLI*
Wiener filter with estimated autocorrelation	*Wien*
Wiener filter with actual (ideal) autocorrelation	*Wien-Id*
SVM with low-pass RBF kernel	*SVM-RBF*
SVM with low-pass *sinc* kernel	*SVM-Sinc*
SVM with estimated autocorrelation kernel	*SVM-Corr*
SVM with actual (ideal) autocorrelation kernel	*SVM-CorrId*

Table 4.1: *List of algorithms benchmarked in the experiments.*

to be computed for every time shift $\tau = t_n - t'_k$, so it had to be estimated over a grid with a resolution much higher than that of the observed samples. Hence, two steps might be carried out: (1) estimating the autocorrelation from the observed samples and (2) interpolating it for every time shift $\tau = t_n - t'_k$. Although many methods exist for this purpose, a simple procedure is used based on frecuency-domain interpolation. The main reason for this choice is that the overall procedure is simple and well-stablished. Specifically, the method consist of (1) a Lomb Periodogram to estimate the PSD of the signal [108], and (2) a zero padding technique in the frequency domain to carry out the interpolation step. Finally, and inverse Fourier transform of the zero padded PSD was used for computing the autocorrelation function.

For the synthetic experiments, a one-dimensional signal with spectral information contained in $[-B/2, B/2]$ was interpolated. This signal is sampled in a set of L unevenly time instants, different for each realization, with an average sampling interval T, such that $BT = 1$. The interpolation instants lied on a uniform grid with step $T_{int} = T/F$, with F the interpolation factor. The nonuniform sampling time instants were simulated by adding a random quantity taken from a uniform distribution in the range $[-u, u]$ to the equally spaced time instants $t_k = kT, k = 1, 2, \ldots, L$. In order to simplify the computation of the kernels, each time instant was rounded to be a multiple of T_{int}. The performance of each algorithm was measured by using the S/E indicator, that is, the ratio between the power of the signal and the power of the error in dB. Each experiment was repeated 50 times.

4.4.2   Interpolation of Band-Pass Signals

To get a first insight of the impact of the kernel spectral adaptation on the algorithms performance, they are compared when interpolating a test signal
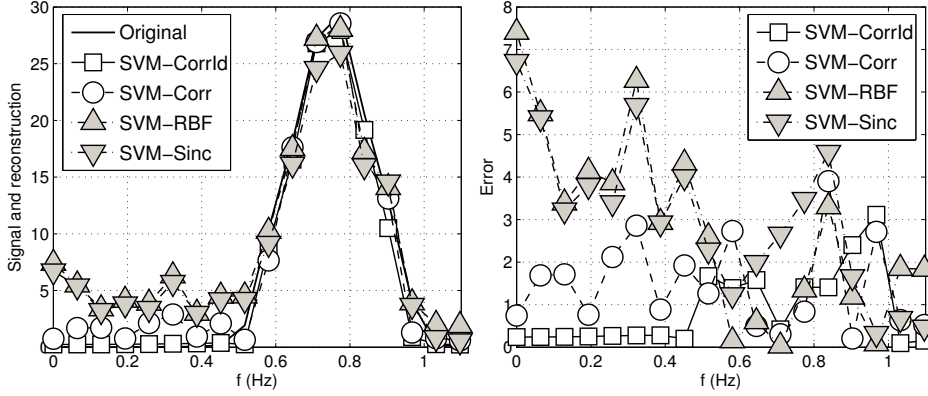
Figure 4.3: *Example of the spectra of the original and reconstructed signals (left) and the error of the reconstructions (right) for the Modulated Sinc Squared Function. T = 0.5 s, L = 32, SNR = 10 dB and u = T/10.*

consisting on a modulated squared *sinc* function (MSSF), defined by:

$$f(t) = sinc^2 \left(\frac{\pi}{T_0} t \right) \cos \left(2\pi f_1 t \right) \tag{4.29}$$

where T_0 and f_1 are chosen in order that the signal bandwidth fulfills BT = 1. The spectrum of this signal is a triangle centered at f_1. The experiment was carried out with $L = 32$ samples, $T = 0.5$ s, a non-uniformity parameter $u = T/10$, and for Gaussian noise with different values of SNR. Figure 4.3 shows the spectra of the original and reconstructed signals and the error of reconstruction of the Yen and the SVM algorithms. The error at low frequencies (where there is no significant signal power) is high for the SVM with low-pass kernels, since in this band the noise is enhanced by the kernel spectrum. On the contrary, it can be seen that the error produced by the autocorrelation kernel is quite lower, since it is adapted to the signal spectrum.

Table 4.2 represents the performance of all the algorithms for different SNRs. It can be observed that both SVM-CorrId and Wien-Id methods, which are based on the perfect knowledge of the signal autocorrelation, clearly outperform the other algorithms. Although the solution presented in (4.3) is optimal in the MSE sense, it suffers from numerical ill-posing due to the inversion of the correlation matrix, which usually presents a very high condition number. The SVM with estimated autocorrelation kernels also has a good performance, only 1 to 2 dB lower than the ideal version. Note that it clearly outperforms the non-ideal version of the Wiener filter. WLI algorithm provides intermediate S/E values, although it computational complexity is the lowest one. Finally, SVM with low pass kernels and Yen algorithms provide a performance lower than that of the others.

Alg.	40 dB	30 dB	20 dB	10 dB
Yen	35.1 (0.5)	29.3 (0.9)	20.3 (1.1)	10.4 (1.3)
Wien	39.8 (1.2)	30.0 (1.0)	20.2 (1.1)	10.1 (1.3)
WLI	38.4 (2.4)	29.4 (1.2)	20.1 (1.3)	10.0 (1.4)
Wien-Id	**41.2 (1.2)**	**32.3 (1.4)**	**22.6 (1.7)**	**13.1 (1.8)**
SVM-Corr	39.5 (1.9)	30.9 (1.4)	22.0 (1.3)	12.6 (1.6)
SVM-CorrId	**41.7 (1.4)**	**32.9 (1.4)**	**23.5 (1.6)**	**14.9 (1.6)**
SVM-RBF	27.4 (1.0)	26.1 (0.7)	19.2 (0.7)	10.8 (1.2)
SVM-Sinc	34.1 (0.7)	28.9 (1.1)	20.2 (1.1)	10.9 (1.2)

Table 4.2: *Mean S/E and (std) with SNR for a band-pass signal interpolation, T = 0.5 s, L = 32 and u = T/10. Two best in bold.*

4.4.3   Effect of the Sampling Process and the Noise

Nonuniform sampling

Now, the effect of increasing the nonuniformity parameter u from very small values to half of the sampling period is examined. The sampling for u very small is almost uniform, while with $u = T/2$ the samples can be placed at any time instant. For this purpose, it is used the MSSF and a set of logarithmically spaced values for u, from 0.001 to $T/2$, using $SNR = 20$dB, and with the rest of parameters as in Section 4.4.2.

Figure 4.4 shows the mean and standard deviation of the S/E for all the algorithms for each value of u. *SVM-CorrId* is the most robust algorithm respect to the nonuniform sampling. When u takes its maximum value, the difference between the *SVM-CorrId* and the rest of algorithms is also maximal and rises up to 5 dB. Interestingly, *Wien-Id* behaves similar to *SVM-CorrId* for low values of u, which was the expected behavior since both of them use the same prior knowledge about the second order statistics of the signal. However, when u exceeds 10^{-2}, the performance of the Wiener filter degrades fast, which can be explained by the loss of stationarity caused by the nonuniform sampling. The robust nature of SVM interpolation is not affected in the same manner by this effect. Finally, SVM-Corr algorithm shows an intermediate performance, between SVM-CorrId and the rest of the algorithms.

Robustness Against Impulse Noise

SVM algorithms have shown good performance when impulse noise is present at the data [99]. All the proposed algorithms are tested with this noise, which was generated with the Bernouilli-Gaussian (BG) function $n_n^{BG} = v_n \lambda_n$ where v_n is a random process with Gaussian distribution and power σ_{BG}^2 and where λ_n is a random process which takes the value 1 with probability p and
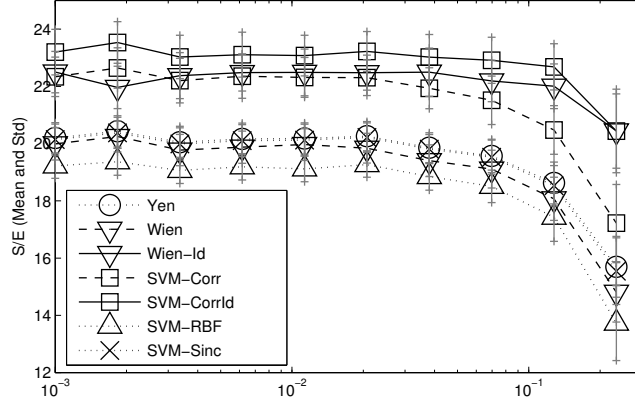
Figure 4.4: *S/E ratio for different values of the nonuniformity parameter (u) SNR = 20 dB, T = 0.5 s, L = 32.*

the value 0 with probability $1 - p$. A value of $p = 0.1$ was considered. In order to compare the robustness of each algorithm when this type of noise was present, the signal to impulse noise ratio (SIR) indicator is used, defined by:

$$SIR_{dB} = 10 \log_{10} \left(\frac{E\{x_n - n_n^G - n_n^{BG}\}}{\sigma_{BG}^2} \right) \qquad (4.30)$$

Table 4.3 shows the performance (in terms of S/E) of the proposed algorithms for different values of SIR, $SNR = 10$dB, and the rest of parameters as in Section 4.4.2. In this case, due to the inherent robustness to outliers of the SVM formulation, all the SVM algorithms are robust against impulse noise, while the performance of the two Wiener filter algorithms degrades for very low SIR, hence confirming the superiority of the SVM-based solution in the case of non-Gaussian noise. Again, *SVM-CorrId* provides de best results for all SIR values, and hence shows an interesting robustness with different types of noise.

4.4.4   Performance for Different Type of Signals

In this experiment the performance of the analyzed algorithms is tested with a database of functions with different kinds of spectrum. Figure 4.5 shows the spectra of the eight functions which have been used for this purpose. In this case, the number of samples is $L = 64$, with $T = 0.24s$ and $u = T/10$. The noise was Gaussian with $SNR = 10$dB. Table 4.4 shows the mean S/E and its standard deviation in brackets. *SVM-CorrId* with the ideal autocorrelation kernel performs well in all the cases, followed by *SVM-Corr* most of the times. In the case of the chirp function, the *SVM-Sinc* behaves better than the *SVM-Corr*, since its spectrum is similar to the one of that function. However, the performance of this algorithm degrades for other functions (like PST or POL). Based on these results, it can be concluded that the SVM with autocorrelation kernels have very good performance independently of

Alg.	20 dB	15 dB	10 dB	5 dB	0 dB	-5 dB
Yen	10.5 (1.3)	10.2 (1.2)	9.9 (1.1)	8.7 (1.5)	6.8 (2.0)	4.5 (2.7)
Wien	10.0 (1.3)	9.8 (1.2)	9.3 (1.2)	7.9 (1.6)	5.7 (2.2)	2.9 (3.3)
Wien-Id	**13.3 (1.8)**	**13.1 (1.8)**	**12.9 (1.7)**	**12.0 (1.9)**	**10.0 (2.3)**	**8.8 (3.5)**
SVM-Corr	12.6 (1.6)	12.1 (1.3)	11.9 (1.5)	10.6 (1.8)	8.2 (2.7)	5.7 (3.1)
SVM-CorrId	**14.5 (1.8)**	**14.3 (1.4)**	**14.1 (1.6)**	**13.0 (2.1)**	**10.9 (2.3)**	**10.0 (2.7)**
SVM-RBF	10.6 (1.2)	10.3 (1.3)	10.1 (1.2)	8.9 (1.6)	6.6 (2.0)	4.4 (2.8)
SVM-Sinc	11.0 (1.1)	10.7 (1.2)	10.7 (1.2)	9.6 (1.5)	7.5 (2.1)	5.3 (2.5)

Table 4.3: *Mean S/E and (std) with SIR (SNR = 10 dB) for a band pass signal interpolation, and $u = T/10$. Two best in bold.*

Alg.	CHRP	3SIN	PTR	SAW	FBRK	POL	BPSK	PLST
Yen	11.1 (1.0)	12.5 (0.9)	11.2 (1.0)	6.7 (0.5)	**11.6 (0.9)**	13.3 (1.1)	9.3 (0.7)	13.2 (1.1)
Wien	9.6 (1.0)	9.1 (0.9)	9.1 (0.9)	5.1 (0.7)	9.0 (0.9)	9.4 (0.9)	8.5 (0.9)	9.4 (1.0)
Wien-Id	11.3 (1.1)	8.9 (1.3)	**13.4 (1.0)**	**7.4 (0.9)**	10.7 (1.0)	9.4 (0.4)	10.8 (1.1)	10.0 (0.4)
SVM-Corr	11.0 (1.0)	**13.4 (1.3)**	12.2 (1.2)	7.2 (0.6)	11.5 (1.0)	**16.7 (1.4)**	**11.6 (0.8)**	**15.7 (1.3)**
SVM-CorrId	**13.0 (1.1)**	**15.2 (1.4)**	**14.1 (1.2)**	**9.1 (0.9)**	**12.9 (1.0)**	**18.7 (1.8)**	**13.4 (0.9)**	**17.5 (1.4)**
SVM-RBF	10.7 (0.9)	11.5 (0.9)	10.8 (1.0)	6.8 (0.7)	11.1 (0.9)	14.6 (1.0)	10.0 (0.8)	14.6 (1.3)
SVM-Sinc	**11.3 (0.9)**	12.6 (1.0)	10.8 (1.0)	6.6 (0.6)	11.4 (0.9)	13.2 (1.1)	9.3 (0.8)	13.1 (1.2)

Table 4.4: *Mean S/E and (std) for different functions (SNR = 10 dB, Gaussian noise, and $u = T/10$). Two best in bold.*
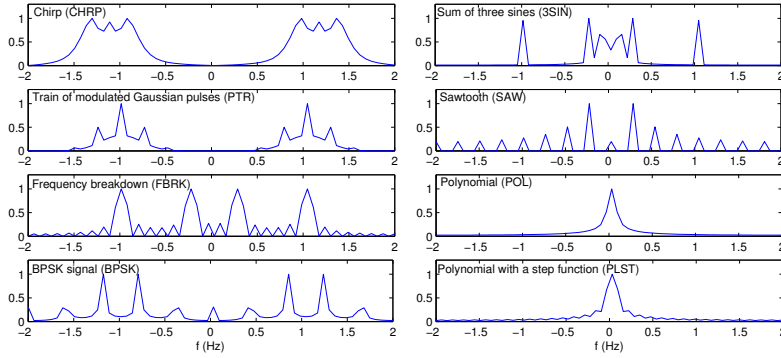
Figure 4.5: *Spectra of the band-limited signals used for comparing the algorithms. A diversity of spectral profiles have been used for this set of experiments.*

the signal spectrum, since they are able to adapt the kernel spectra.

4.4.5 Interpolation of Hear Rate Variability RR-Interval Time Series

Introduction

HRV, as described in Section 1.4, is a relevant marker of the (ANS) control on the heart. This marker has been proposed for risk stratification of lethal arrhythmias after acute myocardial infarction (AMI), as well as for prognosis of sudden death events [4]. When analyzing the HRV time series, the sequence of time intervals between two consecutive beats (called RR-Interval time series) is often used, which is by nature sampled at unevenly spaced times instants. Advanced methods for spectral analysis have shown that the HRV signal contains well defined oscillations that account for different physiological information. The spectrum of the HRV could be divided into three bands: VLF band, between 0 and 0.03 Hz; LF, between 0.03 and 0.15 Hz; and HF, between 0.15 and 0.4 Hz. LF and HF bands have been shown to convey information about the ANS control on the heart rhythm, representing the balance between the sympathetic and parasympathetic contributions. Spectral based methods, such as Fourier Transform or Auto-regressive Modeling, require the RR-interval time series to be resampled into a uniform sampling grid.

The analysis of the HRV is often performed on 24 hours Holter recordings, and a common procedure is to divide the RR-Intervals time series into 5 minutes segments, in order to study the evolution of the spectral components along time. Classic techniques for computing the spectrum of HRV signals aim to obtain a good estimate of LF and HF components, but due to the nonuniform sampling and the noisy nature of the measurements, estimating the HRV spectrum is a very hard problem, specially in LF and HF ranges. In this experiment, the SVM algorithms are applied for interpolating two

HRV signals with this purpose.

Methodology

A 24 hours Holter recording from a patient with Congestive Heart Failure (labelled with a D) and another one from a healthy patient (labelled with an H) have been used for this experiment. These recordings were divided into 5-minute segments, and two preprocessing steps were done: (1) discarding the segments with more than a 10 % of invalid measurements, usually due to low signal amplitude or ectopic origin of the beat; (2) applying a detrending algorithm to subtract the mean value and the constant trend of each segment, which introduces distortion in the VLF region. Two algorithms were compared: SVM-Corr and SVM-RBF. Both algorithms were used to interpolate each segment, by using the RR-intervals in each segment as the training samples, and interpolating the signal over a uniform grid of 500 ms.

The autocorrelation kernel for each patient was estimated as follows: (1) a set of segments (around 20) with low noise and high power in the LF and HF regions were previously selected; (2) an estimate of the autocorrelation of each of these segments was computed by using the method described in Section 4.3, over a fine grid with a step of 5 ms; and (3) a mean autocorrelation was calculated from this set of estimates, in order to reduce the noise level. A subjective evaluation based on the spectrograms and some examples have been used to compare them.

Results

The autocorrelation kernels and their spectra for both patients D and H are shown in Figure 4.6. Although they are still noisy, note that in patient D only one peak is present (probably due to the disease) and both peaks LF and HF are present in patient H. Using the SVM-RBF and the SVM-Corr with these kernels each segment was interpolated. The main effect was that SVM-Corr was able to filter the noise in order to highlight the LF and HF peaks better than the RBF algorithm, specially where the density of noise was very high in frequency bands out of the regions of interest, as can be seen in the examples for both patient shown in Figure 4.7(a) for patient D and Figure 4.7(b) for patient H. For this last one, two details for a region of interest and for a region with noise are shown in lower plots. In the three examples it can be checked that the SVM-Corr was able to reduce the noise level better than the RBF algorithm.

Figure 4.8 shows the spectrograms of the original and interpolated signals. For both patients, LF and HF peaks were clearer with the SVM-Corr than with the SVM-RBF. A short period of the original and estimated signals is shown in Figure 4.9, in which two peaks can be identified which correspond to non-ventricular beats or bad measurements. Note that the SVM-Corr algorithm is able to filter this misleading measurements much better than SVM-RBF
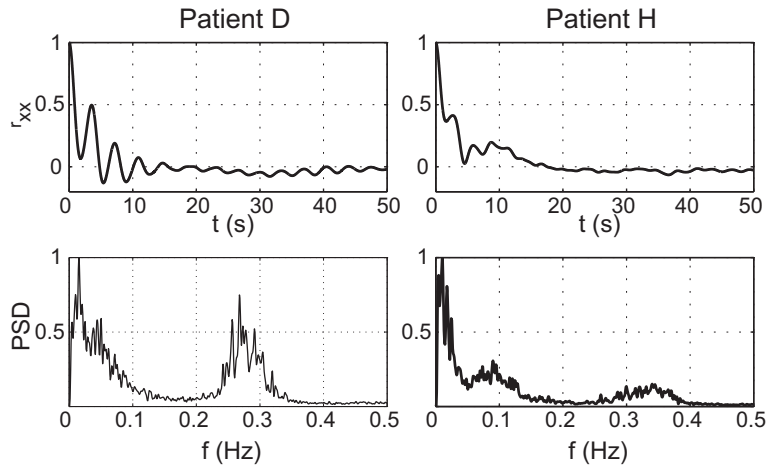
Figure 4.6: *Autocorrelation kernels in time and frequency for the HRV segments of patients* D *and* H.
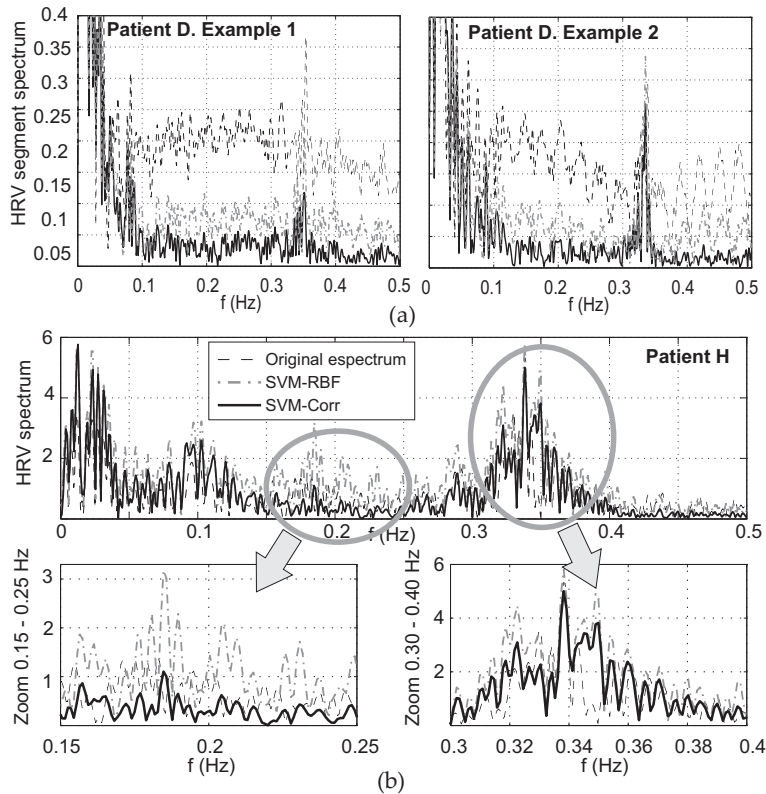
Figure 4.7: *Examples of HRV segments of patients* D *(a) and* H *(b). Two details of the HRV spectrum for patient* H *are shown in the lower plots.*

4.5 Discusion and Conclusions

This chapter resented an SVM framework for nonuniform interpolation based on spectrally adapted Mercer kernels. An spectral interpretation of the classical Yen interpolator was first provided, the Wiener filter, and the SVM interpolation, which motivated us to analyze spectrally adapted kernels for

the SVM algorithm. Among them, the actual and estimated kernels can be computed without a significant increase in complexity, though the actual autocorrelation can be determined in advance only in some specific cases (as in the Wiener filter case).

Several experiments were carried out in which the spectrally adapted kernels were compared with low-pass kernels and with other techniques. The results showed that the SVM with the autocorrelation kernels outperformed the other methods regardless the spectrum of the observed signal. Algorithms for several degrees of sampling nonuniformity, for different amount of samples, and for non-Gaussian noise were also tested, again concluding that the SVM with the autocorrelation kernels were the most robust method. Finally, the proposed algorithm was tested in a real-life problem, which is the interpolation of HRV signals. In this case, the filtering process carried out with the autocorrelation kernel allowed to attenuate the noise level while enhancing the signal power in the frequency bands of interest.

The proposed method can be especially useful when the signal bandwidth is not known. Also, SVM-based algorithms have shown to provide high performance when the number of available samples is low, which is usual in many interpolation scenarios. With respect to the adjustment of the free parameters, it should be noted that, from a Statistical Learning Theory point of view, there is a training stage in which the signal model is built, but free parameters should be checked to be adequate in a validation set given by a different realization. There is evidence in the literature that SVM interpolation algorithms can be approximately adjusted with free parameters in advance (see [95, 103]). Note that the use of autocorrelation kernel avoids tuning the kernel parameters.

Results obtaining using SVM-Corr approach to interpolate RR-interval time series provided robust estimation of PSD. Conventional spectral analysis to assess HRV is very sensitive to noise, artifacts in Holter recordings. The proposed method in this chapter, provided reliable spectral estimations without the needed to perform a complete manually correction of the RR-interval time serie to remove artifact and correct beat misclassification. The main effect was that SVM-Corr was able to filter the noise in order to highlight the LF and HF peaks better than the SVM-RBF method, specially where the density of noise was very high in frequency bands out of the regions of interest.

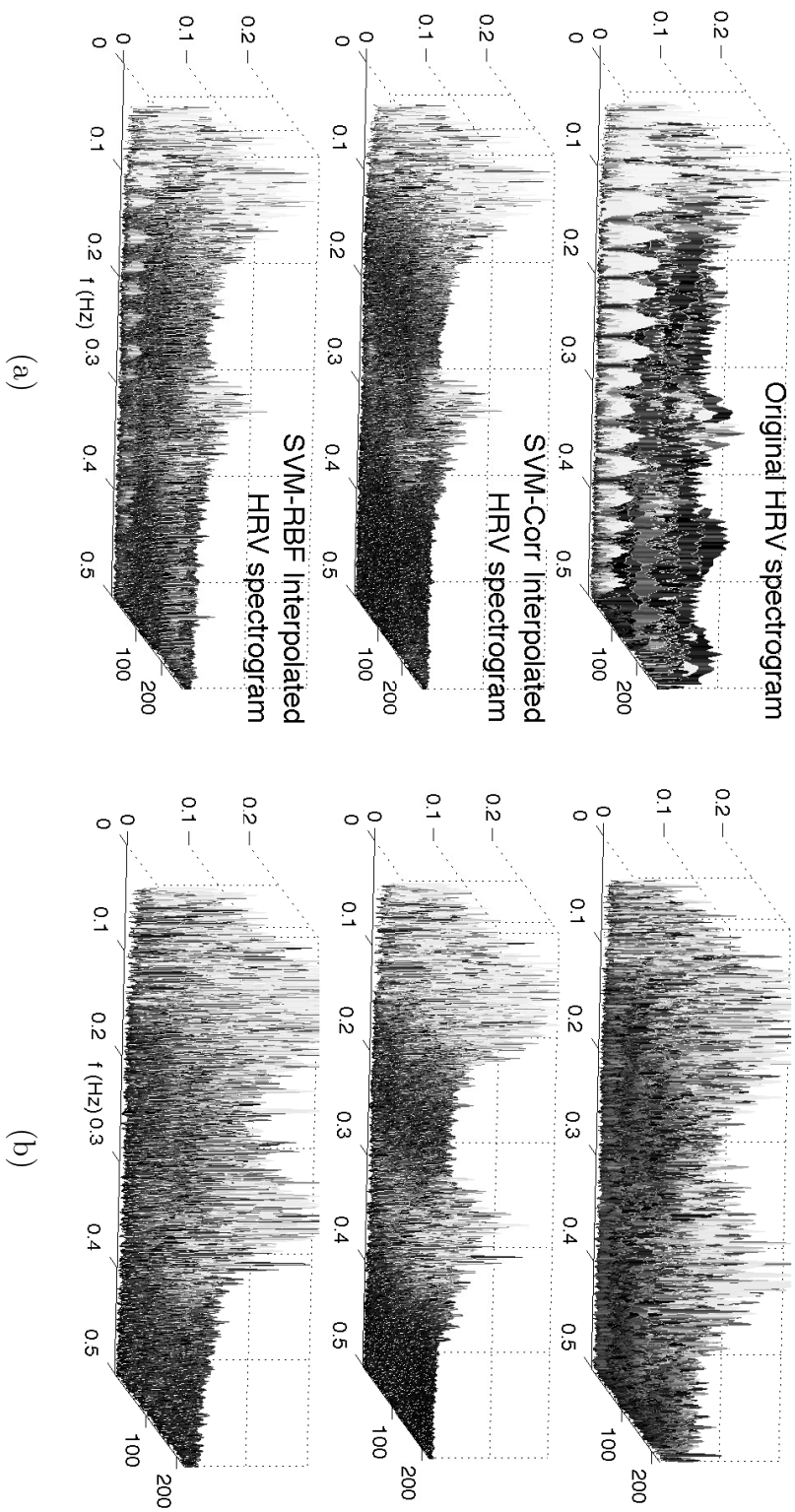Figure 4.8: *Spectrograms for the original (upper plot) and reconstructed signals, for patients D (a) and H (b). Note that noise in intermediate frequencies (0.2 Hz to 0.25 Hz) is lower in the spectrogram filtered with the SVM-Corr method.*
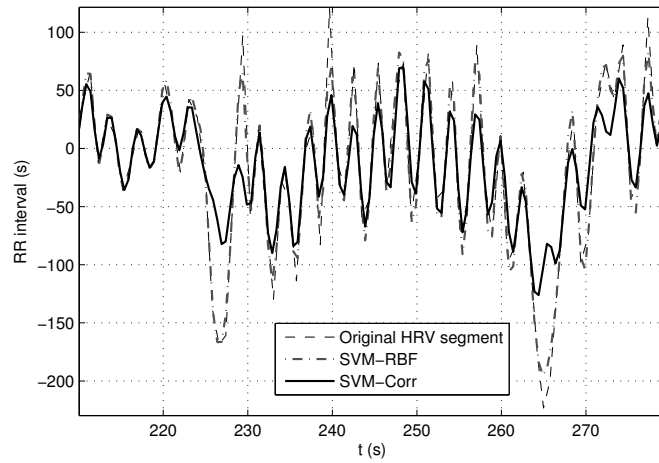
Figure 4.9: *Example of HRV segment of patient* H *and reconstructed signal with SVM-RBF and SVM-Corr algorithms. Note that the spikes have been filterd with the SVM-Corr algorithm.*

Chapter 5

Heart Rate Turbulence Denoising using Support Vector Machines

5.1 Introduction

HRT has been defined as the behavior of the HR after a VPC. Under normal and healthy conditions, HRT consists of a brief increase in HR after the VPC, that is immediately followed by a slower decrease in HR. Measurements on HRT characteristics in long-term (24 hour) Holter recordings have shown a high predictive power for identifying patients with high-risk of cardiac disease [5, 47]. The two parameters that have been mostly used for measuring HRT are the TO and the TS, see Section 1.5. Given that the average VPC-tachogram is usually computed on 24-hour Holter recordings, indices obtained from this template are a long-term measurement of the global state of the patient during a day, and this processing has been shown to be a powerful risk stratifier not only for AMI [5], but also for other diseases such as Chagas [109] or heart failure [110].

Nevertheless, relevant information could be masked by the long-term averaging in this calculation procedure, both from a clinical and from a signal analysis points of view. First, relevant short-time fluctuations in the TS along the day [111] could be hidden by the 24-hour template averaging. Second, several influences of the physiological state can affect the HRT, such as the described effect of HR level that precedes to the VPC on the HRT oscillation amplitude [112, 113]. More specifically, the vegetative tone is probably controlling both the HR level and the HRT oscillation amplitude, but nevertheless, averaging along the different states during the day could result in a reduction of the true magnitude of the HRT fluctuation and in a smoothing not only in noise level, but also in signal level [111, 114]. And third, averaging precludes the comparison of HRT in a given moment to other fluctuating physiological variables. For instance, comparison of long-term Heart Rate Variability (HRV) to long term HRT has been reported [115], but the short-term regulation of the autonomous nervous system on HR can not be studied jointly with the HRT.

Therefore, our hypothesis is that efficient cancelation of physiological

noise from each isolated VPC-tachogram will allow the short-term quantification of TS. This would allow us also to measure the HRT in a higher number of patients, beyond the current limits given by the exclusion criteria for TS averaging with a minimum number of available VPC-tachogram. Accordingly, a signal processing method capable of canceling the noise in a single VPC-tachogram will be a valuable tool to evaluate the short-term HRT, and the development of such method is the purpose of this Chapter. Two main technical issues appear when addressing the signal denoising of a single VPC-tachogram. First, the VPC-tachogram has a very short duration, 15 to 20 samples, and hence, a very robust signal processing method will be required. Second, the HRT is usually measured from 24-hour Holter recordings, which are surely influenced by a variety of noise sources, including the daily activity and the changes in the physiological state of the patient. But a clear gold-standard for HRT behavior and measurement will be needed to benchmark and compare the performance of any proposed denoising algorithm.

To overcome the first issue, the use of SVM is proposed, in particular, the SVM regressor [97]. The SVM framework has been shown specially advantageous in problems with few samples available, due to their excellent generalization performance. The SVM regression based on a robust cost function (the ε-Huber cost), together with the use of bootstrap resampling techniques for tuning the free parameters of the algorithm [104, 116], can provide us with an efficient HRT denoising technique.

Study the performance of the denoising procedure is proposed in a gold standard given by HRT induced with cardiac electrical stimulation (pacing) during EPS, which can be considered an almost noise-free environment, because the patient is maintained at rest. Pacing-induced HRT has started to receive increasing interest, and conditions for its measurement have been established [7, 117, 118, 119, 120]. This gold standard will allow us to quantify the HRT shape in the temporal and spectral domain in an almost noise-free environment, an then to compare the performance of the signal processing algorithms used for HRT denoising in Holter recordings.

5.2   Heart Rate Turbulence Denoising

5.2.1   Support Vector Machine Denoising Algorithm

The signal model considered here uses the RR intervals from an ECG or EGM recording. A VPC has happened at discrete time instant $n = -1$, which is then followed by a compensatory pause at $n = 0$, so that the following RR intervals (from $n = 1$ to $n = 20$) represent the VPC-tachogram under study. Assume that the observed VPC-tachogram is given by $\{y_n, n = 1, \ldots, 20\}$ contains two contributions: one is the actual HRT as the metabolic response to the VPC perturbation, given by $\{x_n, n = 1, \ldots, 20\}$, and the other one consists of noise contributions from different sources, and is given by $\{e_n, n = $

$1, \ldots, 20\}$. The HRT model is then:

$$y_n = x_n + e_n \tag{5.1}$$

for $n = 1, \ldots, 20$. A first approach for denoising $\{y_n\}$ and obtaining an estimate of HRT, denoted by $\{\hat{x}_n\}$, is to use linear filtering. For instance, a Qth order moving-average filter can be used, which will be given by the following signal model:

$$\hat{x}_n = \sum_{q=1}^{Q} b_q y_{n-q+1} \tag{5.2}$$

where b_q are fixed as the coefficients for an adequate filter in the frequency domain. Independently of the kind of filter used, this denoising scheme relies on the assumption of HRT being a band-limited process. Alternatively, a Qth median filter can be used, given by:

$$\hat{x}_n = median\{y_{n-\lfloor\frac{Q}{2}\rfloor}, \ldots, y_{n+\lceil\frac{Q}{2}\rceil}\} \tag{5.3}$$

where $\lfloor\cdot\rfloor$ and $\lceil\cdot\rceil$ denote the rounding up and down to zero, respectively. This denoising scheme is known to be more appropriated whenever impulse noise can be present.

Note that these basic filtering schemes rely on the distribution of noise being known to some extent, which is an *a priori* information that we do not have yet. According to this fact, it is proposed to use a SVM modeling approach. The SVM regressor can be seen as a nonparametric procedure, in the sense that it does not rely on any specified form of the HRT. Also, it is proposed to consider the ε-Huber cost [105], which represents a cost function that can adapt itself to the noise distribution. Finally, given that the extremely short VPC-tachogram signal can not be split into a training and a validation subset, it is proposed to use nonparametric bootstrap resampling, which has been previously used in SVM classifiers for the same purpose of previously tuning of the SVM free parameters [116].

The SVM model for HRT denoising can be described as follows. The nonlinear regression model is given by:

$$y_n = x_n + e_n = \langle \boldsymbol{w}, \phi(n) \rangle + b + e_n \tag{5.4}$$

where $\phi(n)$ is a nonlinear application of n to a possibly high-dimensional (say P-dimensional) feature space $\mathfrak{F}$, where a linear approximation is built by the dot product with vector $\boldsymbol{w} \in \mathfrak{F}$. This model can be seen as a nonlinear interpolation. Following the conventional SVM methodology, a regularized cost function of the residuals is to be minimized. In [105], the following robust cost function of the residuals was proposed:

$$L(e_n) = \begin{cases} 0, & |e_n| \leq \varepsilon \\ \frac{1}{2\delta}(|e_n| - \varepsilon)^2, & \varepsilon \leq |e_n| \leq e_C \\ C(|e_n| - \varepsilon) - \frac{1}{2}\delta C^2, & |e_n| \geq e_C \end{cases} \tag{5.5}$$

where $e_C = \varepsilon + \delta C$; ε is the insensitive parameter, and δ and C control the trade-off between the regularization and the losses. The ε-insensitive zone ignores errors lower than ε; the quadratic cost zone uses the L_2-norm of errors, which is appropriate for Gaussian noise; and the linear cost zone controls the effect of outliers. The SVM coefficients are estimated by minimizing the previous loss function regularized with the squared norm of model coefficients:

$$\frac{1}{2}\sum_{p=1}^{P} w_p^2 + \frac{1}{2\delta}\sum_{n\in I_1}(\xi_n^2 + \xi_n^{\star 2}) + C\sum_{n\in I_2}(\xi_n + \xi_n^\star) - \sum_{n\in I_2}\frac{\delta C^2}{2} \qquad (5.6)$$

with respect to w_p, $\{\xi_n^{(\star)}\}$ (notation for both $\{\xi_n\}$ and $\{\xi_n^\star\}$), and b, and constrained to:

$$y_n - \langle \boldsymbol{w}, \phi(n)\rangle - b \ \leq \ \varepsilon + \xi_n \qquad (5.7)$$
$$-y_n + \langle \boldsymbol{w}, \phi(n)\rangle + b \ \leq \ \varepsilon + \xi_n^\star \qquad (5.8)$$
$$\xi_n, \xi_n^\star \ \geq \ 0 \qquad (5.9)$$

for $n = 1, \cdots, 20$; $\{\xi_n^{(\star)}\}$ are *slack variables* or *losses*, which are introduced to handle the residuals according to the robust cost function; and I_1, I_2 are the sets of samples for which losses have a quadratic or a linear cost, respectively.

Similar derivations of the dual functional can be found in the literature [98, 105]. In brief, by including linear constraints (5.7)-(5.9) into (5.6), the primal-dual functional (or Lagrange functional) is obtained:

$$L_{PD} = \frac{1}{2}\sum_{p=1}^{P} w_p^2 + \frac{1}{2\delta}\sum_{n\in I_1}(\xi_n^2 + \xi_n^{\star 2}) + C\sum_{n\in I_2}(\xi_n + \xi_n^\star) -$$
$$- \sum_{n\in I_2}\frac{\delta C^2}{2} - \sum_{n=1}^{20}(\beta_n\xi_n + \beta_n^\star\xi_n^\star) - \varepsilon\sum_{n=1}^{20}(\alpha_n + \alpha_n^\star) + \qquad (5.10)$$
$$+ \sum_{n=1}^{20}(\alpha_n - \alpha_n^\star)(y_n - \langle \boldsymbol{w}, \phi(n)\rangle - b - \xi_n)$$

constrained to $\alpha_n^{(\star)}, \beta_n^{(\star)}, \xi_n^{(\star)} \geq 0$. By making zero the gradient of L_{PD} with respect to the primal variables [105], it is obtained $\alpha_n^{(\star)} = \frac{1}{\delta}\xi_n^{(\star)}(n \in I_1)$, $\alpha_n^{(\star)} = C - \beta_n^{(\star)}(n \in I_2)$, to be fulfilled, and if these constrains are included into (5.10), primal variables can be removed. The correlation matrix of input space vectors can be identified, and denoted as $\boldsymbol{R}(s,t) \equiv \langle \phi(s), \phi(t)\rangle$. The dual problem can now be obtained and expressed in matrix form, and it corresponds to the maximization of:

$$-\frac{1}{2}(\boldsymbol{\alpha} - \boldsymbol{\alpha}^\star)^T[\boldsymbol{R} + \delta\mathbf{I}](\boldsymbol{\alpha} - \boldsymbol{\alpha}^\star) + (\boldsymbol{\alpha} - \boldsymbol{\alpha}^\star)^T\boldsymbol{y} - \varepsilon\mathbf{1}^T(\boldsymbol{\alpha} + \boldsymbol{\alpha}^\star) \qquad (5.11)$$

constrained to $C \geq \alpha_n^{(\star)} \geq 0$, where $\boldsymbol{\alpha}^{(\star)} = [\alpha_1^{(\star)}, \cdots, \alpha_{20}^{(\star)}]^T$; $\boldsymbol{y} = [y_1, y_2, \ldots, y_{20}]^T$; and $\mathbf{1}$ denotes a column vector of ones. After obtaining Lagrange multipliers

$\boldsymbol{\alpha}^{(\star)}$, the time series model for a sample at time instant m is:

$$\hat{x}_m = \sum_{n=1}^{20} (\alpha_n - \alpha_n^\star) \langle \phi(n), \phi(m) \rangle + b \qquad (5.12)$$

which is a weighted function of the nonlinearly observed times in the feature space. Note that only a reduced subset of the Lagrange multipliers is nonzero, which are called the *support vectors*, and the HRT solution is built in terms of them.

A Mercer's kernel is a bivariate function that is equivalent to calculate a dot product in a possibly infinite dimensional feature space [97]. Examples of valid Mercer's kernels are the *linear kernel*, given by $K(s,t) = \langle s, t \rangle$, and the (nonlinear) *Gaussian kernel*, given by:

$$K_G(s,t) = \exp\left(-\frac{(s-t)^2}{2\sigma^2}\right) \qquad (5.13)$$

where σ is the width of the Gaussian kernel, and it must be properly chosen. For a fixed value of σ, it is fulfilled that $K_G(s,t) = \langle \phi(s), \phi(t) \rangle$ in some unknown feature space. However, it is not needed to know explicitly neither the feature space nor the nonlinear application, but still the dot products in the feature space can be readily calculated by means of the kernel. Thus, the final solution of SVM for HRT denoising can be expressed simply as:

$$\hat{x}_m = \sum_{n=1}^{20} (\alpha_n - \alpha_n^\star) K_G(n,m) + b \qquad (5.14)$$

which is just a linear combination of shifted Gaussian kernels of a given width.

5.2.2   Bootstrap Tuning of the Free Parameters

Note that several free parameters need to be previously tuned in the described SVM denoising algorithm, namely, width σ of the Gaussian kernel, and the free parameters of the cost function (ε, δ, C). Cross-validation techniques are often used for this purpose in SVM approaches, but in our case only 20 observations are available, and splitting them involves dramatically reducing the amount of information in the training set. Search using bootstrap resampling techniques is proposed for finding the bootstrap bias-corrected error as a function of each free parameter, and then fixing the free parameters and training a machine with the whole 20-samples set of the VPC-tachogram.

Bootstrap resampling techniques are useful for nonparametric estimation of the *pdf* of statistical magnitudes, even when the observation set is small. A detailed description and discussion on bootstrap resampling can be found in [121]. The procedure used here is described in [116] for SVM classification, its extension to the regression case being straightforward. In

brief, be $\theta = \{\varepsilon, \delta, C\}$ is the set of free parameters of the SVM for time series y_n. The estimated SVM coefficients are $\hat{\boldsymbol{\alpha}} = [\hat{\alpha}_1 - \hat{\alpha}_1^*, \ldots, \hat{\alpha}_{20} - \hat{\alpha}_{20}^*] = s(\{y_n\}, \theta)$, where $s(,)$ denotes the SVM estimation operator. Empirical risk $\hat{R}_{emp} = t(\hat{\boldsymbol{\alpha}}, \{y_n\})$, where $t()$ is the estimation operator, can be defined as the averaged cost in the training set of samples. A *bootstrap resample* is a data subset drawn from the training set by following its empirical distribution, and accordingly, it consists of sampling with replacement the time samples of y_n, this is, $\{y_n^*(b)\} = \{y_1^*, y_2^*, \ldots, y_{20}^*\}$, and the resampling process is repeated for $b = 1, ..., B$ times. Note that, for each resample, $\{y_n^*(b)\}$ contains samples of $\{y_n\}$ appearing none, one, or several times. A partition of $\{y_n\}$ set of samples can be done in terms of resample $y_n^*(b)$, given by $\{y_n\} = \{y_{n,in}^*(b)\} \cup \{y_{n,out}^*(b)\}$, according to the time samples included (in) and excluded (out) in resample b. The SVM coefficients from each resample will be given by $\hat{\boldsymbol{\alpha}}(b) = s(\{y_{n,in}^*(b)\}, \theta)$.

An acceptable approximation to the actual risk (i.e., not only empirical, but total risk) can be obtained using $\hat{R}_{act} = t(\hat{\boldsymbol{\alpha}}(b), \{y_{n,out}^*(b)\})$. A bias-corrected estimate of the actual risk is obtained by simply taking the replication average. Furthermore, this average estimate can be achieved for a grid of values of the SVM free parameters, hence allowing us to determine their suitable values to train the SVM with the whole training set. A good range for B is typically 200 to 500 resamples. SVM free parameters are not usually mutually independent, however, a good heuristic approach is to start with an intermediate value of C, γ, set $\varepsilon = 0$, then giving an initial guess of the kernel parameter, and then re-estimate again each the other parameters, continuing until a stable set of parameters is obtained.

5.3   Experiments

Practical issues for the application of the proposed HRT denoising techniques were studied and are next presented, first by analyzing the suitability of bootstrap resampling for tuning the free parameters in SVM interpolation algorithm. Then, the clinical EPS database that was used as gold standard for HRT measurements is described, and application examples of denoising are used in order to show the following points: (1) pacing-induced HRT during EPS can be considered as almost noise-free recordings; (2) The cycle length previous to the HRT onset can be physiologically related to the HRT oscillation amplitude, which should be taken into account when measuring TS parameter; And (3) the spectral domain representation of HRT can yield the shape of the denoised gold standard HRT. Next, measurements on TS parameter are studied in the gold standard EPS patient database. After summarizing the clinical data of Holter database, denoising examples are considered both in the time and in the frequency domains, and poblational measurements of TS are studied in this setting. Finally, denoising methods are statistically compared in terms of a new parameter, the Turbulence Length, which allows us to quantitatively determine the effectiveness of the
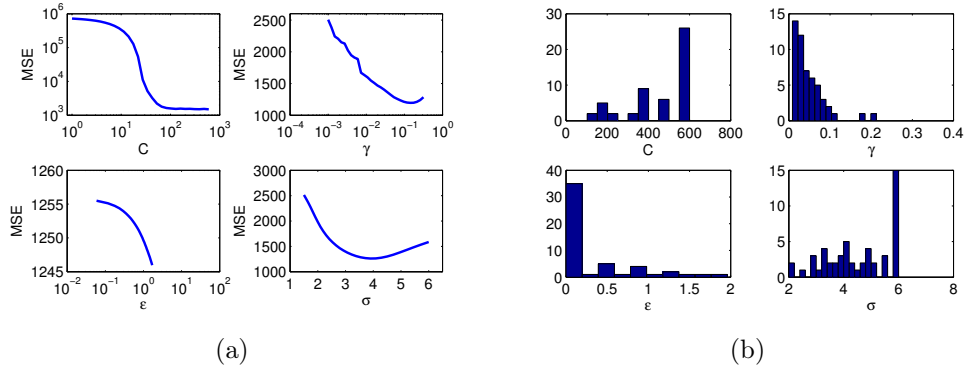
Figure 5.1: *Example of free parameters selection for the SVM denoising algorithm. (a) Bootstrap estimated MSE in a single VPC-tachogram example. Each free parameter is subsequently explored in a rank of possible values while fixing the other ones. (b) Histograms of the obtained values of the free parameters for a set of VPC-tachogram in a single patient. Note the trend of γ and ε towards lower values, and of C and σ towards higher values.*

denoising procedures in the time domain.

5.3.1 Support Vector Machine Free Parameter Selection

One of the key issues when using SVM algorithms is setting appropriate values for the free parameters. In this problem, where only 20 discrete-time samples are available, bootstrap resampling was used for this purpose. For each VPC-tachogram, the Mean Squared Error (MSE) was estimated with Bootstrap resampling on the time series for each tested combination of SVM free parameters (C, γ, ε, and σ). Bootstrapped MSE (200 resamplings) was obtained for values of each free parameter in its search interval, while freezing the other parameters, using a sequential search and with two rounds. Figure 5.1(a) shows an example of the bootstrapped MSE for searching the free parameters in a VPC-tachogram of a patient, and panel (b) depicts the histograms of the free parameters obtained for all the VPC-tachogram in the same patient. An appropriate rank of searched values was set by reviewing the histograms in a subset of the EPS and Holter database, which was found to be $\gamma \in (10^{-3}, 0.32)$, $C \in (1, 600)$ and $\sigma \in (1.5, 6)$ (on a logarithmic scale), and ε between 0 and the standard deviation of the signal divided by 10 (on a linear scale). These ranks were found to be appropriate for individually tuning in each VPC-tachogram the SVM interpolator throughout the study.

5.3.2 Electrophysiological Study Patient Database

VPC-tachograms were induced by pacing in 10 patients with structurally normal heart during EPS under mild sedation at rest and were used as the HRT gold standard by assuming that under these conditions the electrophys-

(a)

(b)

(c)

(d)
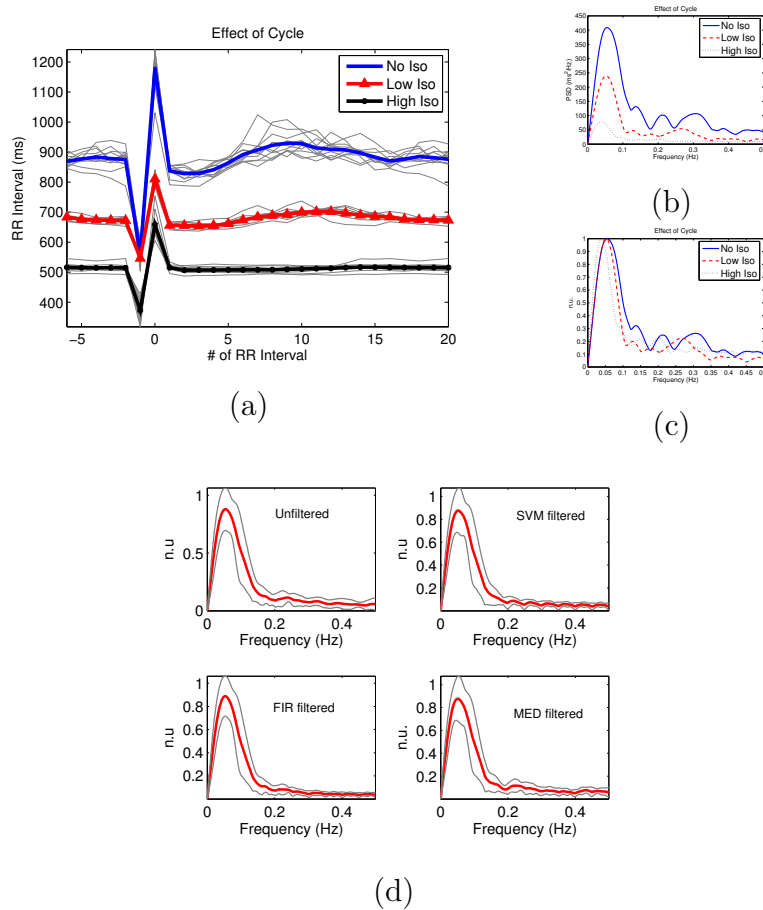
Figure 5.2: *EPS database: Relationship with preceding cycle length. (a) VPC-tachograms for basal and for low and high isoproterenol dose controling the heart rate. (b) Effect of cycle in frequency domain. (c) Effect of cycle in frequency domain, with normalized units. (d) Normalized spectra for a patient (mean and 95% CI), for raw and denoised VPC-tachogram.*

iological noise would be minimized. The VPCs were induced by cyclic pacing from the right ventricular apex, after every twenty one spontaneous beats during sinus rhythm, according to the procedure suggested in [119]. The intracardiac EGM and the surface ECG were simultaneously recorded on a conventional digital polygraph and the beat-to-beat intervals were extracted from the ECG.

Figure 5.3 shows an example of denoising a VPC-tachogram in a patient from EPS database. A clear smoothing effect can be observed, and the turbulence oscillation pattern (this is, initial acceleration followed by a deceleration) is clearly recovered with the three methods, i.e., SVM, linear (FIR), and median (MED) filtering. According to its proposal as gold standard, low noise level is expected in these signals, and hence, they hardly differ from the denoised version with any of the proposed algorithms. This can be also checked in the frequency domain representation of the HRT. The spectrum using a Fast Fourier Transform (FFT) of 512 samples was obtained
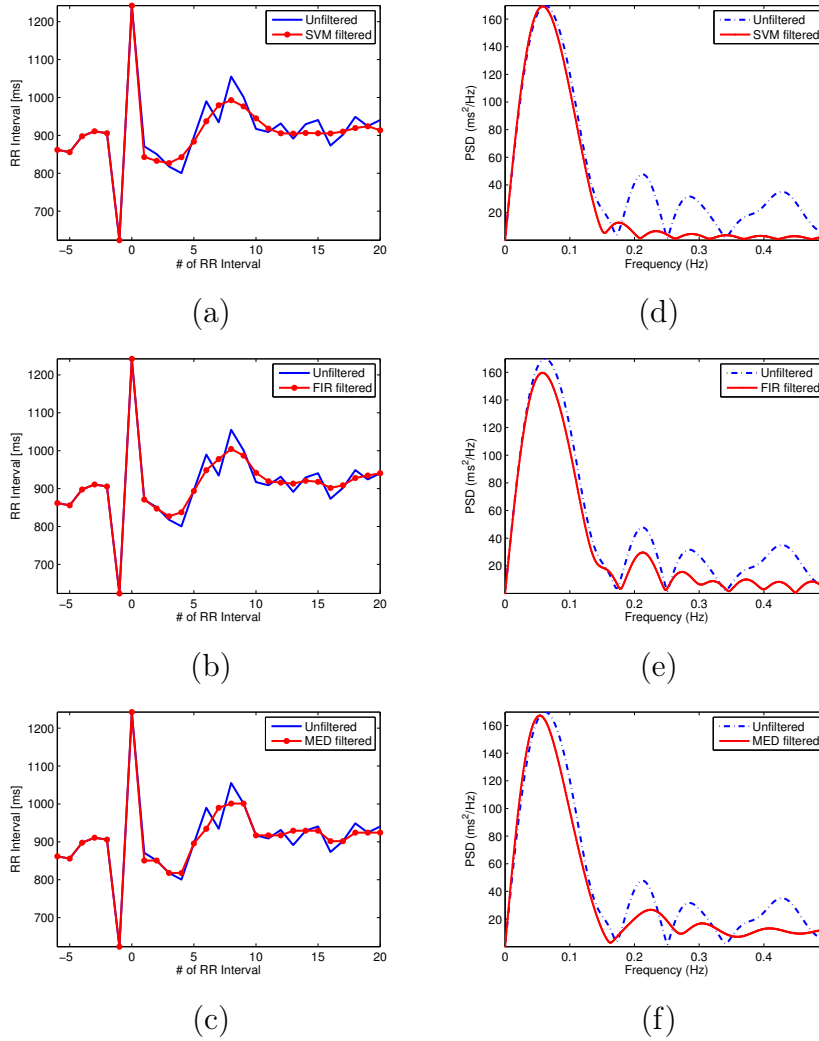
Figure 5.3: *EPS database: Examples of HRT denoising, in time (left) and frequency (right) domains. (a,d) SVM filtered. (b,e) FIR filtered. (c,f) Median filtered.*

for the VPC-tachogram recording. Note the extremely low length of the HRT time series (20 samples), which makes a strong windowing effect to be present. Figure 5.3 also shows the power spectral density for denoised VPC-tachograms. It can be seen that the power in low frequency (about < 0.18 Hz) is maintained in all cases, whereas the high frequency components are filtered and smoothed, aiming to cancel the high frequency noise. The SVM denoised signal has a slightly lower level in the high frequency band (about > 0.18 Hz) and a less distorted low frequency band, when compared to the spectrum of the other denoising methods.

The relationship with previous cycle length was observed in the gold standard HRT. Figure 5.2 shows an example of the effect of the preceding cycle in a patient with three different conditions: basal, low, and high doses of isoproterenol, yielding different levels of HR acceleration preceding the
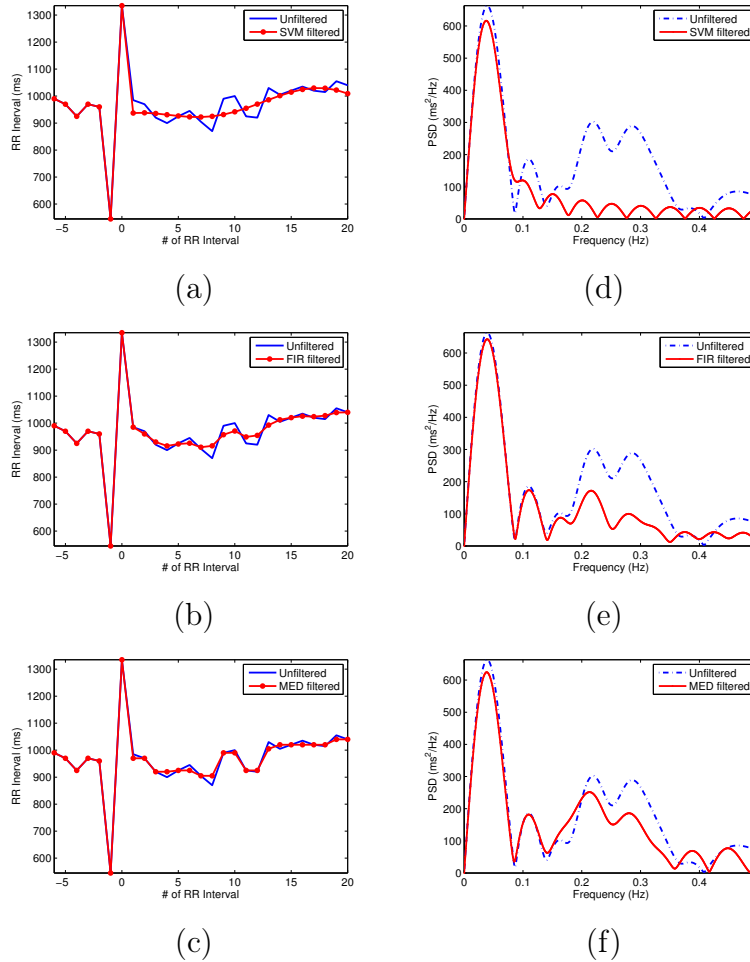
Figure 5.4: *Examples in Holter database, in time (left) and frequency (right) domains: (a,d) SVM denoised; (b,e) FIR denoised; (c,f) Median denoised.*

HRT. In order to clearly observe the relationship between the HR and the HRT, a number between 9 and 11 VPC were stimulated for each of these states. Figure 5.2(a) shows the relationship between preceding HR and HRT oscillation amplitude in the time domain. According to previously reported results in the literature [112], the increase in HR is related to a decrease in the turbulence oscillation amplitude. Figure 5.2(b) shows the same effect in the frequency domain, in which the spectral envelope clearly decreases with cycle length. Note also that there is a slight, yet visible, shift in the power towards lower bands. Figure 5.2(c) shows the normalized spectra, in which the shift is still more patent. Accordingly, filtering the averaged VPC-tachogram, while being adequate for noise reduction, may mask the potential changes of the VPC-tachogram response over time, thus precluding to assess oscillations of the autonomic balance in an individual patient. Figure 5.2(d) shows the averaged spectrum and 95% confidence intervals for normalized spectrum in a patient of EPS database, for raw and denoised signals. Spectra of each VPC-tachogram have been separately normalized, and average and
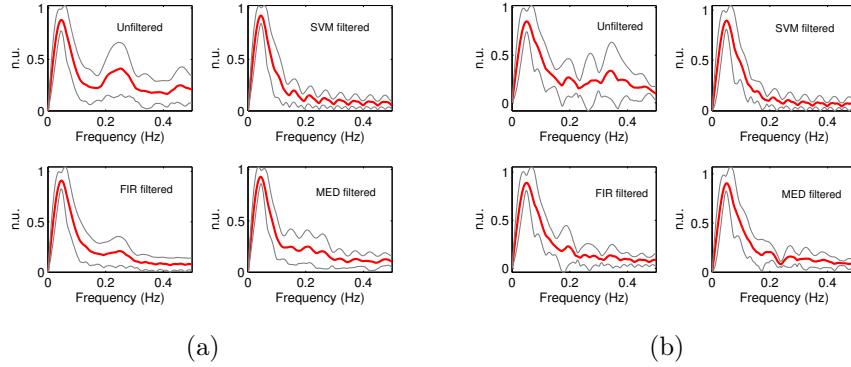
Figure 5.5: *Examples from Holter database in the frequency domain. Averaged normalized spectra and 95% confidence intervals for two patients with 24 VPC-tachogram (a) and 8 VPC-tachogram (b) in their 24-hours Holter recordings.*

standard deviation have been subsequently calculated.

Note that filtering does not change significantly the spectral content of the turbulence in physiological rest with any of the denoising methods, which allows us to consider pacing induced HRT during EPS as a gold standard for comparison with the denoising algorithms in the Holter database.

5.3.3 Results on the Electrophysiological Study Patient Database

Table 5.1 shows the number of VPC (VPC-tachogram) obtained for each patient in the EPS database, together with the mean and standard deviation of the TS parameter in each VPC-tachogram ($TS_{VPC-tach}$), both for unfiltered and for filtered conditions. Right columns in the table present the values of the TS parameter for each patient, and for each denoising algorithm (SVM TS, FIR TS, $Median$ TS), as well as for the raw signal. Parameter TS was here obtained according to the conventional procedure, i.e., by calculating the TS for the averaged VPC-tachogram signals. It can be seen that parameter TS has lower values when obtained from the averaged template than when averaged in each VPC-tachogram. Nevertheless, in both cases the TS has similar values (yet slightly lower for the denoised VPC-tachograms) for all the denoising methods.

5.3.4 Holter Database

VPC-tachograms were also obtained in 61 post-myocardial infarction patients included in a prospective study at Hospital Universitario Virgen de la Arrixaca (Murcia, Spain) [122]. A 24-hour ambulatory electrocardiographic monitoring was performed in patients with stable sinus rhythm between 2 and 6 weeks after infarction and 61 with at least 1 VPC during the monitoring period were included in the analysis (age 64.3 +/- 9.0 years, 26 men).

# Pat	# VPC	$TS_{VPC-tach}$	SVM $TS_{VPC-tach}$	FIR $TS_{VPC-tach}$	Median $TS_{VPC-tach}$	TS	SVM TS	FIR TS	Median TS
Pat1	9	34.7 ± 10.9	33.2 ± 11.9	28.6 ± 9.7	30.3 ± 12.8	30.2	29.5	25.3	28.1
Pat2	11	24.6 ± 7.8	22.7 ± 7.1	21.9 ± 7.3	23.6 ± 7.9	19.7	18.4	18.6	20.1
Pat3	10	61.1 ± 27.9	51.2 ± 26.7	46.4 ± 22.3	48.7 ± 26.8	52.7	41.7	40.2	40.0
Pat4	9	38.7 ± 27.7	30.8 ± 24.2	30.3 ± 22.4	29.4 ± 21.2	17.6	15.0	14.0	15.5
Pat5	11	47.0 ± 13.3	33.5 ± 10.6	36.5 ± 9.4	37.3 ± 10.6	41.6	30.9	35.2	35.2
Pat6	8	13.0 ± 4.2	10.2 ± 5.1	9.9 ± 3.5	10.9 ± 4.8	7.8	6.6	6.6	6.6
Pat7	11	24.6 ± 10.1	19.0 ± 7.2	20.7 ± 8.0	22.0 ± 9.0	20.6	16.8	18.9	19.8
Pat8	12	24.1 ± 15.5	18.5 ± 14.1	19.5 ± 14.2	21.3 ± 16.7	14.3	11.0	12.2	13.9
Pat9	14	33.8 ± 15.2	28.8 ± 11.3	28.8 ± 12.3	31.0 ± 13.1	28.0	24.4	24.4	25.6
Pat10	19	8.6 ± 2.9	7.6 ± 3.0	7.4 ± 2.7	7.9 ± 3.1	6.3	5.9	5.7	6.0

Table 5.1: *EPS Database Results: Number of VPC per patient, TS parameter for each patient and each VPC-tachogram, $TS_{VPC-tach}$, (mean $\pm$ standard deviation), and TS parameter from averaged VPC-tachogram after denoising.*

	Mean±Std	Median	[Max,Min]
# VPC-tachogram	50.7 ± 104.8	12	$[474, 1]$
TS	7.8 ± 6.0	6.1	$[29.1, 0.4]$
SVM TS	6.9 ± 4.4	6.1	$[20.3, 0.4]$
FIR TS	6.8 ± 6.3	5.2	$[37.3, 0.2]$
Median TS	6.8 ± 6.3	5.2	$[37.3, 0.2]$
$TS_{VPC-tach}$	14.7 ± 9.8	12.1	$[174.0, 0]$
SVM $TS_{VPC-tach}$	11.3 ± 6.0	10.6	$[145.4, 0.02]$
FIR $TS_{VPC-tach}$	11.9 ± 8.3	9.6	$[146.1, 0.002]$
Median $TS_{VPC-tach}$	13.2 ± 10.0	10.7	$[171.5, 0]$

Table 5.2: *Holter Database: Number of VPC-tachogram per patient and values for the TS parameter (raw and denoised). Conventionally calculated and averaged values for individual TS from denoised HRT ($TS_{VPC-tach}$) are reported.*

The average number of VPC-tachograms per patient was 50.7 (median 12, rank 1-474).

Figure 5.4 shows a denoising example in one of these patients. It can be seen that SVM obtains a denoised signal with a clearer turbulence pattern in the time domain in comparison with the other two filtering methods. With respect to the frequency domain, SVM is better than the other denoising methods at cancelling the noisy components in high frequency, while preserving an spectral shape that is quite similar to the previously observed in the gold standard. Averaged normalized spectra and 95% confidence intervals with all the methods are shown in Figure 5.5, in two patients with moderate and low (24 and 8) number of VPC-tachograms in the 24-hour recording. The unfiltered spectra show an extremely high noise level that is partially reduced by the median and FIR algorithms. However, the narrower confidence interval and shape coherence with the gold standard spectra is obtained with the SVM denoising.

5.3.5 Results on the Holter Database

Table 5.2 shows the number of VPC-tachograms in the Holter database. Also, the values of TS parameter when obtained from conventional processing for both raw and denoised signals were compared with its calculation from each isolated VPC-tachogram ($TS_{VPC-tach}$) in all cases. As expected, higher TS values were obtained for isolated and denoised VPC-tachogram, and in both procedures, SVM denoised values yielded the lowest standard deviation.

An additional parameter was calculated, aiming to quantify the similar-
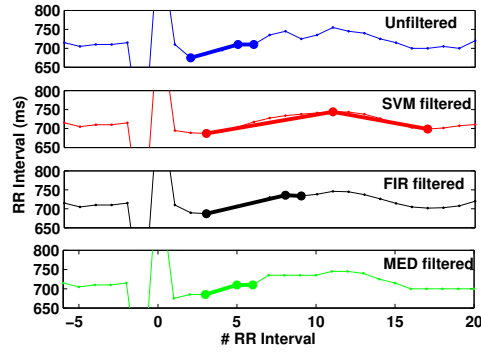
(a)
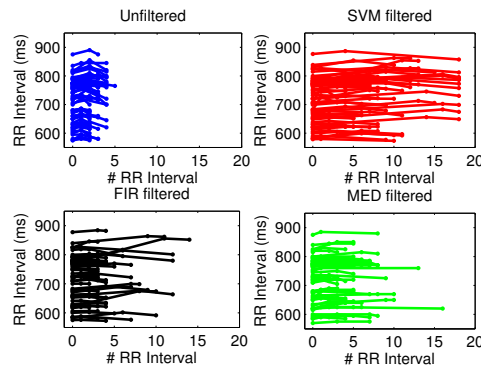
(b)

Figure 5.6: *Holter Database: Examples of Turbulence Length calculation. (a) When Turbulence Length is measured in a single VPC-tachogram, larger values correspond to a clearer correspondence with the oscillation expected by the HRT mechanism, whereas shorter values are in general due to noise still present in the signal. (b) Example of Turbulence Lengths in a patient with high number of VPC-tachogram, and effect of the denoising algorithms.*

	Tach.	SVM	FIR	Med.
EPS	5.2±1.7	10.9±3.0*	9.7±2.5*	7.2±2.4*
Holter	3.0±0.7	11.2±2.6*	7.6±2.7*	5.3±1.6*

Table 5.3: *EPS and Holter Databases: Turbulence Lengths for the patients in the study and for the denoising algorithms.*

ity in the time domain between the (raw or denoised) actual VPC-tachogram and the expected according to the physiological definition of HRT. Therefore, for each VPC-tachogram the following sequence was obtained: first minimum, first maximum, and second minimum, for the raw and for the filtered VPC-tachogram. This sequence gives a measurement of the similarity between the turbulence waveform and the postulated mechanism in the HRT definition (deceleration, acceleration, and oscillation). The Turbulence Length parameter was calculated as the difference between the discrete times corresponding to the second and to the first minimum, and hence it has units

of number of beats.

Figure 5.6 shows an example in a patient with a high number of VPC-tachogram, and it can be observed therein that the Turbulence Length is extremely short in raw VPC-tachogram, because the first and second relative minima usually correspond to the noise present in the signal. An increase in the Turbulence length can be obtained for denoising VPC-tachogram, which is more visible with the SVM denoising. Table 5.3 shows the values of the Turbulence Length both in the gold standard and in the Holter databases, in which a significant increase can be observed (*p<0.001 when compared with unfiltered tachograms, paired t-Student test).

5.4 Conclusions

A new signal processing method, the SVM interpolation, has been proposed for denoising PPT signals in HRT. The use of a gold standard database with pacing induced VPC-tachogram during EPS has been used for comparison of the HRT behavior both in the time and in the spectral domains. In low-noise conditions, the SVM algorithm yielded results that were similar to other conventional filtering methods, and in all cases the results were according to the expected mechanism of the HRT. For VPC-tachograms in this EPS database, denoising algorithms also were shown to yield similar spectral profiles of HRT. In the presence of noise, i.e., in the Holter database, the tested algorithms yielded denoised VPC-tachogram signals containing lower noise level. However, SVM algorithm obtained a higher performance when compared to the median and to the FIR filters. As seen in the examples, the oscillations that are expected in the HRT were better preserved, the spectral profile of the denoised VPC-tachogram was more similar to the observed in the gold standard, standard deviation was lower, and the significantly higher values of Turbulence Length suggest that the noise was more efficiently removed from the turbulence.

The proposed SVM algorithm allows to perform the HRT analysis even when a low number of VPCs are available. This characteristic has clinical implications, because one of the current requirements for suitability of a patient to be studied in terms of TS is a sufficient number of VPCs being available. Thus, HRT denoising will help to extend the HRT analysis to a higher number of patients. The SVM algorithm gives a better description of the dependence with the HR previous to the VPC-tachogram, and allows the analysis of the changes of HRT with time. These possibilities should be explored in additional studies with other databases of patients with different cardiac diseases.

We can conclude that it is possible to obtain time-local HRT measurements without averaging, by using robust digital signal processing, as shown by the analysis on the EPS database. The SVM denoising allows us to measure the HRT in noisy conditions, such as in patients with Holter, which is a usual situation in the clinical practice. Finally, this denoising can give new

approaches to HRT analysis, such as evaluation of the changes of HRT with time, or the evaluation of patients with a low number of VPC. Hence, the application of SVM denoising in series with clinical events could improve the predictive value of the classical HRT methods for risk stratification. Finally, other similar problems can be found in Electroencephalography literature, like event-related potentials [123, 124], which could be addressed by following the approach used here to HRT denoising.

Chapter 6

Influence of Coupling Interval and Heart Rate on Heart Rate Turbulence

6.1 Introduction

The baroreflex hypothesis for the HRT origin would imply that the more premature the VPC (the less hemodynamically efficient the contraction), the stronger the HRT response [6]. Nevertheless, a number of precedent works studying the relationship between CI and HRT present conflicting results, as summarized in Section 6.2.

The usual procedure to assess the HRT implies averaging all the available isolated VPC-tachograms in order to construct the average VPC-tachogram, on which TS and TO are computed. This averaging aims to improve the SNR, and it has provided positive results in several clinical studies [5, 48, 125]. However, it could mask the influence of different physiological factors on the HRT, and more, if these factors are not independent, then averaging could be a biased or inaccurate processing stage for HRT parameter estimation.

The aim of this chapter is to propose a procedure to systematically assess the interaction between VPC prematurity (as given by its coupling interval, CI) and the underlying HR on the HRT. Instead of conventional averaging, HRT was measured by computing TS parameter on each individual VPC-tachogram and comparing it with the corresponding CI and HR physiological values.

For this purpose, a population of patients with structurally normal heart undergoing EPS was considered in the present Thesis. A clinical protocol was designed so that CI was controlled with a programmed cardiac pacing protocol, and HR was controlled by using isoproterenol. The EPS protocol consisted of two substudies, one to analyze the relationship between HR and HRT, and another to analyze the combined effect of HR and CI on HRT. These interactions were also studied by using Holter recordings from patients after an AMI episode, in order to compare data registered in low physiological

noise conditions (EPS) with those in real-world conditions (Holter out-of-hospital monitoring).

Several data analysis methods have been used to determine the cross-effect and interactions of CI and HR on TS parameter, namely:

1. Simple linear regression analysis (HR vs TS, and CI vs TS), on EPS database separated into HR and CI controlled patients, respectively, was used to replicate results in previous studies [119, 126, 127, 128] in our database.

2. Nonlinear ridge regression models fitted on EPS database with all patients altogether, and on AMI database divided into high risk and low risk patients, according to HRT usual thresholds [6]. This methods was used to provide a model that is able to explain the influence of CI and HR on HRT.

6.2   Background

HRT probably reflects the baroreflex activity triggered by the low pulse pressure due to a hemodynamically inefficient ventricular contraction [6]. Several physiological factors modulate and can affect the HRT pattern, namely, the HR, the VPC prematurity (or CI), and circadianity [112, 129, 130]. On the one hand, the dependence of HRT on HR is attributed to a shared sympathovagal modulation, hence the HRT response is attenuated at high HR conditions. Some studies support this physiological hypothesis by showing a strong dependence between HR and HRT across individuals [131, 132], however, only weak correlations have been found within individuals [47].

Authors in [133] found that prematurity of VPC was linearly correlated only with TO, but TS was not affected at all, whereas studies [127] and [134] reported strong linear correlations of both TO and TS with prematurity of VPC. Interestingly, this effect was less pronounced in patients with left ventricular dysfunction [127]. However, authors in [119] found no correlation between HRT parameters and prematurity of VPC, either in pooled population or in individual patients. In summary, existing studies provide us with contradictory results, sometimes even apparently opposed to the HRT physiological hypothesis. Conflicting results among different studies about correlations between HRT parameters and CI have been usually attributed to the effect of basal HR. According to [135] if HR is high then, regardless of CI, HRT will be low and unlikely to be correlated with CI. The author in [135] stated:

> *"The effect of coupling interval as separate from HR seems debatable, and awaits further study."*

There had been some attempts to characterize HRT parameters by using simultaneously the information of CI and HR, by representing TS and TO as a function of CI and HR [128, 136], but no clear pattern could be observed, likely due to the low SNR in Holter monitoring signals.
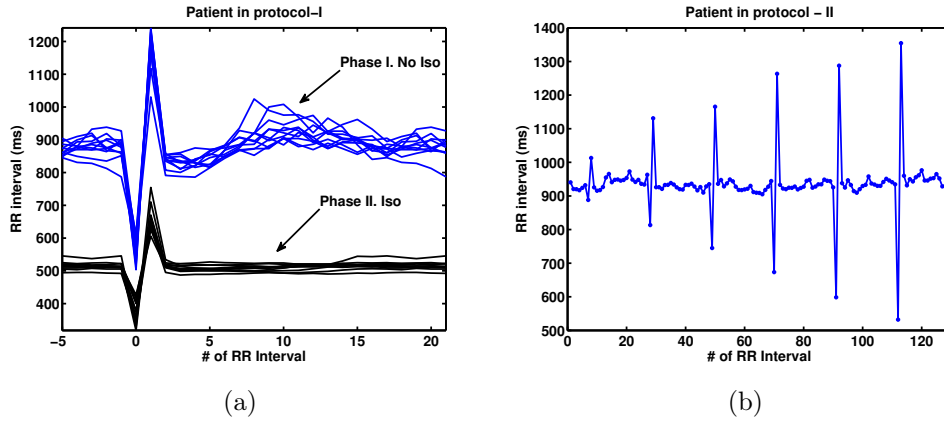
Figure 6.1: *(a) Superposition of individual VPC-tachograms from a patient in Protocol–I. Phase–I (no-isoproterenol) shows high SCL values (low HR), and Phase–II (isoproterenol) shows lower SCL values (high HR). HRT is clearly attenuated at high HR. (b) Example of consecutive VPC-tachograms for a patient in Protocol–II, showing the change of prematurity of the VPC.*

6.3   Clinical Datasets

In this Section, the EPS and AMI databases are described. The protocol to stimulate VPC on EPS patients is explained with detail.

6.3.1   Electrophysiological Studye Database

A database of 11 patients with structurally normal heart referred for EPS in Hospital Universitario Virgen de la Arrixaca (Murcia, Spain) was assembled. A protocol to induce VPC was approved by the local Ethics Committee and all participants granted a signed informed consent. The protocol was performed during SR at the end of the EPS and after ablation procedures. Sequences of 10 single induced VPC were delivered every 20 seconds from the apex of the right ventricle. VPC-tachograms were reviewed to discard those with atrial or ventricular ectopy. The study was structured into two protocols: Protocol–I, designed to study the influence of HR on HRT, with 5 patients, and Protocol–II, designed to study the combined influence of HR and prematurity of VPC (CI) on HRT, with 6 patients. The HR was controlled by isoproterenol, which emulates the general activation of beta-1 receptors in the heart by the sympathetic nervous system [137], whereas the CI was controlled by modifying the prematurity of the VPC. Table 6.1 summarizes the demographic variables of the 11 EPS patients.

Age (mean±std), [min,max] years	Sex (Male/Female)
50.45 ± 15.82 [24, 76]	4/7

Table 6.1: *EPS database demographic variables.*

Protocol–I. Hear Rate Influence on Heart Rate Turbulence

The purpose of this protocol was to assess the influence of HR on the HRT, under the assumption that high HR reduces the HRT response, i.e. produces lower TS values. Protocol–I had two phases. *Phase–I*, in which 10 VPC were delivered without isoproterenol. *Phase–II*, in which 10 VPC were delivered with isoproterenol. HR was high (low Sinus Cycle Length, SCL) in *Phase–II*, due to administration of isoproterenol. Figure 6.1(a) shows individual VPC-tachograms from a patient on Protocol–I. Note that HRT is clearly attenuated at high HR, which corresponds with *Phase–II*.

Protocol–II. Influence of Heart Rate and Coupling Interval on Heart Rate Turbulence

The purpose of this protocol was twofold: (1) to verify that CI modulates the HRT, under the assumption that lower CI (more premature VPC) leads to stronger HRT response; (2) to corroborate that HR moderates or interacts with the CI modulation of the HRT, under the assumption that high HR will affect it. Protocol–II was also structured into two phases: *Phase–I* without isoproterenol and *Phase–II* with isoproterenol. In each phase, 10 VPC were delivered with extraestimuli prematurity starting at 95% of the preceding sinusal RR-Interval, and decreasing prematurity of each extrastimuli by 70 ms. Figure 6.1(b) shows an example for a patient on Protocol–II.

    The design of Protocol–II aimed to decouple the effect of HR and CI on the modulation of HRT, considering two scenarios with HR as constant as possible: one scenario with low HR (*Phase–I*); another one with high HR (*Phase–II*). In both, CI was modified to evaluate the isolated influence of the VPC prematurity.

6.3.2   Acute Myocardial Infarction Database

This database contained 61 AMI patients that underwent emergency coronary angiography, and when appropriate, percutaneous revascularization of the infarct. This data were collected in a prospective study at Hospital Universitario Virgen de la Arrixaca (Murcia, Spain) [122] to evaluate the impact of primary angioplasty on the indication for implantable defibrillator in patients with AMI. A 24-hour Holter was done in patients with stable SR between 2 and 6 weeks after infarction, and 61 patients with at least 1 VPC during the monitoring period were included in the analysis. The average number of VPC-tachograms per patient was 50.7 (median 12, rank 1-474).

    AMI database was split into two different subsets: (1) one subset comprised patients with normal HRT parameters values: $TS \geq 2.5\ ms/RR-interval$ & $TO \leq 0$ %, hereafter called *AMI low-risk*. (2) The another subset comprised patients with abnormal HRT parameters values $TS < 2.5\ ms/RR-interval$ & $TO > 0$ %, hereafter called *AMI high-risk*. TS and TO cutoff values are commonly used in most clinical studies, where $TS > 2.5\ ms/RR-interval$ and $TO < 0$ % are considered normal. They were proposed using data

from different post-infarction studies [6]. Table 6.2 shows the demographic statistics.

	Age (mean±std), [min,max] years	Sex (Male/Female)
AMI low-risk	$62.65 \pm 11.87 \, [34, 82]$	12/5
AMI high-risk	$70.00 \pm \;\; 5.61 \, [62, 77]$	1/4

Table 6.2: *AMI database demographic variables.*

6.4 Simple Linear Regression and Nonlinear Ridge Regession Models

Simple linear regression models were used to assess, independently, the relationship between TS and SCL, and between TS and CI, on EPS database. The goal was to reproduce the analysis in the literature using data from a specifically designed protocol to decouple the effect of HR and CI. Nonlinear ridge regression model was proposed to take into account possible interactions between SCL and CI. Finally, a bootstrap procedure was used to estimate the standard error of the parameters in the nonlinear ridge regression model, which, in turn, allow to estimate confidence intervals and test the significance of the parameters. The advantages of the boostrap procedure are that no assumption about the distribution of the residuals is made and that the estimation of standard error is reasonable even if the assumption of the nonlinear regression model is wrong [138].

Note that in this Chapter, as in most previous works in the literature [119, 132], HR is represented as SCL in milliseconds for calculation purposes.

6.4.1 Simple Linear Regression

Relationship among physiological factors HR and CI with TS was assessed by means of a simple linear regression model driven by data. A regression line is constructed by using LS, hence allowing to measure the correlation between response and explicative variables. This simple analysis would allow to determine whether these physiological variables are related with HRT in the same way as explained by the baroreflex source hypothesis. The following linear regression model was used:

$$TS = w_{C,1} \; CI + w_{C,0} + \varepsilon_C \qquad (6.1)$$

where $w_{C,0}$, and $w_{C,1}$ are the coefficients of the linear model, and ε_C accounts for the model residuals. To isolate the influence of CI from the effect of HR as much as possible, the *normalized coupling interval* (CI_n) was also considered [126], defined as:

$$CI_n = \frac{Coupling \; Interval}{Preceding \; Sinus \; Interval} \qquad (6.2)$$

and the results were compared by using both CI and CI_n as independent variable in (6.1).

Clearly, the slope coefficient $w_{C,1}$ quantifies the attenuation of HRT due to the CI. The statistical significance of this coefficient was evaluated by using F-test and Pearson's correlation coefficient, R.

The influence of HR on HRT was also assessed using a linear regression model given by:

$$TS = w_{H,1}\ SCL + w_{H,0} + \varepsilon_H \tag{6.3}$$

where $w_{H,0}$, and $w_{H,1}$ are the model coefficients, and ε_H accounts for the residuals.

6.4.2   Nonlinear Ridge Regression Model

Given that conflicting results in the literature could be due to possible nonlinear relationships among physiological variables and the HRT, an extension of the previous models was proposed by including nonlinear transformations of explicative variables and an interaction term. Regularization was used to avoid overfitting.

Accordingly, the nonlinear regression model assumes that TS parameter could be a nonlinear function of the SCL and CI: $\widehat{TS} = f(SCL, CI)$. It can be stated as follows:

$$\widehat{TS} = w_0 + w_1 SCL + w_2 CI + w_3 SCL^2 + w_4 SCL^3$$
$$+ w_5 CI^2 + w_6 CI^3 + w_7 SCL \cdot CI \tag{6.4}$$

where independent variables can be arranged in a vector $\boldsymbol{\varphi}$ as:

$$\boldsymbol{\varphi} = \begin{bmatrix} 1 \\ SCL \\ CI \\ SCL^2 \\ SCL^3 \\ CI^2 \\ CI^3 \\ SCL \cdot CI \end{bmatrix} \tag{6.5}$$

and they allow nonlinear transformation of SCL and CI. Terms have been included up to the third degree of both SCL and CI, together with an interaction term to characterize interaction effects. The corresponding model coefficients are arranged in $\boldsymbol{w}$, such that the linear regression model can be formulated as:

$$TS_i = \boldsymbol{w}^T \boldsymbol{\varphi}_i + \varepsilon_i; \text{ for } i = 1, \dots, N \tag{6.6}$$

where N is the total number of individual tachograms. In matrix notation, previous equation can be rewritten as:

$$\boldsymbol{TS} = \boldsymbol{\Phi} \boldsymbol{w} + \boldsymbol{\varepsilon} \tag{6.7}$$
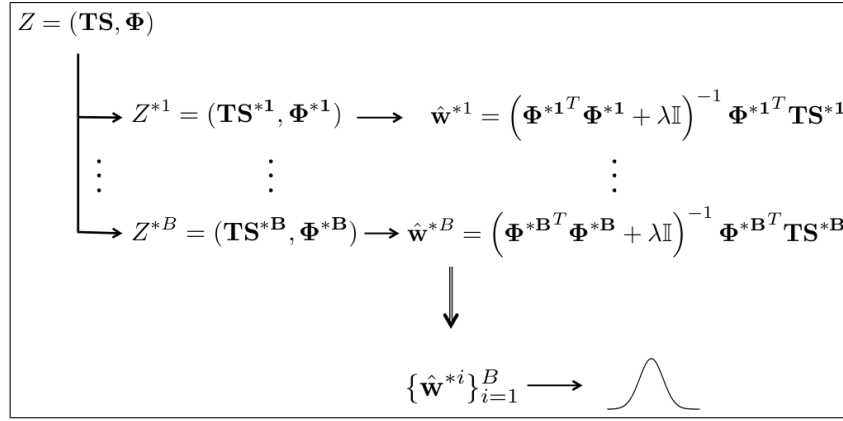
Figure 6.2: Bootstrap procedure to estimate distribution of weights

where $\boldsymbol{\Phi}$ is the physiological matrix, defined as follows:

$$\boldsymbol{\Phi} = \begin{bmatrix} - \boldsymbol{\varphi}_1^T - \\ - \boldsymbol{\varphi}_2^T - \\ \vdots \\ - \boldsymbol{\varphi}_N^T - \end{bmatrix} \tag{6.8}$$

To compute $\boldsymbol{w}$, the MSE cost function is minimized. Additionally, the original cost function is modified to include a penalty term (regularization) depending on the model coefficients. The objective of the regularization term is to find a trade-off between a smooth solution at the same time providing low error [139, 140]. The influence of the regularization term is controlled by regularization parameter λ, so that the modified MSE cost function is:

$$\min_{\boldsymbol{w}} \ \left\| \boldsymbol{TS} - \boldsymbol{\Phi}\boldsymbol{w} \right\|_2^2 + \lambda \left\| \boldsymbol{w} \right\|_2^2 \tag{6.9}$$

Thus, the solution is given by:

$$\boldsymbol{w} = \left(\boldsymbol{\Phi}^T \boldsymbol{\Phi} + \lambda \mathbb{I} \right)^{-1} \boldsymbol{\Phi}^T \boldsymbol{TS} \tag{6.10}$$

6.4.3 Model Performance Evaluation and Bootstrap for Characterization of Variable Relevance

In order to estimate the accuracy of the nonlinear regression model, the MSE and the R^2 statistic were computed using cross-validation. In this approach, a fair evaluation of both quantities is obtained using data different from those used to construct the model. The quantity MSE is defined, here, as:

$$MSE = \frac{1}{N} \sum_{i=1}^{N} (\widehat{TS}_i - TS_i)^2 \tag{6.11}$$

and R^2 defined as:

$$R^2 = 1 - \frac{RSS}{TSS} \qquad (6.12)$$

where $RSS = N \cdot MSE$ is the Residual Sum of Squares, and TSS, Total Sum of Squares, is defined as:

$$TSS = \sum_{i=1}^{N} (TS_i - \overline{TS})^2 \qquad (6.13)$$

where $\overline{TS}$ is the average of all TS_i values. R^2 measures the proportion of variability in the response variable that can be explained by the explanatory variables.

A 10-fold cross-validation procedure typically used in the literature was used [141]. In this procedure, the dataset is randomly divided into 10 groups of equal size named folds, and 10 nonlinear regression models are constructed. Each model is constructed using data from 9-folds, while remaining fold is used as a validation set to compute accuracy measures. This process is repeated 10 times, so that the validation set correspond to a different fold every time. Final estimation of the measures is computed by averaging the results obtained for the 10 validation sets.

Empirical distributions of coefficients for the nonlinear ridge regression model were computed using a bootstrap procedure. Bootstrap resampling is a powerful statistical tool that allows to emulate the process of obtaining new datasets [138]. This approach can be used to estimate the coefficients distribution in a linear regression model. The idea is to obtain coefficients estimations from different datasets by repeatedly sampling observations from the original dataset [141].

Let us denote an observation as the pair $(TS_i, \boldsymbol{\varphi}_i)$, where, $i = 1, \ldots, N$, and N is the number of observations on the original dataset. The complete original dataset is, therefore, $Z = (\boldsymbol{TS}, \boldsymbol{\Phi})$. The bootstrap procedure consists in randomly selecting N observations, with replacement, from Z to obtain a bootstrap dataset Z^{*1}. Since resampling is performed with replacement, one observation can occur more than once in the bootstrap dataset. Coefficients are estimated using Z^{*1}, leading to a bootstrap estimate for $\boldsymbol{w}$, called $\hat{\boldsymbol{w}}^{*1}$. This procedure is repeated B times to produce B bootstrap data sets, $\{Z^{*i}\}_{i=1}^{B}$, and accordingly, to obtain B bootstrap estimates of the coefficients $\{\hat{\boldsymbol{w}}^{*i}\}_{i=1}^{B}$, see Figure 6.2.

The empirical distribution of the coefficients, being estimated with the previously explained procedure, allows us to perform a statistical hypothesis test to evaluate the relevance of every variable in the model. The null hypothesis is that $w_j = 0$, meaning that the associated variable is not relevant to explain TS. The alternative hypothesis is that $w_j \neq 0$, meaning that the corresponding variable is relevant, i.e. there is a linear relationship between variable and response. This can be stated as follows:

$$\begin{cases} H_0 : w_j = 0 \\ H_1 : w_j \neq 0 \end{cases} \qquad (6.14)$$
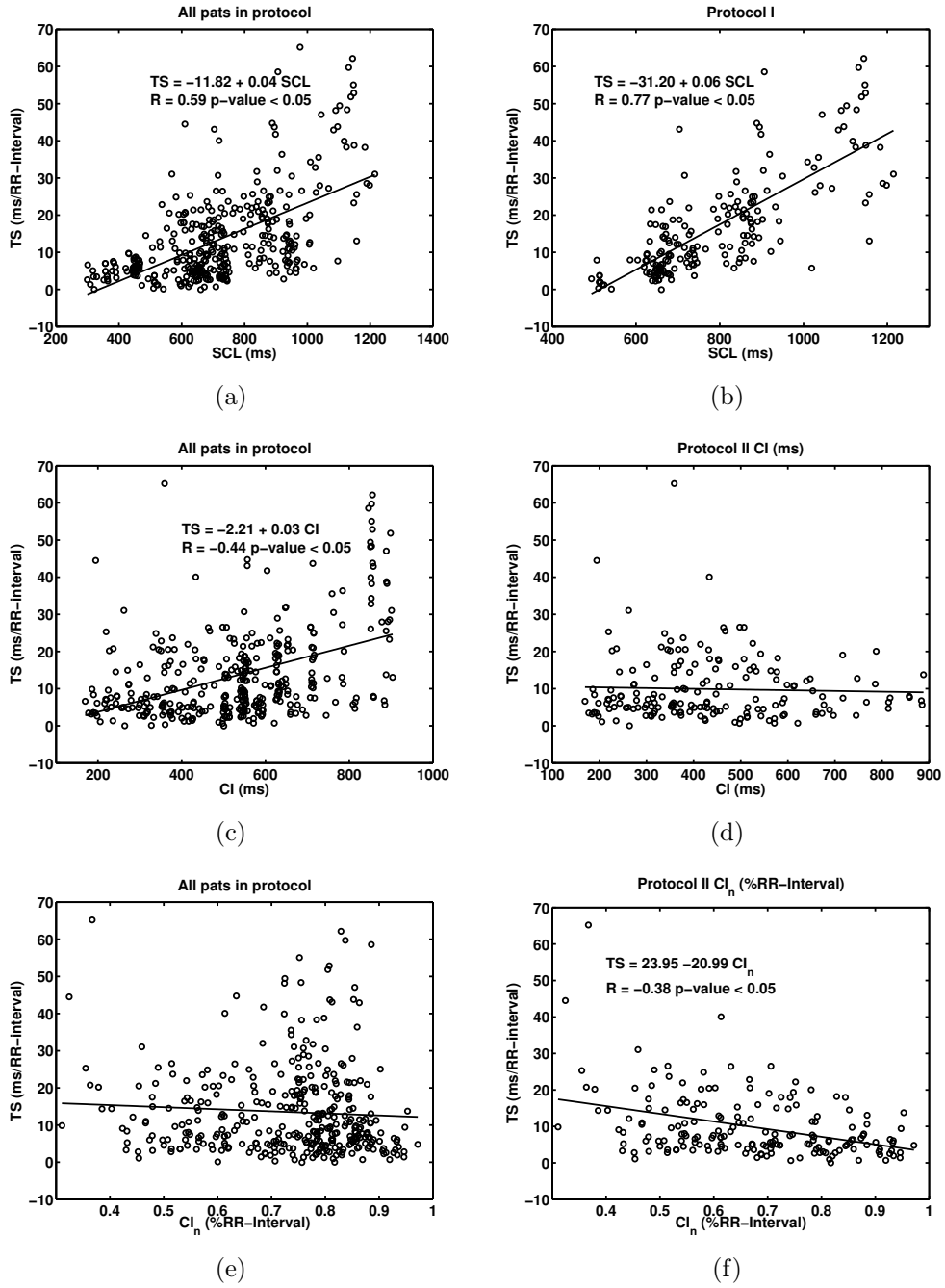
Figure 6.3: *Linear regression of TS parameter vs SCL, vs CI, and vs CI_n in a population with all patients from both protocols (a),(c), and (e), and in separated protocols: (b) Protocol-I, (d) and (f) Protocol-II.*

This hypothesis test is performed from the bootstrap empirical distribution of parameter w_j, so that whenever the 95% confidence interval contains the zero value H_0, is accepted, otherwise H_0 is rejected.
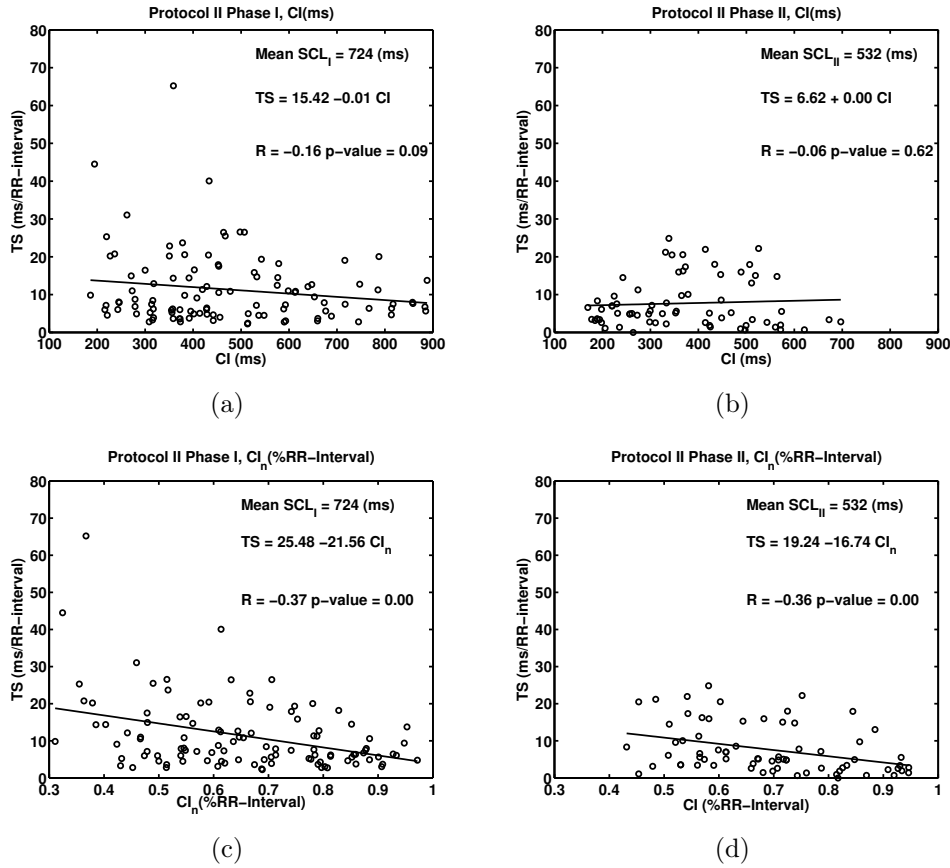
Figure 6.4: *Analysis of the interaction between HR and CI using data from patients in Protocol–II, Phase–I (a,c), and Phase–II (b,d). Mean and standard deviation of SCL for each phase is reported.*

6.5 Data Analysis and Results

In this section, the analysis of data using the simpler linear regression and nonlinear ridge regression models are presented. First, simple linear regression models are fitted using all the available data on the EPS database (aggregated data), aiming to reproduce the results in the literature [119]. Then, simple linear regression models are fitted using data separated into Protocol–I and Protocol–II, aiming to check whether the design of the protocol allows to verify the influenc of CI on HRT. Finally, nonlinear ridge regression models are fitted on EPS databases (aggragated data) and on AMI databases, aiming to verify if the proposed model is able to explain the influence of HR and CI on HRT. Additionally, the nonlinear ridge regression models are extended to take into account the AGE and SEX of patients.

6.5.1 Simple Linear Regression Analysis

Analysis on Aggregated Data

In order to establish a comparison with previous results in the literature, variables involved in simple linear regression models were first analyzed (TS-CI and TS-SCL), see Section 6.4.1. To reproduce results in the literature, aggregate data from EPS database are used.

Left panels in Figure 6.3 show the simple linear regression models given by Eqs. (6.3) and (6.1). Specifically, Figure 6.3(a) shows that the linear relationship between SCL and TS is significantly positive ($TS = -11.82 + 0.04\ SCL$, $R = 0.59$, $p < 0.05$). Figure 6.3(c) shows, also, a significantly positive relationship between CI and TS ($TS = -2.21 + 0.03\ CI$, $R = -0.44$, $p < 0.001$). The last result is apparently in contradiction with the HRT baroreflex source hypothesis, and it is consistent with previous work in [119], where TS was also found to be positively correlated with compensatory pause. Additionally, authors in [119] analyzed the relationship between CI_n (see Eq. (6.2)) and TS, and found no correlation. Accordingly, Figure 6.3(e) shows the same conclusion with our data ($R = -0.06$, p not significant).

Authors in [119] suggested, according to their experiments, that correlations were in fact due to strong influence of HR on HRT (low HR–high TS, and high HR–low TS), rather than an inherent relationship between HRT and CI. However, no further analysis was presented therein.

Isolated Effects of SCL and CI

Since EPS protocols (Protocol–I and Protocol–II) defined in Section 6.3.1 were designed to decouple the interaction between HR and CI, simpler linear regression models were fitted using patients from Protocol–I and Protocol–II separately.

Figure 6.3(b) shows the simple linear regression model between TS and SCL considering only data from patients in Protocol–I, where HR is controlled with isoproterenol. TS was positively correlated with SCL ($TS = -31.20 + 0.06\ SCL$, $R = 0.77$, $p < 0.01$).

Figure 6.3(d) shows the simple linear regression model between TS and CI with considering data from patients in Protocol–II, where CI was externally modified, as explained in Section 6.3.1. Results indicated that TS was uncorrelated with CI ($R = -0.04$, p not significant). However, as it is shown in Figure 6.3(f), linear regression between TS and CI_n yielded a significantly negative correlation ($TS = 23.95 - 20.99\ CI_n$, $R = -0.38$, $p < 0.001$). Normalization allowed to decouple the effect of SCL on CI using only data from patients in Protocol–II, revealing the expected physiological modulation of CI on TS.
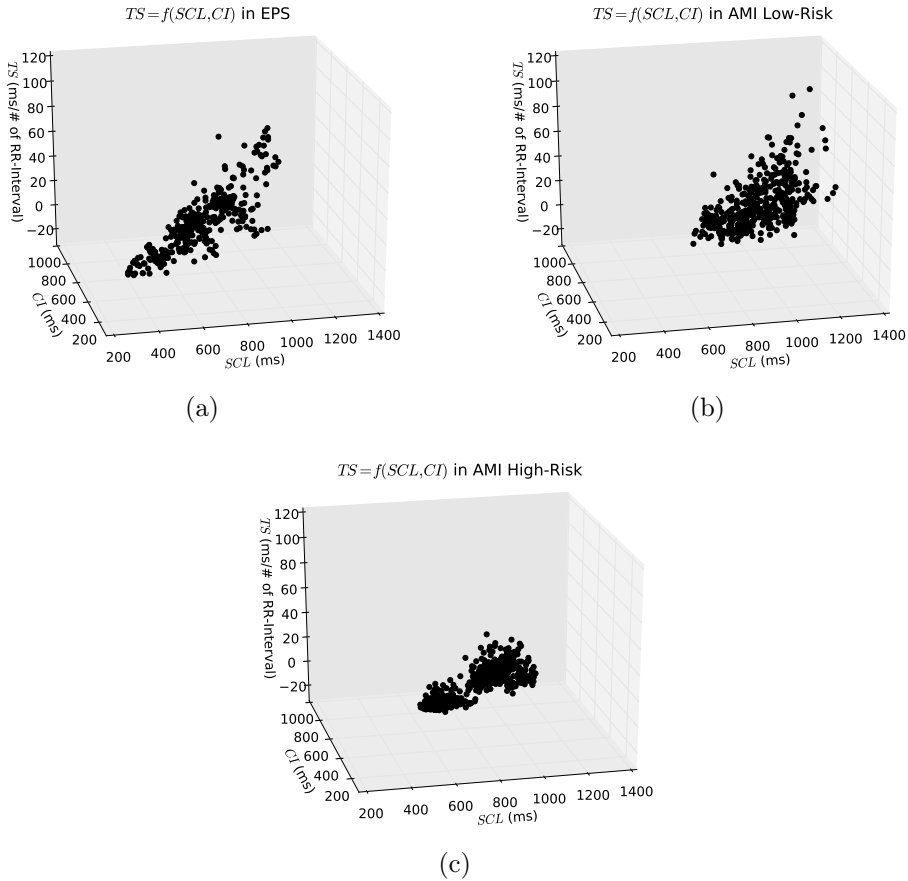
Figure 6.5: *Scatter 3D plots of TS vs SCL and CI for EPS subjects (a),*
AMI low-risk patients (b) and AMI high-risk patients (c).

Effect of SCL on CI in Protocol–II

Protocol–II was divided into two phases, allowing to study the effect of SCL
on CI. Then, simpler linear regression models betwen TS and CI were fitted
in both phases (I and II) of Protocol–II. Patients in Phase–I were not given
isoproterenol, hence their chronotropic state corresponded to high SCL (low
HR), whereas patients in Phase–II were under isoproterenol intervention and
hence their state corresponded to low SCL (high HR).

Figure 6.4 shows results of simple linear regression models for Phase–I
and –II. It showed no significant relationship ($p > 0.05$) between TS and
CI ($R = -0.16$ and $R = -0.006$, respectively). However, using CI_n yielded
TS models with significant negative slope, namely, $TS = 25.48 - 21.56\, CI_n$
with $R = -0.37$, and $TS = 19.24 - 16.74\, CI_n$ with $R = -0.36$, respectively,
both $p < 0.001$. This behavior was consistent with the HRT baroreflex
hypothesis source, and it was a confirmation that EPS protocol accounted
for interactions. Moreover, the slope coefficient was lower with high HR
(low SCL), showing an interaction effect of HR on SCL according to some
previous results [136, 142].

EPS	SCL	CI	AGE
SCL	1	0.85	0.05
CI	0.85	1	0.07
AGE	0.05	0.07	1

AMI low-risk	SCL	CI	AGE
SCL	1	0.32	-0.03
CI	0.32	1	0.22
AGE	-0.03	0.22	1

AMI high-risk	SCL	CI	AGE
SCL	1	0.92	-0.93
CI	0.92	1	-0.92
AGE	-0.93	-0.92	1

Table 6.3: *Correlation matrix for variables SCL, CI, AGE on EPS, AMI low-risk, and AMI high-risk databases.*

6.5.2 Nonlinear Ridge Regression Analysis

Nonlinear ridge regression models were fitted to the whole EPS database (aggregated data) and to both *AMI low-risk* and *AMI high-risk* databases. The model proposed in Section 6.4.2 was extended to include *AGE* and *SEX* variables. Since *SEX* is a qualitative variable with only two levels (male/female), its incorporation into the model is straightforward. A *dummy SEX* variable was created taking two possible numerical variables: $SEX = -1$ corresponds to male, $SEX = 1$ corresponds to female. The notation used to represent the nonlinear ridge regression models has three elements:

XXX aX sX

where the first three characters represent the order of the model, second (**2nd**) or third order (**3rd**), the second group of characters indicates whether the variable *AGE* is included in the model (**a1**) or not (**a0**), and finally, the third group of characters indicates whether the variable *SEX* is included in the model (**s1**) or not (**s0**). The nonlinear ridge regression models used and the corresponding notation is presented following:

- Second order models:

  - **2nd a0 s0**: $\varphi = \left[1, SCL, CI, SCL^2, CI^2, SCL \cdot CI \right]^T$

  - **2nd a1 s0**: $\varphi = \left[1, SCL, CI, SCL^2, CI^2, SCL \cdot CI, AGE \right]^T$

  - **2nd a1 s1**: $\varphi = \left[1, SCL, CI, SCL^2, CI^2, SCL \cdot CI, AGE, SEX \right]^T$

- Third order models:

  - **3rd a0 s0**: $\varphi = \left[1, SCL, CI, SCL^2, SCL^3, CI^2, SCL^3, SCL \cdot CI \right]^T$

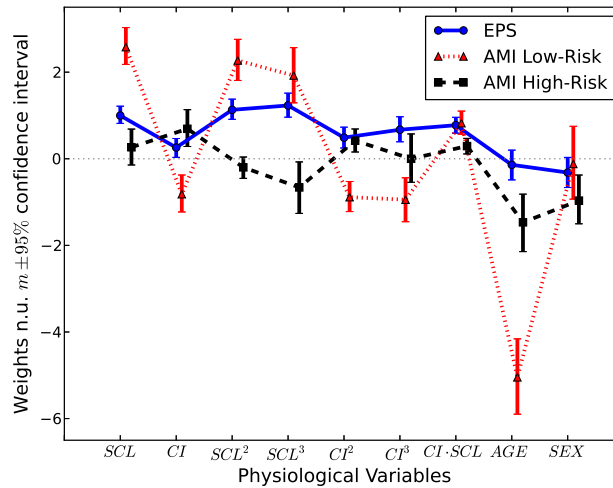 - **3rd a1 s0**: $\varphi = \left[1, SCL, CI, SCL^2, SCL^3, CI^2, SCL^3, SCL \cdot CI, AGE \right]^T$

Figure 6.6: *Mean and 95% confidence intervals of coefficients for the nonlinear ridge regression models with AGE and SEX variables for EPS, AMI low-risk, and AMI high-risk databases.*

– **3rd a1 s1**: $\boldsymbol{\varphi} = \left[1, SCL, CI, SCL^2, SCL^3, CI^2, SCL^3, SCL{\cdot}CI, AGE, SEX\right]^T$

Table 6.3 shows the correlation matrices between SCL, CI, and AGE variables for EPS, AMI low-risk, and AMI high-risk databases. SCL and CI showed strong correlation in EPS database. However, these are not free variables since they are controlled according to the Protocol proposed in Section 6.3. On the other hand, the correlation between them on AMI low-risk database was weaker. AGE was strongly negative correlated with both SCL and CI in AMI high-risk database.

Figure 6.5 shows a 3D scatterplot for TS in terms of SCL and CI, on EPS, AMI low-risk, and AMI high-risk databases. It can be pointed out that EPS and AMI low-risk presented similar point distributions, with higher variance than AMI high-risk.

Since some of the features are powers or combinations of SCL and CI, the ranges of values vary widely. Thus, features with large values may have larger influence in the cost function. To overcome this problem, a usual approach is to scale the data by subtracting the mean and dividing by the standard deviation [143]. Therefore, coefficients are presented in normalized units (n.u.).

Table 6.4 shows coefficients values of the nonlinear ridge regression models fitted to EPS database. The best models, in terms of MSE and R^2, were **2nd a0 s0** and **3rd a0 s0**, this is without AGE and SEX variables. In both models, coefficient of CI variable was significant and with a negative correlation with TS, in agreement with the hypothesis of baroreflex source of HRT. Coefficients relating SCL variables with TS were significant and positive. Interaction term $SCL \cdot CI$ was also significant for these models, and for all models. Table 6.5 shows coefficient values of the best models

2nd a0 s0 and **3rd a0 s0**, refitted by removing iteratively nonsignificant variables until all the variables were significant. However, the hierarchical principle states that if we include an interaction in a model, the main effects should also be included, even if the p-values associated with their coefficients are not significant [141]. Table 6.6 shows coefficient values of the complete model (**3rd a1 s1**) but without regularization term (setting $\lambda = 0$) showing the necessity for using the regularization term.

Table 6.7 shows coefficient values of the nonlinear ridge regression models fitted to AMI low-risk database. All the variables except SEX were significant in all the models. Even more, variables relating CI and TS showed negative relationship in agreement with the baroreflex source. Similarly, variables relating SCL and TS showed positive relationship. AGE had a negative significant relationship with TS. Table 6.8 shows coefficient values of the nonlinear ridge regression models fitted to AMI high-risk database. The relationship between variables and TS was completely different than in EPS and AMI low-risk database. The coefficient values were always smaller than 1.8 units.

Figure 6.6 shows mean and 95% confidence interval, estimated with bootstrap, of coefficients of nonlinear ridge regression model (**3rd a1 s1**) fitted to EPS, AMI low-risk, and AMI high-risk database.

6.6   Discussion and Conclusions

Previous studies [119, 127, 133, 134] showed conflicting results when assessing the effect of the CI on HRT parameters, and even contrary to the baroreflex origin hypothesis of the HRT. In this chapter, an EPS protocol to stimulate VPC on patients with with structurally normal heart was designed. HR and CI were controlled in order to decouple the interaction on HRT. Simple linear regression analysis confirmed previous results about the influence of CI on HRT. A nonlinear ridge regression model was proposed in order to take into account interaction terms and nonlinear relationship between variables and HRT. Nonlinear ridge regression models were used to analyze EPS, AMI low-risk and AMI high-risk databases. The model proposed was able to explain the influence of HR and CI on HRT in agreement with the baroreflex source hypothesis on EPS and AMI low-risk database. AMI high-risk patients showed a completely different relationship, that might be viewed as a breakdown of the physiological control on the HRT response.

EPS	SCL	CI	SCL^2	SCL^3	CI^2	CI^3	$SCL*CI$	AGE	SEX	MSE	R^2
2nd a0 s0	1.29	**-5.95***	**5.32***	—	2.38	—	**3.75***	—	—	107.61	0.25
2nd a1 s0	**1.71***	0.11	**2.08***	—	**0.73***	—	**1.32***	-0.26	—	123.74	0.14
2nd a1 s1	**1.31***	**0.46***	**1.49***	—	**0.75***	—	**1.09***	-0.16	-0.35	127.23	0.12
3rd a0 s0	**1.50***	**-2.37***	**2.36***	**3.34***	-0.23	**1.57***	**0.85***	—	—	107.56	0.25
3rd a1 s0	**1.20***	-0.01	**1.43***	**1.61***	**0.39***	**0.73***	**0.84***	-0.21	—	119.70	0.17
3rd a1 s1	**1.00***	**0.26***	**1.13***	**1.24***	**0.49***	**0.67***	**0.78***	-0.14	-0.32	123.08	0.15

Table 6.4: *Coefficients values of nonlinear ridge regression models fitted to EPS database. Significant variables are highlighted and denoted by *. Symbol – means that the variable was not included in the model.*

EPS	SCL	CI	SCL^2	SCL^3	CI^2	CI^3	$SCL*CI$	AGE	SEX	MSE	R^2
2nd a0 s0 rebuilt	X	**-3.76***	**6.17***	—	X	X	**4.31***	—	—	106.28	0.26
3rd a0 s0 rebuilt	X	**-2.15***	**3.04***	**4.20***	X	X	**1.83***	—	—	105.91	0.27

Table 6.5: *Coefficients values of the best nonlinear ridge regression models rebuilt by removing (iteratively) nonsignificant variables. Significant variables are highlighted and denoted by *. Symbol – means that the variable was not included in the model. Symbol X means that the variable was removed because it was nonsignificant.*

EPS	SCL	CI	SCL^2	SCL^3	CI^2	CI^3	$SCL*CI$	AGE	SEX	MSE	R^2
3rd a1 s1	**41.97***	-24.18	-79.76	44.05	30.40	-13.71	8.42	-0.42	-0.04	169.01	-0.17

Table 6.6: *Nonlinear regression model **3rd a1 s1** fitted to EPS database without regularization. Significant variables are highlighted and denoted by *.*

AMI low-risk	SCL	CI	SCL^2	SCL^3	CI^2	CI^3	$SCL*CI$	AGE	SEX	MSE	R^2
2nd a0 s0	**3.44***	**-1.55***	**3.32***	–	**-1.83***	–	**0.82***	–	–	300.93	0.13
2nd a1 s0	**3.25***	**-1.15***	**2.96***	–	**-1.28***	–	**1.03***	**-5.18***	–	239.06	0.31
2nd a1 s1	**3.24***	**-1.15***	**2.95***	–	**-1.29***	–	**1.01***	**-5.15***	-0.17	240.64	0.31
3rd a0 s0	**2.65***	**-1.05***	**2.49***	**2.28***	**-1.26***	**-1.43***	**0.63***	–	–	297.20	0.15
3rd a1 s0	**2.59***	**-0.81***	**2.28***	**1.92***	**-0.90***	**-0.97***	**0.82***	**-5.07***	–	238.29	0.32
3rd a1 s1	**2.59***	**-0.81***	**2.27***	**1.92***	**-0.90***	**-0.98***	**0.81***	**-5.05***	-0.13	239.74	0.31

Table 6.7: Coefficients values of nonlinear ridge regression models fitted to AMI low-risk database. Significant variables are highlighted and denoted by $*$. Symbol – means that the variable was not included in the model.

AMI high-risk	SCL	CI	SCL^2	SCL^3	CI^2	CI^3	$SCL*CI$	AGE	SEX	MSE	R^2
2nd a0 s0	**1.13***	**1.63***	**-0.69***	–	0.14	–	0.02	–	–	16.77	0.21
2nd a1 s0	0.48	**0.84***	**-0.86***	–	0.27	–	-0.01	**-1.57***	–	16.68	0.21
2nd a1 s1	0.07	**0.78***	**-0.64***	–	0.42	–	0.13	**-1.53***	**-1.04***	16.70	0.21
3rd a0 s0	**1.18***	**1.47***	0.08	**-1.12***	**0.59***	-0.58	**0.57***	–	–	16.82	0.20
3rd a1 s0	0.55	**0.70***	-0.15	**-0.85***	**0.37***	-0.10	**0.29***	**-1.46***	–	16.75	0.21
3rd a1 s1	0.27	**0.69***	-0.20	**-0.66***	**0.42***	0.00	**0.30***	**-1.46***	**-0.97***	16.77	0.21

Table 6.8: Coefficients values of nonlinear ridge regression models fitted to AMI high-risk database. Significant variables are highlighted and denoted by $*$. Symbol – means that the variable was not included in the model.

Chapter 7

Conclusions and Future Work

7.1 Conclusions

In this Thesis, different robust signal processing to characterize cardiac fibrillations and baroreflex and ASN control of the HR have been proposed.

Part II of the Thesis addressed the problem of characterizing spectral properties of VF and AF. Specifically, in Chapter 2 a parametric method to study VF has been proposed. The method, called FOA, is an extension of Fourier Series expansion that accounts for the irregularity present in the VF signals. To test the proposed method, controlled electrophysiological substrates have been simulated, and synthetic EGM have been obtained. Also, a small database with four different rhythms, and an extensive VF database, have been analyzed. The database with different rhythms aimed to evaluate the performance of the two different approaches, the classical DFA and the proposed FOA, in real EGM recordings with different electrophysiological and well-known situations. VF database aimed to evaluated the performance of both approaches in a real set with a large number of EGM recordings. Results showed that FOA provides better results estimating the periodicity than the DFA approach. This methodology allowed us to give a principled understanding of the meaning and limitations of the different indices currently used in the DFA and OA literature, and also to check the improvement given by the FOA spectral description.

In Chapter 3, a new method based on the Correntropy function was proposed to estimate the f_0 of AF signals. A combination of this method with multicomponent FOA was proposed to model complex AF signals, under the assumption that the complexity may be originated by the interaction of two (or more) wavefronts with different fundamental frequencies. Both methods were compared with the classic approach based on DFA, which characterizes the periodicity of the AF signal by means of the f_d calculated on a preprocessed signal. A set of experiments with pseudo-real AF signals were designed to verify the adequacy of the proposed approach. In addition, two different datasets were assembled, one with regular and homogeneous AF signals, and another one with complex AF signals. The proposed methods allowed, on the one hand, to characterize the periodicity of regular AF sig-

nals, and on the other hand, to improve the characterization of more complex signals.

Part III addressed the problem of assessment of baroreflex and ANS control of the heart rhythm. Specifically, in Chapter 4 a SVM framework for nonuniform interpolation based on spectrally adapted Mercer kernels was proposed. Several experiments were carried out to compare the spectrally adapted kernels approach with low-pass kernels and with other techniques. The results showed that the SVM with the autocorrelation kernels outperformed the other methods regardless the spectrum of the observed signal. Finally, the proposed approach was tested in a few Holter recordings from healthy and congestive heart failure patients. In this case, the filtering process carried out with the autocorrelation kernel allowed to attenuate the noise level while enhancing the signal power in the frequency bands of interest, which might avoid the time-consuming task of manual correction on Holter recordings.

In Chapter 5, a denoising method based on SVM interpolation has been proposed for VPC-tachograms signals in HRT. The use of a gold standard database with pacing induced VPC during EPS has been used for comparison of the HRT behavior, both in the time and in the spectral domains. In low-noise conditions, the SVM algorithm yielded results that were similar to other conventional filtering methods, and in all cases the results were according to the expected mechanism of the HRT. For VPC-tachograms in this EPS database, denoising algorithms also were shown to yield similar spectral profiles of HRT. In the presence of noise, i.e., in the Holter database, the tested algorithms yielded denoised VPC signals containing lower noise level. However, SVM algorithm obtained a higher performance when compared to the median and to the FIR filters. SVM algorithm preserved oscillations expected in the HRT, the spectral profile of the denoised VPC-tachogram was more similar to the observed in the gold standard, standard deviation was lower, and the significantly higher values of Turbulence Length suggest that the noise was more efficiently removed from the turbulence. The proposed SVM algorithm allows to perform the HRT analysis even when a low number of VCPs are available. This characteristic has clinical implications, because one of the current requirements for suitability of a patient to be studied in terms of TS is a sufficient number of VPCs being available. Thus, HRT denoising will help to extend the HRT analysis to a higher number of patients. The SVM algorithm gives a better description of the dependence with the HR previous to the VPC-tachogram, and allows the analysis of the changes of HRT with time.

In Chapter 6, a nonlinear regression model to characterize the influence of CI and HR on HRT responses was proposed. The model was used in a database of healthy patients with pacing induced VPC during EPS. Also, a database of Holter recordings from patients that had suffered an AMI was used. The nonlinear regression model was able to explain the influence of CI and HR on the HRT in healthy subjects, and in patients with low risk of SCD (measured by HRT parameters). Evenmore, the results agreed with

the baroreflex source of HRT hypothesis.

7.2   Future work

In this section some future directions are itemized, aiming to propose different threads to explore further the methods proposed in this Thesis.

Regarding fibrillatory arrhytmias we propose:

- To develop a robust method to statistically select components in the multicomponent FOA approach. According to this, a new component should be included in the final FOA model only if the improvement explaining the signal is statistically significant. This can help to better characterize complex AF and VF signals.

- To extend the multicomponent FOA approach to provide time-variant track evolution of the irregularity of AF and VF signals.

- To validate proposed approaches in relevant database to evaluate the clinical impact, and the correlation with different clinical variables. In VF, study the impact of the location of the myocardial infarction on the FOA measurements. In AF, study of the correlation of FOA approach and the different types of AF, namely, paroxysmal, permanent, persistent.

Regarding the assessment of the baroreflex and ANS we propose:

- To further study the applicability of SVM nonuniform interpolation of HRV long recordings, namely 7 and 21 days. An excellent gold standard would be a database of long recordings manually corrected by cardiologists. This would allow to compare raw with cleaned HRV signals, and even to create HRV pseudo-real signals with the presence of different level of noise, artifacts and miss-detections.

- To develop a method to include local physiological information on the assessment of HRT. As shown by our results, the HRT response is closely linked to the local physiological condition, and including this information should provide with better characterization. Also, the proposed methodology would allow to easily incorporate additional and information, such as the correlation between HRT from individual VPCs and the previous HRV assessment. This would lead to a complete characterization of the baroreflex and ANS control of the HR.

References

[1] J. Ng, A. H. Kadish, and J. J. Goldberger, "Effect of electrogram characteristics on the relationship of dominant frequency to atrial activation rate in atrial fibrillation," *Heart Rhythm*, vol. 3, pp. 1295–1305, 2006.

[2] P. Sanders, O. Berenfeld, M. Hocini, P. Jaïs, R. Vaidyanathan, L.-F. Hsu, S. Garrigue, Y. Takahashi, M. Rotter, F. Sacher *et al.*, "Spectral analysis identifies sites of high-frequency activity maintaining atrial fibrillation in humans," *Circulation*, vol. 112, pp. 789–797, 2005.

[3] G. W. Botteron and J. M. Smith, "A technique for measurement of the extent of spatial organization of atrial activation during atrial fibrillation in the intact human heart," *IEEE Transactions on Biomedical Engineering*, vol. 42, pp. 579–586, 1995.

[4] M. Malik, J. T. Bigger, A. J. Camm, R. E. Kleiger, A. Malliani, A. J. Moss, and P. J. Schwartz, "Heart rate variability. Standards of measurement, physiological interpretation, and clinical use." *European Heart Journal*, vol. 17, pp. 354–381, 1996.

[5] G. Schmidt, M. Malik, P. Barthel, R. Schneider, K. Ulm, L. Rolnitzky, A. J. Camm, J. T. Bigger, and A. Schömig, "Heart-rate turbulence after ventricular premature beats as a predictor of mortality after acute myocardial infarction," *Lancet*, vol. 353, pp. 1390–1396, 1999.

[6] A. Bauer, M. Malik, G. Schmidt, P. Barthel, H. Bonnemeier, I. Cygankiewicz, P. Guzik, F. Lombardi, A. Müller, A. Oto *et al.*, "Heart rate turbulence: standards of measurement, physiological interpretation, and clinical use: International Society for Holter and Noninvasive Electrophysiology Consensus," *Journal of the American College of Cardiology*, vol. 52, pp. 1353–1365, 2008.

[7] M. Watanabe and M. Josephson, "Heart rate turbulence in the spontaneous ventricular tachy-arrhythmia database," *PACE Part II*, vol. 23, p. 686, 2000.

[8] R. E. Klabunde, *Cardiovascular Physiology Concepts*, 2nd ed. Lippincott Williams & Wilkins, 2005.

[9] J. T. Ottesen, M. S. Olufsen, and J. K. Larsen, *Applied mathematical models in human physiology.* SIAM, 2004, vol. 9.

[10] G. D. Clifford, F. Azuaje, and P. McSharry, *Advanced methods and tools for ECG data analysis.* Artech house London, 2006.

[11] L. Sörnmo and P. Laguna, *Bioelectrical signal processing in cardiac and neurological applications.* Elsevier Academic Press, 2005.

[12] A. L. Goldberger, *Clinical electrocardiography: a simplified approach*, 6th ed. Mosby, 1999.

[13] R. A. Gray and J. Jalife, "Ventricular fibrillation and atrial fibrillation are two different beasts." *Chaos: An Interdisciplinary Journal of Nonlinear Science*, vol. 8, pp. 65–78, 1998.

[14] R. Gray, A. Pertsov, and J. Jalife, "Spatial and temporal organization during cardiac fibrillation," *Nature*, no. 392, pp. 20–1, 1998.

[15] A. J. Camm, P. Kirchhof, G. Y. Lip, U. Schotten, I. Savelieva, S. Ernst, I. C. Van Gelder, N. Al-Attar, G. Hindricks, and B. Prendergast, "Guidelines for the management of atrial fibrillation The Task Force for the Management of Atrial Fibrillation of the European Society of Cardiology (ESC)," *European Heart Journal*, vol. 31, pp. 2369–2429, 2010.

[16] A. C. Skanes, R. Mandapati, O. Berenfeld, J. M. Davidenko, and J. Jalife, "Spatiotemporal periodicity during atrial fibrillation in the isolated sheep heart," *Circulation*, vol. 98, pp. 1236–1248, 1998.

[17] R. Clayton, A. Murray, and R. Campbell, "Frequency analysis of self-terminating ventricular fibrillation," in *Proc. Computers in Cardiology, Bethesda, MD, USA*, vol. 23, 1994, pp. 705–8.

[18] M. Haïssaguerre, P. Jaïs, D. C. Shah, A. Takahashi, M. Hocini, G. Quiniou, S. Garrigue, A. Le Mouroux, P. Le Métayer, and J. Clémenty, "Spontaneous initiation of atrial fibrillation by ectopic beats originating in the pulmonary veins." *The New England Journal of Medicine*, vol. 339, pp. 659–666, Sep. 1998.

[19] G. K. Moe, W. C. Rheinboldt, and J. A. Abildskov, "A Computer Model of Atrial Fibrillation." *American Heart Journal*, vol. 67, pp. 200–220, Feb. 1964.

[20] J. Jalife, O. Berenfeld, and M. Mansour, "Mother rotors and fibrillatory conduction: a mechanism of atrial fibrillation." *Cardiovascular Research*, vol. 54, pp. 204–216, 2002.

[21] L. Sörnmo, M. Stridh, D. Husser, A. Bollmann, and S. B. Olsson, "Analysis of atrial fibrillation: from electrocardiogram signal processing to clinical management." *Philosophical Transactions of the Royal Society of London. Series A, Mathematical, Physical, and Engineering Sciences*, vol. 367, pp. 235–253, 2009.

[22] F. Atienza, J. Almendral, J. Moreno, R. Vaidyanathan, A. Talkachou, J. Kalifa, A. Arenal, J. P. Villacastín, E. G. Torrecilla, A. Sánchez *et al.*, "Activation of inward rectifier potassium channels accelerates atrial fibrillation in humans evidence for a reentrant mechanism," *Circulation*, vol. 114, pp. 2434–2442, 2006.

[23] J. Ng, A. H. Kadish, and J. J. Goldberger, "Technical Considerations for Dominant Frequency Analysis," *Journal of Cardiovascular Electrophysiology*, vol. 18, pp. 757–764, 2007.

[24] F. H. Samie, O. Berenfeld, J. Anumonwo, S. F. Mironov, S. Uassi, J. Beaumont, S. Taffet, A. M. Pertsov, and J. Jalife, "Rectification of the background potassium current: A determinant of rotor dynamics in ventricular fibrillation," *Circulation Research*, vol. 89, pp. 1216–1223, 2001.

[25] T. H. Everett, J. R. Moorman, L. C. Kok, J. G. Akar, and D. E. Haines, "Assessment of global atrial fibrillation organization to optimize timing of atrial defibrillation," *Circulation*, vol. 103, pp. 2857–61, 2001.

[26] T. H. Everett, L. C. Kok, J. R. Moorman, and D. E. Haines, "Frequency domain algorithm for quantifying atrial fibrillation organization to increase defibrillation efficacy," *IEEE Transactions on Biomedical Engineering*, vol. 48, pp. 969–977, 2001.

[27] D. P. Zipes, A. J. Camm, M. Borggrefe, A. E. Buxton, B. Chaitman, M. Fromer, G. Gregoratos, G. Klein, A. J. Moss, R. J. Myerburg *et al.*, "Acc/aha/esc 2006 guidelines for management of patients with ventricular arrhythmias and the prevention of sudden cardiac deatha report of the american college of cardiology/american heart association task force and the european society of cardiology committee for practice guidelines (writing committee to develop guidelines for management of patients with ventricular arrhythmias and the prevention of sudden cardiac death)," *Journal of the American College of Cardiology*, vol. 48, pp. e247–e346, 2006.

[28] J. Jalife, "Ventricular fibrillation: mechanisms of initiation and maintenance." *Annual Review of Physiology*, vol. 62, pp. 25–50, 2000.

[29] T. Taneja, J. Goldberger, M. A. Parker, D. Johnson, N. Robinson, G. Horvath, and A. H. Kadish, "Reproducibility of ventricular fibrillation characteristics in patients undergoing implantable cardioverter

defibillator implantation," *Journal of Cardiovascular Electrophysiology*, vol. 8, pp. 1209–1217, 1997.

[30] R. H. Clayton, A. Murray, and R. W. Campbell, "Comparison of four techniques for recognition of ventricular fibrillation from the surface ECG." *Medical & Biological Engineering & Computing*, vol. 31, pp. 111–117, 1993.

[31] J. Ng and J. J. Goldberger, "Understanding and Interpreting Dominant Frequency Analysis of AF Electrograms," *Journal of Cardiovascular Electrophysiology*, vol. 18, pp. 680–685, 2007.

[32] O. Rompelman, A. J. R. M. Coenen, and R. I. Kitney, "Measurement of heart-rate variability: Part 1—comparative study of heart-rate variability analysis methods," *Medical & Biological Engineering & Computing*, vol. 15, pp. 233–239, 1977.

[33] J. Mateo and P. Laguna, "Analysis of heart rate variability in the presence of ectopic beats using heart timing signal," *IEEE Transactions on Biomedical Engineering*, vol. 50, p. 334, 2003.

[34] R. Hainsworth, "Physiological background of heart rate variability," in *Dynamic Electrocardiography*, M. Malik and A. J. Camm, Eds. Blackwell Futura, 2004.

[35] M. Malik, T. Farrell, T. Cripps, and A. J. Camm, "Heart rate variability in relation to prognosis after myocardial infarction: Selection of optimal processing techniques," *European Heart Journal*, vol. 10, pp. 1060–1074, 1989.

[36] H. Huikuri, T. Makikallio, J. Airaksinen, R. Mitrani, A. Castellanos, and R. Myerburg, "Measurement of heart rate variability: A clinical tool or a research toy?." *Journal of the American College of Cardiology*, vol. 34, pp. 1878–1883, 1999.

[37] G. D. Clifford, "Signal processing methods for heart rate variability," Ph.D. dissertation, University of Oxford, 2002.

[38] S. M. Kay and S. L. Marple, "Spectrum analysis-a modern perspective," *Proceedings of the IEEE*, vol. 69, pp. 1380–1419, 1981.

[39] S. Cerutti, A. M. Bianchi, and L. T. Mainardi, "Spectral analysis of the heart rate variability," in *Heart Rate Variability*, M. Malik and A. J. Camm, Eds. New York: Futura Publishing Company, 1995.

[40] M. V. Kamath and E. L. Fallen, "Power Spectral Analysis of Heart Rate Variability: A Noninvasive Signature of Cardiac Autonomic Function," *Critical Reviews in Biomedical Engineering*, vol. 21, pp. 245–311, 1993.

[41] M. J. Lisenby and P. C. Richardson, "The beatquency domain: An unusual application of the fast fourier transform," *IEEE Transactions on Biomedical Engineering*, vol. 24, pp. 405–408, July 1977.

[42] B. M. Sayers, "Analysis of Heart Rate Variability," *Ergonomics*, vol. 16, pp. 17–32, 1973.

[43] S. Akselrod, "Power spectrum analysis of heart rate fluctuation: a quantitative probe of beat-to-beat cardiovascular control." *Science*, vol. 213, pp. 220–222, 1981.

[44] H. V. Huikuri, T. H. Mäkikallio, and J. Perkiömäki, "Measurement of heart rate variability by methods based on nonlinear dynamics," *Journal of Electrocardiology*, vol. 36, p. 95, 2003.

[45] A. L. Goldberger, "Nonlinear dynamics, fractals, and chaos theory: Implications for neuroautonomic heart rate control in health and disease," in *The Autonomic Nervous System*, C. Bolis and J. Licinnio, Eds. Geneva: World Health Organization, 1999.

[46] M. Malik and A. J. Camm, *Dynamic electrocardiography.* Wiley Online Library, 2004.

[47] M. Watanabe and G. Schmidt, "Heart rate turbulence: A 5-year review," *Heart Rhythm*, vol. 1, pp. 732–738, 2004.

[48] P. Barthel, R. Schneider, A. Bauer, K. Ulm, C. Schmitt, A. Schömig, and G. Schmidt, "Risk stratification after acute myocardial infarction by heart rate turbulence," *Circulation*, vol. 108, pp. 1221–1226, 2003.

[49] I. Cygankiewicz, "Heart rate turbulence." *Progress in Cardiovascular Diseases*, vol. 56, pp. 160–171, 2013.

[50] M. Biermann, M. Shenasa, and M. Borggrefe, *Cardiac Mapping.* NY, USA: Futura Publishing, 1993, ch. The Interpretation of Cardiac Electrograms.

[51] W. M. Smith, J. M. Wharton, and S. M. Blanchard, *Cardiac Electrophysiology: From Cell to Bedside.* Philadelphia, USA: WB Saunders Co, 1990, ch. Direct Cardiac Mapping.

[52] L. Mørkrid, O. J. Ohm, and H. Engedal, "Time domain and spectral analysis of electrograms in man during regular ventricular activity and ventricular fibrillation," *IEEE Transactions on Biomedical Engineering*, vol. 31, pp. 350–355, 1984.

[53] H. S. Karagueuzian, S. S. Khan, W. Peters, W. J. Mandel, and G. A. Diamond, "Nonhomogeneous local atrial activity during acute atrial fibrillation: Spectral and dynamic analysis," *PACE*, vol. 13, pp. 1937–1942, 1990.

[54] D. S. Rosenbaum and R. J. Cohen, "Frequency based measures of atrial fibrillation in man," *IEEE Engineering in Medicine and Biology Society*, vol. 12, pp. 582–583, 1990.

[55] J. Chen, R. Mandapati, O. Berenfeld, A. C. Skanes, and J. Jalife, "High-frequency periodic sources underlie ventricular fibrillation in the isolated rabbit heart," *Circulation Research*, vol. 86, pp. 86–93, 2000.

[56] A. V. Zaitsev, O. Berenfeld, S. F. Mironov, J. Jalife, and A. M. Pertsov, "Distribution of excitation frequencies on the epicardial and endocardial surfaces of fibrillating ventricular wall of the sheep heart," *Circulation Research*, vol. 86, pp. 408–417, 2000.

[57] A. Casaleggio, P. Rossi, A. Faini, T. Guidotto, V. Malavasi, G. Musso, and G. Sartori, "Analysis of implantable cardioverter defibrillator signals for non conventional cardiac electrical activity characterization," *Medical & Biological Engineering & Computing*, vol. 44, pp. 45–53, 2006.

[58] S. Singh, E. Heist, J. Koruth, C. Barrett, J. Ruskin, and M. Mansour, "The relationship between electrogram cycle length and dominant frequency in patients with persistent atrial fibrillation." *Journal of Cardiovascular Electrophysiology*, vol. 20, no. 12, pp. 1336–42, 2009.

[59] J. J. Sánchez-Muñoz, J. L. Rojo-Álvarez, A. García-Alberola, E. Everss, F. Alonso-Atienza, M. Ortiz, J. Martínez-Sánchez, J. Ramos-López, and M. Valdés-Chavarri, "Spectral analysis of intracardiac electrograms during induced and spontaneous ventricular fibrillation in humans," *Europace*, vol. 11, pp. 328–331, 2009.

[60] J. J. Sánchez-Muñoz, J. L. R. Álvarez, A. G. Alberola, J. R. Carrión, E. Everss, M. Ortiz, J. M. Sánchez, and M. V. Chávarria, "Spectral analysis of sustained and non-sustained ventricular fibrillation in patients with an implantable cardioverter-defibrillator," *Revista Española de Cardiología*, vol. 62, pp. 690–693, 2009.

[61] J. J. Sánchez-Muñoz, J. L. Rojo-Álvarez, A. García-Alberola, E. Everss, J. Requena-Carrión, M. Ortiz, F. Alonso-Atienza, and M. Valdés-Chavarri, "Effects of the location of myocardial infarction on the spectral characteristics of ventricular fibrillation," *Pacing and clinical electrophysiology*, vol. 31, pp. 660–665, 2008.

[62] J. L. Rojo-Álvarez, Á. Arenal-Maíz, and A. Artés-Rodríguez, "Support vector black-box interpretation in ventricular arrhythmia discrimination," *IEEE Engineering in Medicine and Biology Magazine*, vol. 21, pp. 27–35, 2002.

[63] K. Minami, H. Nakajima, and T. Toyoshima, "Real-Time Discrimination of Ventricular Tachyarrhythmia with Fourier-Transform Neural

Network," *IEEE Transactions on Biomedical Engineering*, vol. 46, pp. 179–85, 1999.

[64] J. W. Picone, "Signal modelling techniques in speech recognition," *Proceedings of the IEEE*, vol. 81, pp. 1215–1247, 1993.

[65] F. Alonso-Atienza, J. Requena-Carrión, A. García-Alberola, J. L. Rojo-Álvarez, J. J. Sánchez-Muñoz, J. Martínez-Sánchez, and M. Valdés-Chávarri, "A probabilistic model of cardiac electrical activity based on a cellular automata system," *Revista Española de Cardiología (English Edition)*, vol. 58, pp. 41–47, 2005.

[66] J. Malmivuo and R. Plonsey, *Principles and Applications of Bioelectric and Biomagnetic Fields*. New York: Oxford University Press, 1995.

[67] J. Kalifa, K. Tanaka, A. V. Zaitsev, M. Warren, R. Vaidyanathan, D. Auerbach, S. Pandit, K. L. Vikstrom, R. Ploutz-Snyder, A. Talkachou *et al.*, "Mechanisms of wave fractionation at boundaries of high-frequency excitation in the posterior left atrium of the isolated sheep heart during atrial fibrillation," *Circulation*, vol. 113, pp. 626–633, 2006.

[68] G. Fischer, M. C. Stühlinger, C. N. Nowak, L. Wieser, B. Tilg, and F. Hintringer, "On computing dominant frequency from bipolar intracardiac electrograms," *IEEE Transactions on Biomedical Engineering*, vol. 54, pp. 165–169, 2007.

[69] O. Berenfeld, S. Ennis, E. Hwang, B. Hooven, K. Grzeda, S. Mironov, M. Yamazaki, J. Kalifa, and J. Jalife, "Time and Frequency Domains Analyses of Atrial Fibrillation Activation Rate: The Optical Mapping Reference," *Heart rhythm*, pp. 1–45, 2011.

[70] M. Haisaguerre, P. Sanders, M. Hocini, L.-F. Hsu, D. C. Shah, C. Scavée, Y. Takahshi, M. Rotter, J.-L. Pasquié, S. Garrigue *et al.*, "Changes in atrial fibrillation cycle length and inducibility during catheter ablation and their relation to outcome." *Circulation*, vol. 109, pp. 3007–3013, 2004.

[71] A. Elvan, A. C. Linnenbank, M. W. van Bemmel, A. R. R. Misier, P. P. H. M. Delnoy, W. P. Beukema, and J. M. T. de Bakker, "Dominant frequency of atrial fibrillation correlates poorly with atrial fibrillation cycle length," *Circulation: Arrhythmia and Electrophysiology*, vol. 2, pp. 634–644, 2009.

[72] E. J. Ciaccio, A. B. Biviano, W. Whang, J. Coromilas, and H. Garan, "A new transform for the analysis of complex fractionated atrial electrograms." *Biomedical Engineering Online*, vol. 10, p. 35, 2011.

[73] K. R. Grzęda, S. F. Noujaim, O. Berenfeld, and J. Jalife, "Complex fractionated atrial electrograms: Properties of time-domain versus frequency-domain methods," *Heart rhythm*, vol. 6, pp. 1475–1482, 2009.

[74] I. Santamaría, P. Pokharel, and J. Principe, "Generalized correlation function: definition, properties, and application to blind equalization," *IEEE Transactions on Signal Processing*, vol. 54, pp. 2187–2197, 2006.

[75] A. Garde, L. Sörnmo, R. Jané, and B. F. Giraldo, "Correntropy-based spectral characterization of respiratory patterns in patients with chronic heart failure." *IEEE Transactions on Biomedical Engineering*, vol. 57, pp. 1964–1972, 2010.

[76] W. Liu, P. Pokharel, and J. Principe, "Correntropy: Properties and Applications in Non-Gaussian Signal Processing," *IEEE Transactions on Signal Processing*, vol. 55, pp. 5286–5298, 2007.

[77] J.-W. Xu and J. Principe, "A Pitch Detector Based on a Generalized Correlation Function," *IEEE Transactions on Audio, Speech, and Language Processing*, vol. 16, pp. 1420–1432, 2008.

[78] M. G. Genton, "Classes of kernels for machine learning: a statistics perspective," *Journal of Maching Learning Research*, vol. 2, pp. 299–312, 2002.

[79] L. Mainardi, S. Cerutti, and L. Sörnmo, *Understanding Atrial Fibrillation: The Signal Processing Contribution*, 1st ed. Morgan and Claypool Publishers, 2008.

[80] C. Shannon, "Classic paper: Communication in the presence of noise," *Proceedings of the IEEE*, vol. 86, pp. 447–57, 1998.

[81] A. G. García, "Orthogonal sampling formulas: A unified approach," *SIAM Review*, vol. 42, pp. 499–512, 2000.

[82] A. Jerri, "The Shannon sampling theorem-its various extensions and applications: A tutorial review," *Proceedings of the IEEE*, vol. 65, pp. 1565–96, 1977.

[83] M. Unser, "Sampling-50 years after Shannon," *Proceedings of the IEEE*, vol. 88, pp. 569–87, 2000.

[84] P. Vaidyanathan, "Generalizations of the sampling theorem: Seven decades after Nyquist," *IEEE Transactions on Circuits and Systems I*, vol. 48, pp. 1094–1109, 2001.

[85] E. Meijering, "A chronology of interpolation: From ancient astronomy to modern signal and image processing," *Proceedings of the IEEE*, vol. 90, pp. 319–42, 2002.

[86] T. Strohmer, "Numerical analysis of the non-uniform sampling problem," *Journal of Computational and Applied Mathematics*, vol. 122, pp. 297–316, 2000.

[87] H. Choi and D. C. Munson, "Direct-Fourier reconstruction in tomography and synthetic aperture radar," *International Journal of Imaging Systems and Technology*, vol. 9, pp. 1–13, 1998.

[88] J. Jackson, C. Meyer, D. Nishimura, and A. Macovski, "Selection of a convolution function for Fourier inversion using gridding," *IEEE Transactions on Medical Imaging*, vol. 10, pp. 473–478, 1991.

[89] J. L. Yen, "On nonuniform sampling of bandwidth-limited signals," *IRE Transactions on Circuit Theory*, vol. 3, pp. 251–57, 1956.

[90] E. J. Diethron and D. Munson Jr, "A linear time-varying system framework for noniterative discrete-time band-limited signal extrapolation," *IEEE Transactions on Signal Processing*, vol. 39, pp. 55–68, 1991.

[91] G. Kakazu and D. Munson Jr., "A frequency-domain characterization of interpolation from nonuniformly spaced data," in *IEEE International Symposium on Circuits and Systems*, Portland, Oregon, 1989, pp. 288–91.

[92] G. Calvagno and D. C. Munson Jr., "New results on Yen's approach to interpolation from nonuniformly spaced samples," in *Proceedings of the IEEE International Conference on Acoustics, Speech, and Signal Processing*, 1990, pp. 1535–38.

[93] H. Johansson and P. Löwenborg, "Reconstruction of nonuniformly sampled bandlimited signals by means of time-varying discrete-time fir filters," *EURASIP Journal on Advances in Signal Processing*, vol. 2006, pp. 1–18, 2006.

[94] S. Tertinek and C. Vogel, "Reconstruction of nonuniformly sampled bandlimited signals using a differentiator–multiplier cascade," *IEEE Transactions on Circuits and Systems I*, vol. 55, pp. 2273–2286, 2008.

[95] J. Selva, "Functionally weighted lagrange interpolation of band-limited signals from nonuniform samples," *IEEE Transactions on Signal Processing*, vol. 57, pp. 168–181, 2009.

[96] S. M. Kay, *Fundamentals of Statistical Signal Processing. Detection Theory.* New Jersey, USA: Prentice Hall, 1993, vol. 2.

[97] V. Vapnik, *The Nature of Statistical Learning Theory.* New York: Springer–Verlag, 1995.

[98] G. Camps-Valls, J. L. Rojo-Álvarez, and M. Martínez-Ramón, *Kernel Methods in Bioengineering, Signal and Image Processing.* Hershey, PA (USA): Idea Group Inc., 2006.

[99] J. L. Rojo-Álvarez, C. Figuera-Pozuelo, C. E. Martínez-Cruz, G. Camps-Valls, F. Alonso-Atienza, and M. Martínez-Ramón, "Nonuniform Interpolation of Noisy Signals Using Support Vector Machines," *IEEE Transactions on Signal Processing*, vol. 55, pp. 4116–4126, 2007.

[100] L. Zhang, Z. Weida, and L. Jiao, "Wavelet support vector machine," *IEEE Transactions on Systems, Man, and Cybernetics Part B*, vol. 34, pp. 34–39, 2004.

[101] S. Akselrod, D. Gordon, and F. Ubel, "Power spectrum analysis of heart rate fluctuation: a quantitative probe of beat-to-beat cardiovascular control," *Science*, vol. 213, pp. 220–2, 1981.

[102] N. Wiener, *Extrapolation, Interpolation, and Smoothing of Stationary Time Series*. Wiley, New York, 1949.

[103] A. J. Smola and B. Schölkopf, "A tutorial on support vector regression," *Statistics and Computing*, vol. 4, pp. 199–222, 2004.

[104] J. L. Rojo-Álvarez, G. Camps-Valls, M. Martínez-Ramón, A. Navia-Vázquez, and A. R. Figueiras-Vidal, "Support Vector Machines Framework for Linear Signal Processing," *Signal Processing*, vol. 85, pp. 2316–2326, 2005.

[105] J. L. Rojo-Álvarez, M. Martínez-Ramón, M. de Prado-Cumplido, A. Artés-Rodríguez, and A. R. Figueiras-Vidal, "Support Vector Method for Robust ARMA System Identification," *IEEE Transactions on Signal Processing*, vol. 52, pp. 155–164, 2004.

[106] J. L. Rojo-Álvarez, M. Martínez-Ramón, J. Muñoz-Marí, G. Camps-Valls, C. M. Cruz, and A. R. Figueiras-Vidal, "Sparse deconvolution using support vector machines," *EURASIP Journal on Advances in Signal Processing*, vol. 2008, 2008.

[107] B. Schölkopf and A. J. Smola, *Learning with Kernels*. Cambridge, MA: MIT Press, 2001.

[108] P. Laguna, G. Moody, and R. Mark, "Power Spectral Density of Unevenly Sampled Data by Least-Square Analysis: Performance and Application to Heart Rate Signals," *IEEE Transactions on Biomedical Engineering*, vol. 45, pp. 698–715, 1998.

[109] F. Tundo, F. Lombardi, M. C. Rocha, F. Botoni, G. Schmidt, V. C. Barros, B. Muzzi, M. Gomes, A. Pinto, and A. L. Ribeiro, "Heart rate turbulence and left ventricular ejection fraction in chagas disease," *Europace*, vol. 7, pp. 197–203, 2005.

[110] J. Koyama, J. Watanabe, A. Yamada, Y. Koseki, Y. Konno, S. Toda, T. Shinozaki, M. Miura, M. Fukuchi, M. Ninomiya, Y. Kagaya, and K. Shirato", "Evaluation of heart-rate turbulence as a new prognostic marker in patients with chronic heart failure," *Circulation Journal*, vol. 66, pp. 902–907, 2002.

[111] A. P. Hallstrom, P. K. Stein, R. Schneider, M. Hodges, G. Schmidt, and K. Ulm, "Characteristics of heart beat intervals and prediction of death," *International Journal of Cardiology*, vol. 100, pp. 37–45, 2005.

[112] A. Bauer, M. Malik, P. Barthel, R. Schneider, M. A. Watanabe, A. J. Camm, A. Schomig, and G. Schmidt, "Turbulence dynamics: An independent predictor of late mortality after acute myocardial infarction," *International Journal of Cardiology*, vol. 107, pp. 42–7, 2005.

[113] J. Schwab, G. Eichner, G. Veit, H. Schmitt, T. Lewalter, and B. Luderitz, "Influence of basic heart rate and sex on heart rate turbulence in healthy subjects," *PACE*, vol. 27, pp. 1625–1631, 2004.

[114] A. P. Hallstrom, P. K. Stein, R. Schneider, M. Hodges, G. Schmidt, and K. Ulm, "Structural relationships between measures based on heart beat intervals: Potential for improved risk assessment," *IEEE Transactions on Biomedical Engineering*, vol. 51, pp. 1414–1420, 2004.

[115] I. Cygankiewicz, J. Wranicz, H. Bolinska, J. Zaslonka, and W. Zareba, "Circadian changes in heart rate turbulence parameters," *Journal of Electrocardiology*, vol. 37, pp. 297–303, 2004.

[116] J. L. Rojo-Alvarez, A. Arenal-Maiz, and A. Artes-Rodriguez, "Discriminating between supraventricular and ventricular tachycardias from egm onset analysis," *IEEE Engineering in Medicine and Biology Magazine*, vol. 21, pp. 16–26, 2002.

[117] N. Guettler, D. Vukajlovic, A. Berkowitsch, B. Schulte, A. Erdogan, J. Carlsson, J. Neuzner, and H. Pitschner, "Effect of vagus blockade with atropine on heart rate turbulence," *PACE*, vol. 24 Part II, p. 625, 2001.

[118] I. Savelieva, D. Wichterle, M. Harries, M. Meara, J. Camm, and M. Malik, "Different effects of atrial and ventricular prematurity on heart rate turbulence: relation to left ventricular function," *PACE*, vol. 25 Part II, p. 608, 2002.

[119] M. Watanabe, J. Marine, M. Sheldon, and M. Josephson, "Effects of ventricular premature stimulus coupling interval on blood pressure and heart rate turbulence," *Circulation*, vol. 106, pp. 325–330, 2002.

[120] D. Roach and R. Sheldon, "Turbulence: a focal, inducible, source of heart period variability associated with induced, transient hypertension," *PACE Part II*, vol. 23, p. 709, 2000.

[121] B. Efron and R. Tibshirani, *An Introduction to the Bootstrap.* Chapman&Hall, 1998, vol. 57.

[122] J. González-Carrillo, A. García-Alberola, D. Saura, P. Carrillo, R. López, J. J. Sánchez-Muñoz, J. Martínez, and M. Valdés, "Impacto de la angioplastia primaria en la indicación de desfibrilador implantable en pacientes con infarto de miocardio," *Revista Española de Cardiología*, vol. 56, pp. 52–56, 2003.

[123] P. Jaskowski and R. Verleger, "Amplitudes and Latencies of Single trial ERP's Estimated by a Maximum-likelihood Method," *IEEE Transactions on Biomedical Engineering*, vol. 46, pp. 987–93, 1999.

[124] D. Lange, H. Siegelmann, H. Pratt, and G. Inbar, "Overcoming selective averaging: Unsupervised identification of event-related brain potentials," *IEEE Transactions on Biomedical Engineering*, vol. 47, pp. 822–826, 2000.

[125] I. Cygankiewicz, W. Zareba, R. Vazquez, M. Vallverdú, J. Cino, J. Cinca, J. Almendral, J. R. Gonzalez Juanatey, C. Macaya, M. Valdes, P. Caminal, and A. Bayes de Luna, "Relation of heart rate turbulence to severity of heart failure." *The American journal of cardiology*, vol. 98, pp. 1635–1640, 2006.

[126] A. Bauer, P. Barthel, R. Schneider, and M. Malik, "Impact of coupling interval on heart rate turbulence," *Eur Heart J*, vol. 22, p. 438, 2001.

[127] I. Savelieva, D. Wichterle, M. Harries, M. Meara, A. J. Camm, and M. Malik, "Heart rate turbulence after atrial and ventricular premature beats: relation to left ventricular function and coupling intervals," *PACE*, vol. 26, pp. 401–405, 2003.

[128] G. Schmidt, A. Bauer, R. Schneider, P. Barthel, M. Malik, A. J. Camm, and A. Schömig, "Heart rate turbulence: Impact of coupling interval and preceding sinus interval," *Eur Heart J*, vol. 21, p. 552, 2000.

[129] J. Francis, M. A. Watanabe, and G. Schmidt, "Heart rate turbulence: a new predictor for risk of sudden cardiac death," *Annals of Noninvasive Electrocardiology*, vol. 10, pp. 102–109, 2005.

[130] M. Watanabe, M. Alford, R. Schneider, A. Bauer, P. Barthel, P. Stein, and G. Schmidt, "Demonstration of circadian rhythm in heart rate turbulence using novel application of correlator functions," *Heart Rhythm*, vol. 4, pp. 292–300, 2007.

[131] A. Bauer, R. Schneider, P. Barthel, M. Malik, and G. Schmidt, "Heart rate turbulence dynamicity," *European Heart Journal*, vol. 22, p. 436, 2001.

[132] J. Schwab, G. Eichner, N. Shlevkov, J. Schrickel, A. Yang, O. Balta, T. Lewalter, and B. Lüderitz, "Impact of age and basic heart rate on heart rate turbulence in healthy persons," *PACE*, vol. 28, pp. S198–S201, 2005.

[133] J. O. Schwab, N. Shlevkov, K. Grunwald, J. W. Schrickel, A. Yang, L. Lickfett, T. Lewalter, and B. Lüderitz, "Influence of the point of origin on heart rate turbulence after stimulated ventricular and atrial premature beats." *Basic Research in Cardiology*, vol. 99, pp. 56–60, 2004.

[134] K.-T. Lee, W.-T. Lai, C.-S. Chu, H.-W. Yen, W.-C. Voon, and S.-H. Sheu, "Effect of electrophysiologic character of ventricular premature beat on heart rate turbulence." *Journal of Electrocardiology*, vol. 37, pp. 41–46, 2004.

[135] M. A. Watanabe, "Heart rate turbulence: a review." *Indian Pacing and Electrophysiology Journal*, vol. 3, pp. 10–22, 2003.

[136] A. Bauer, "Einfluß von Kopplungsinterval und Herzfrequenz auf die Heart Rate Turbulence," Ph.D. dissertation, Technischen Universität München, 2000.

[137] S. Steinberg, R. Robinson, and M. Rosen, "Molecular and cellular bases of β-adrenergic and α-adrenergic modulation of cardiac rhythm," in *Cardiac Electrophysiology: From Cell to Bedside*, D. Zipes and J. Jalife, Eds. WB Saunders, 2005.

[138] B. Efron and R. J. Tibshirani, *An Introduction to the Bootstrap*. Chapman & Hall, 1993.

[139] C. M. Bishop, *Pattern Recognition and Machine Learning (Information Science and Statistics)*. Springer, Oct. 2007.

[140] T. Hastie, R. Tibshirani, and J. Friedmann, *The Elements of Statistical Learning. Data Mining, Inference, and Prediction.* New York: Springer, 2001.

[141] G. James, T. Hastie, D. Witten, and R. Tibshirani, *An Introduction to Statistical Learning: With Applications in R.* Springer London, Limited, 2013.

[142] A. Voss, V. Baier, A. Schirdewan, and U. Leder, "Physiological hypotheses on heart rate turbulence," in *Dynamic Electrocardiography*, M. Malik and A. J. Camm, Eds. Blackwell Publishing, 2007, pp. 203–210.

[143] S. Theodoridis and K. Koutroumbas, *Pattern Recognition*, 4th ed. Academic Press, 2008.